**The Dissertation Committee for Youmin Wang**
**certifies that this is the approved version of the following dissertation:**

# Miniature Laser Scanning Micro-endoscopes: Multi-modality Imaging System and Biomedical Applications

**Committee:**

Xiaojing Zhang, Supervisor

Edward T. Yu, Co-Supervisor

Hsin-Chih Yeh

Wei Li

Andrew Dunn

James W. Tunnell

# Miniature Laser Scanning Micro-endoscopes: Multi-modality Imaging System and Biomedical Applications

**by**

**Youmin Wang, B.E., M.S.E**

**Dissertation**

Presented to the Faculty of the Graduate School of

The University of Texas at Austin

in Partial Fulfillment

of the Requirements

for the Degree of

**Doctor of Philosophy**

**The University of Texas at Austin**
**May 2013**

# Dedication

Dedicated to my family.

# Acknowledgments

It is ending, my five years of Ph.D., which has been proved to be an unforgettable experience.

I would never forget my life here in the University of Texas at Austin, which I would always be indebted to, for its formation of my plasma-physics and optics knowledge base, state-of-the-art cleanroom skillset, and clinical application experiences. Undoubtedly and more importantly, I would never forget my time shared with you here, my caring mentors, able colleagues, and true friends.

I would like to first express my deepest gratitude to my supervisor Dr. Xiaojing Zhang especially, for his invaluable support and guidance in my doctoral study. He opened the door for me to my research, career, and every possible opportunity. He set me a lifelong admirable example with his work ethic, determination, and commitment to excellence in all aspects of life. He is the right great mind I sincerely intend to follow in my all possible achievements, even after my graduation.

I also thank my committee members, my co-supervisor Dr. Edward Yu, Dr. James W. Tunnell, Dr. Wei Li, Dr. Andrew Dunn, and Dr. Hsin-Chih Yeh for serving on my dissertation committee and giving insightful advices on my dissertation research. Dr. H. Stan McGuff at the University of Texas at San Antonio Health Science Center provided objective and practical advice regarding imaging experiments. I enjoy the friendship from faculty and staff from Biomedical Engineering Department, Dr. Ning Jiang, Dr. Pengyu Ren, Chris Cooper, Bobby Knight, and Jim Pollard, from our collaborative startup company NanoLite systems Dr. Ting Shen, and from Microelectronics

Research Center, Ricardo Garcia, Johnny Johnson, Dr. Marylene Palard and many others.

I am thankful for the valuable contributions and warm-hearted caring from my collaborator and good friend Dr. Daghan Yigit Gokdel. The wine of our everlasting friendship inspired from the shared meaningful works and joyful talks would never run dry. The collaboration with Dr. Kazunori Hoshino, Sheldon Bish, Bin Yang, Dr. Lingyun Wang, Yu-Yen Huang, Gauri Bhave, and Youngkyu Lee will also be happily memorized for my life.

I also wouldn't forget my undergraduate mentees Milan Raj, Gloria Chao, Ryan Jang, Alex Hu, Christine Sparks and Nicholas Triesault for their encouragements and help during the process finishing my Ph.D. Without them I couldn't have learned the true meanings of leadership, mentorship, and project management.

Finally, I would like to thank my parents, Xiaoying Cheng and Huaibao Wang, for giving me the unconditional love and support over so many years. They are the reason and motif for which I fought through the hardships, scarce to be counted.

My five years' Ph.D. is ending, but my endeavor in research and academia will continue. Sir Winston Churchill said: "It is not even the beginning of the end. But it is, perhaps, the end of the beginning." So is it for my efforts on Micro-Electro-Mechanical System (MOEMS) and endoscope research.

Many thanks to all.

Youmin Wang

The University of Texas at Austin

May 2013

# Miniature Laser Scanning Micro-endoscopes: Multi-modality Imaging System and Biomedical Applications

Publication No. _____

Youmin Wang, Ph.D.
The University of Texas at Austin, 2013

Supervisors: Xiaojing Zhang
Edward T. Yu

Cancer is a world menace. After years of endeavor seeking the end of it, people started to realize that no matter how powerful the therapy could be, detection at early stage is always a cheaper, easier and more successful solution compared with curative methods for cancer developed onto its advanced stage. However, relatively few early-detection approaches have proven sufficiently effective and practical for mass use as a point-of-care tool. An early-cancer screening tool integrating the desired features of sensitive, informative, portable, and cost-effective is in need for the doctors.

The progress in optical imaging and Micro-electro-mechanical system (MEMS) technology offers a promise for an innovative cancer screening alternative that is non-invasive, radiation-free, portable and potentially cost-effective. This dissertation investigates handheld instrumentation as multi-modalities of miniature imaging probes with various designs of MEMS devices, to obtain real-time images of epithelial tissue optical and physiological properties, combining the quantitative advantages of spectral analysis

with the qualitative benefits of imaging to distinguish early cancer. This dissertation in sequence presents the handheld instruments in the fashions of Laser-scanning confocal microscopy (LSCM), optical diffuse reflectance imaging, nonlinear optical imaging modalities with their subsequent image-guided managements in oral cancer, skin cancer detection, circulating tumor cell (CTC) imaging, and imaging guided surgeries.

One of the main challenges facing miniaturization lies in the mechanism of beam deflection across the sample. This dissertation introduces two generations of MEMS devices desgined, fabricated and incorporated in the imaging probes. A two-axis vertical comb driven silicon micromirror was used in the development of a handheld LSCM for oral cancer detection. Though obtaining numerous advantages, this first generation silicon MEMS micromirror suffers from small aperture size and high voltage requirement for actuation, which result in low collection efficiency in fluorescence imaging and medial safety concerns, respectively. Therefore a stainless steel scanner compatible with electrical discharge machining (EDM) process was fabricated with simplified process, low-voltage magnetic actuation and large fluorescence collection efficiency, with its capability demonstrated in the incorporation and embodiment of a handheld hyperspectral nonlinear imaging probe.

Besides, software and controlling innovations for handheld imaging modalities are presented. A feedback controlling system for MEMS scanning status monitoring was developed for stabilized imaging rendering. For the sake of further improved imaging stability in handheld imaging and to enable on-site mosaic for large field viewing, a handheld mosaic system was developed and presented.

# Table of Contents

# List of Tables

# List of Figures

# Chapter 1

# Introduction

Cancer is a major public health problem and globally it will become the No. 1 killer disease in the future. Worldwide, more than 6 million people die from cancer and more than 10 million new cases are detected each year. 85% of cancers arise in the epithelium and include broad classes of cancers such as cervical, colon, lung, stomach, bladder and skin cancers [1]. 60% of the mortalities and 54% of the new cases are in developing nations, where patients have limited access to sensitive screening tests and advanced healthcare facilities.

Parallel to advances in various other directions of cancer research, the concept of early detection has been discussed by cancer-control researchers for many years. A great deal of research is invested in improving treatment for advanced disease, because most people who develop cancer have advanced disease at the time of diagnosis. However on the other hand, these life threating cancers could be promising to be curable if detected at an early stage. Until now, though, relatively few early-detection approaches have proven sufficiently effective and practical for mass use. An early-cancer screening tool integrating the desired features of sensitive, informative, portable, and cost-effective is in need to diagnose the condition characterizing each patient's disease, and tailor treatment strategies for the doctors.

Here we start a brief survey on the desired early cancer screening tool with its features and requirements rooted in the current management strategies employed for

an organ specific cancer, and materialized taking the advantage of start-of-the-art engineering techniques. Specifically, we propose to obtain real-time images of epithelial tissue optical and physiological properties, combining the quantitative advantages of spectral analysis with the qualitative benefits of imaging to distinguish early cancer using functional miniature imaging probes with various embodiments of Micro-Electro-Mechanical System (MEMS) devices.

## 1.1 Cancer facts

In the 4000-year long history accompanying us, cancer has gone from the black box to blueprint. Inaugurated on December 23, 1971, the National Cancer Act signed by by President Richard Nixon also witnessed and promoted the extensive theoretical and clinical advances achieved by medical practitioners. During the recent decades lots of efforts and progress have been made in cancer chemotherapy, radiation therapy and surgery.

Surgery has been the traditional treatment for cancer. The famous 18th century surgeon, John Hunter, first suggested that surgery might cure cancer if the tumor had not invaded the surrounding tissue. But early surgery was a risky procedure. The field of cancer surgery, or 'surgical oncology', developed in parallel with the advance in surgery anesthetics. Between 1860 and 1890 Theodore Billroth in Austria successfully operated to remove the stomach, voicebox and foodpipe. In the USA in 1889, William Halsted noticed that breast cancer recurred more often in women who had had their tumor removed but not the surrounding tissue. He developed a technique called the 'radical mastectomy', the surgical removal of the tumor, breast, overlying skin and muscle. At around the same time, the English surgeon Stephen Paget discovered that cancer cells

could spread through the blood and lymph systems, but could only grow in a few organs. He drew the brilliant analogy between cancer spread ('metastasis') and 'seeds that are carried in all directions, but they can only live and grow if they fall on congenial soil' [2].

Cancer surgery has benefited from the use of high-tech imaging techniques such as ultrasound, MRI and CT scanning. These procedures allow a surgeon to find out the exact size and shape of a patient's tumor.

Wilhelm Conrad Rontgen discovered X-ray In October 1895. Soon after that, in March 29, 1896 Emil Grubbe who was then a medical school student in Chicago assembled the first x-ray machine used it to treat a woman with breast cancer. Though unsuccessful, this treatment announced the foundation of radiology therapy, cancer treatment has entered the atomic era.

In 1898, Pierre and Marie Curie isolated a new radioactive element and named it "radium", which is a landmark in chemistry and physics. This great discovery also promoted the progress in radiotherapy. The day of Marie Curie's arrival in New York City in 1922, the headline in the New York Times read, "Mme. Curie Plans To End All Cancers—Says Radium Is Sure Cure, Even in Deep Rooted Cases, if Properly Treated." In November 1908, Radiologist Antoine Beclere in Paris did the first successful radiotherapy treatment of a 16-year old girl with brain tumor.

However, it tool biologists decades to figure out why radiation is effective on cancer treatment. The reason lays in its destruction of the DNA chains, especially those of rapid growing cells. Meanwhile, it did not took long for people to discover the side-effects of radiation. Ironically, the radium that was being touted as a cancer cure-all may have contributed to Curie's death in 1934. The doctor who cared for her described

the cause as "aplastic pernicious anemia ... The bone marrow could not react probably because it had been injured by a long accumulation of radiation."

On the other hand, mortality rates dropped in recent years not primarily due to the improved treatments for cancer at advanced stage, but largely due to the increased awareness, earlier detection of the condition through increased screening, and improved treatment options. Aside of the aforementioned treatment therapies, it is always preferable to prevent cancer. Some notable successes with cancer prevention has been made with discoveries of the connection between viruses and cancer, methods of chemoprevention, and the role of tobacco in cancer. Meanwhile, the importance of early detection by screening is highlighted by studying the dependence of survival rates on the stage at which the disease was diagnosed. Early detection is high on the future agenda of oncologists because of significant evidence that it will result in a higher cure rate [3, 4].

## 1.2 Rationale for approach

### 1.2.1 Image-guided cancer management

As the stepwise progression of human cancer well recognized, morphological and phenotypic changes that accompany cancer pathogenesis is important for building tools and determining criteria to diagnose the condition early (Figure 1.1). Pre-malignant lesions such as dysplasia and hyperplasia can be detected in diverse organs prior to the appearance of fully malignant invasive tumors. The pre-malignant lesions are caused either by genetic alterations which induce monoclonal expansion of the cells, or by environmental factors, such as viral infection. Subsequently, accumulation of genetic alterations occur in one of the pre-malignant cells, and the cells convert into malignant ones of clonal origin and produce a primary tumor. However, at the early stage

of primary tumor expansion, the cells are not invasive and metastatic. Then, new clones with invasiveness and metastatic ability appear as a result of further accumulation of genetic alterations in the cells. Thus, fully malignant cells are invasive and metastatic, then the carcinoma then invades the basal membrane of the duct or lobule. At this point, the tumor has the potential to spread through the rest of the organ and invade the lymphatic system, causing significant structural changes.

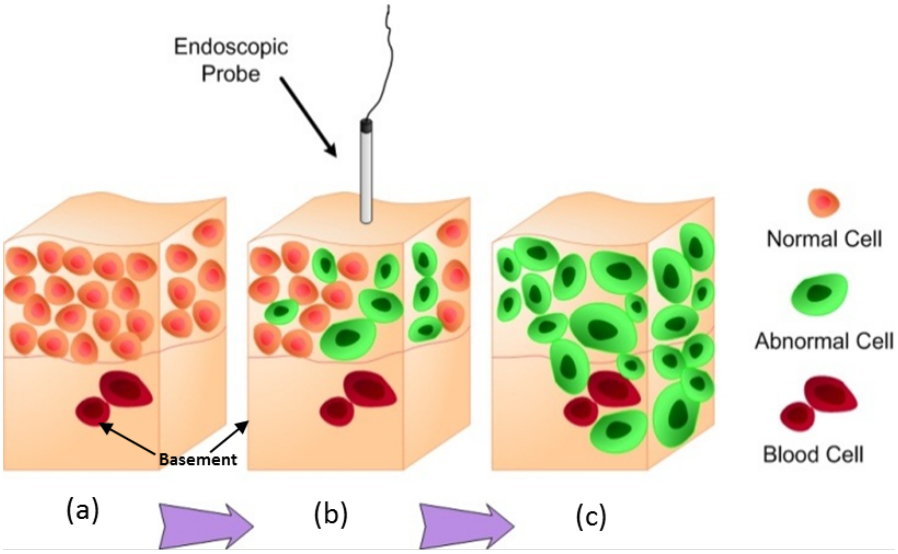


Figure 1.1: Structure of stratified squamous tissue under (a) normal conditions, (b) dysplastic conditions, and (c) metastic conditions.

Specifically, 85% of all cancers are known to originate in the epithelium [5].The epithelium is comprised of a stratified squamous structure (see Figure 1.1); it consists of a surface layer, a basement membrane, and the underlying stroma. Neoplastic cells originate at the bottom layers of epithelium along the basement membrane. These cells grow progressively upwards through epithelium and eventually cover the entire epithelial thickness. It is at this point that neoplastic cells break through the basement membrane, invading the stromal layer. By detecting neoplastic cells in their earliest stages

and evaluating their degree of malignance, it will be possible to effectively treat pre-cancer.

Early detection of these neoplastic cells promises minimally invasive treatment and greatly improves long-term survival rates. It is critical for timely intervention, represents one of the most promising approaches to reduce the burden of cancer [3]. The concept of early detection — finding tumours early, before they spread and become incurable — has been discussed and investigated for many years. When cancer is detected at its early stage, patients live longer, require less extensive treatment and could save the curative cost greatly comparing with developed as a more advanced disease. Currently, invasive needle biopsy and radiation-based screening technologies such as MRI and CT are gold standard in cancer diagnosis. However both approaches have many limitations in preventive screening. Although MRI and CT are proven technologies for cancer diagnosis, they are often used to confirm cancer diagnosis when the tumors have grown into a significant size, and have limited usage in early diagnosis for several reasons. First of all, physicians are concerned that frequent exposure to radiation can be a major cause of cancer, thus using radiation-based technologies for preventive diagnosis can indeed cause cancer, ironically [6]. Second, current MRI and CT exams are still expensive, and thus majority of the worldwide population cannot afford it as a frequent preventive diagnosis. Third, MRI and CT are typically bulky and housed in hospitals or major practices, thus cannot be widely adopted as a point-of-care solution especially in developing countries.

On the other hand, the development of endoscopy has experienced more than one century. Derived from the beginning prototype, modern medical endoscopes have been used in a variety of applications to examine the interior of a hollow organ or cavity of

the body. Accompanying the continuous efforts fighting with cancer, endoscopes have emerged as an effective tool in early cancer detection. The progress in optical imaging, Micro-electro-mechanical system (MEMS) technology and semiconductor manufacturing offers a promise for an innovative cancer screening alternative that is non-invasive, radiation-free, portable and potentially cost-effective. My goal in this dissertation research is to enable a new class of low cost, multi-functional clinical tool that can significantly improve early diagnosis of epithelial cancers such as skin, oral, cervix, lung and colon cancers (Figure 1.2). This proposed MEMS scanners based on various materials can be used to spot tumors at a very early stage and determine how far the cancer has progressed. It also can be used to monitor the tumor during treatment, and track the efficiency of therapy adopted, thus opening up a whole new opportunity to conquer cancers.

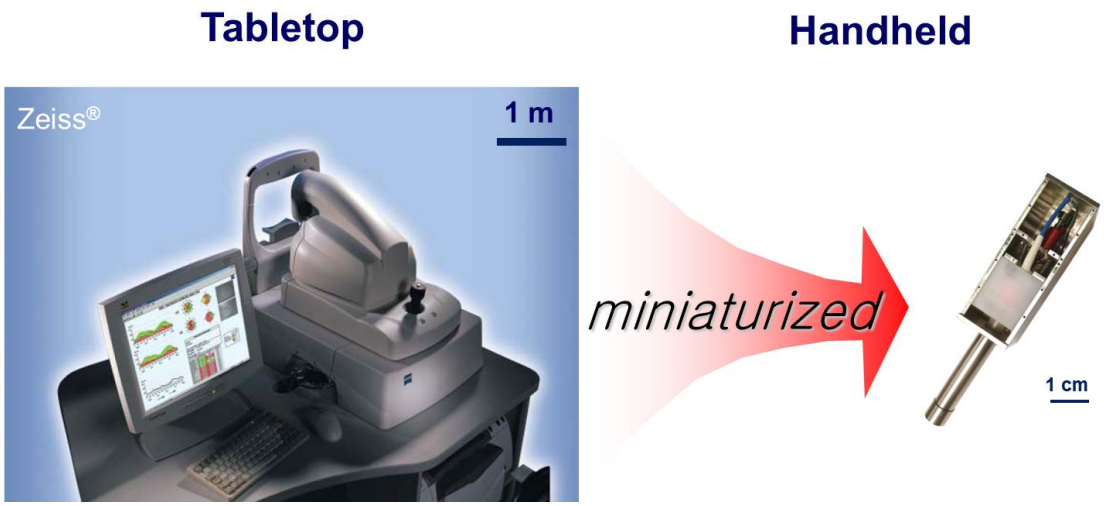


Figure 1.2: Miniaturization of microscope for handheld early cancer diagnosis

### 1.2.2 Abilities of the micro-endoscopy

We have developed multiple handheld laser-scanning microscopes targeted for cancer locating at different organs. Coupled with different cancer identifiers and imaging schemes, MEMS enabled portable imaging instruments with architectures including confocal reflectance imaging, hyperspectral imaging and two-photon imaging have been explored and tested. The mainstream of the research scope is well presented in Figure 1.3.

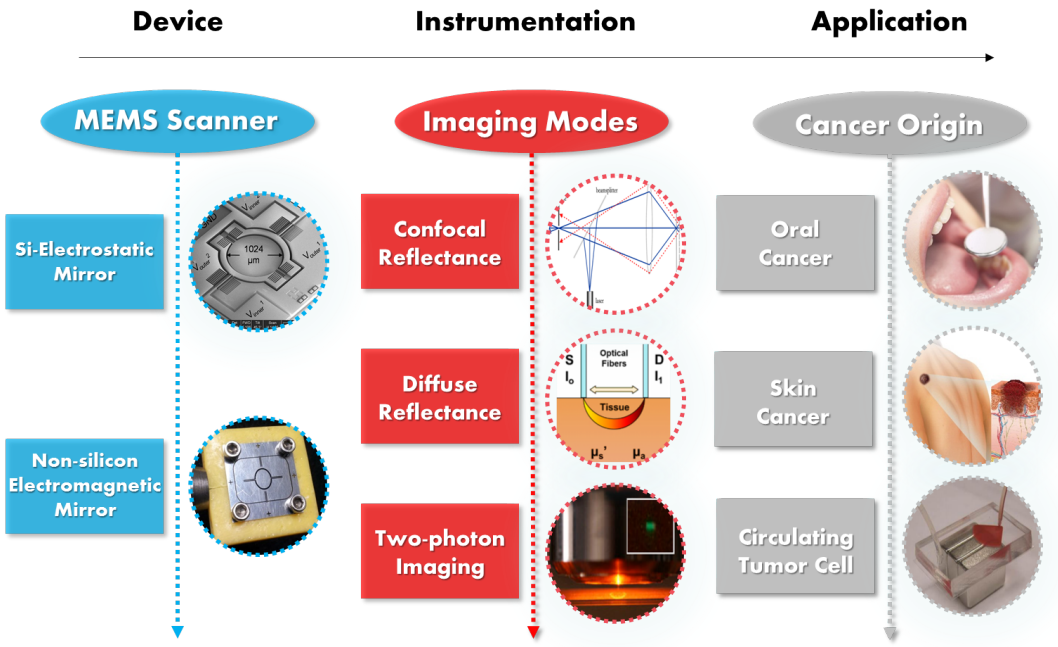


Figure 1.3: Thesis research path from device to clinic.

The handheld confocal reflectance microscope designed for oral cancer detection is capable of resolving sub-cellular morphological and physiological features of tissues via reflectance confocal imaging of optical sections up to 250 $\mu$m beneath the tissue surface. Neoplastic lesion tissues of Giant Cell Fibroma and Peripheral Ossify-

ing Fibroma, the fibroma inside the fixing paraffin box and ex-vivo gross tissues were imaged by the handheld imaging modality, and further compared with traditional confocal microscope imaging results. The instrument is designed in a single-fiber, portable format to help improve access to biopsy-free examination in low-infrastructure environments. The resulting early detection and high-resolution, sensitive mapping of structural and physiological function could dramatically improve patient prognosis, while reducing screening costs, treatment delay, and occurrences of unnecessary and potentially harmful medication.

The handheld hyperspectral fluorescence microscope combined with diffuse reflectance imaging was designed for the functional spectral skin cancer diagnosis based on the detection of Melanoma and nonmelanoma (basal and squamous cell carcinoma. Skin cancer is the most common type of cancer in the Caucasian population and the incidence of skin cancer has reached epidemic proportions. The handheld hyperspectral imaging probe was based on 488nm argon laser excitation source for confocal fluorescence imaging. It is able to acquire spectral information from 15 wavelengths simultaneously by using a multichannel photomultiplier tube (PMT). Hyperspectral resolution of 20nm from 490-730nm, with a fast imaging speed of 2 seconds per hyperspectral frames were obtained for images of a quantum dots infused PDMS phantom sample.

To take the advantages of nonlinear optical imaging in terms of low phototoxicity, high power efficiency and improved z-resolution, we further developed handheld two photon imaging instrument was operated based on the intrinsic/extrinsic nonlinear fluorescing induced by ultra-short pulse train of high energy density NIR laser. As the goal of the projects we demonstrated the feasibility of the handheld MEMS based scanning spectrometer to be potentially suitable for detecting auto-fluorescence spec-

trum of various kinds of epithelial cancer tissue.

## 1.3 Dissertation organization

This dissertation is arranged as follows. ”Chapter 2 Background” review the underlying mechanisms behind confocal, hyperspectral fluorescence microscopies and nonlinear microscopy with femtosecond laser pulses, as well as their clinical applications and current state of development.

Chapter 3 explores the unique design considerations and constraints that dictate the options for clinical development and discussed the design, construction and testing of an handheld laser laser-scanning confocal microscope for oral cancer detection. Chapter 4 describes the the functional fluorescence hyperspectral imaging probe integrated with optical diffuse reflectance imaging for skin cancer detection. Chapter 5 described two major novel improvements implemented on the device level for imaging enhancements that can be achieved by the modifications of the MEMS micromirror – non-silicon material MEMS scanner design, fabrication and testing, and compact “objective-less” micro-endoscopy. Chapter 6 introduced the handheld two-photon imaging probe incorporating the stainless steel scanner with advantages of lowered actuation voltage and enhance fluorescence collection efficiency.

Chapter 7 Conclusions and future work” concludes the thesis and future work recommendation is also presented.

# Chapter 2

# Background

Before diving into the detailed development of a MEMS based handheld laser-scanning endoscopes, it is helpful to review both the underlying physics, design and the scope of MEMS micromirror, laser scanning imaging, and light-tissue interaction mechanisms. This chapter will begin by discussing the historical developments and basic principles of MEMS micromirror. This section is followed by a review of the laser imaging geometrical optics principles and current microscope development status. Next, I provide a discussion of the current scope of clinical and pre-clinical applications of handheld endoscopes and how additional functional information including single/multi-photon excited fluorescence could help improve cancer diagnosis efficiency. Lastly, this chapter will cover confocal and nonlinear imaging endoscopes' applications that establish the motivation for creating a clinical laser-scanning diagnostic endoscope.

## 2.1 Principles and status of micro-endoscopy

Micro-endoscopy has been intensively studied due to its capability of in vivo real-time imaging of neoplastic lesions. Laser-scanning microscopy (LSM) allows high-resolution imaging, while at the same time its optical sectioning ability and in-depth imaging beneath a few hundred micrometers beneath the tissue surface enable precise cancer diagnosis on the tumor sites. Currently confocal laser endo-microscopy has been well developed for gastrointestinal tract, and is under study of the investigation of lesions

in human oropharynx [7].

Several approaches have been explored previously to achieve laser scanning micro-endoscopy in small form factor. Proximal scanning systems wherein a micro-optics fiber-based assembly is translated axially and/or rotated [24] within a protective sheath have been employed in imaging modalities that require only slow scan rates in sideways-imaging systems. Forward-imaging requires fiber-bundle imaging or a distal scan mechanism. A fiber-optic bundle consisting of thousands of closely spaced fibers packaged with an objective lens has been used for in vivo imaging [8] by selecting, at the proximal end, the fiber through which the illumination is directed, and scanning through all the fibers sequentially. Though compact, this method suffers heavily from pixilation imaging artifacts and lowered spatial resolution due to finite spacing between adjacent fiber cores. Distal scanning has been achieved by fiber/objective translation [9, 10]. These techniques suffer from slow scan rates and limited field of view either by demagnification of the objective lens or optical aberrations. The most promising technique for fast-scanning units is micromirror-based angular beam deflection. Micromirrors driven by piezoelectric [11], thermal [12], magnetic [13, 14, 15] and electrostatic [16, 17, 18] actuation schemes have been explored previously.

## 2.2 MEMS micromirror

The acronym for Microelectromechanical systems (MEMS) was initialized in 1989 at Salt Lake City where a workshop called Micro - Tele -Operated Robotics Workshop was held. Currently, MEMS technology has started major novel innovations in various scientific fields and created highly promising market potential. Optics and photonics are research fields greatly impacted by MEMS techniques and the ability to steer

or direct light is one of the key requirements in optical MEMS. In the past two decades since Petersen published his silicon scanner [19], the field of optical MEMS has experienced explosive growth [20, 21]. In the past decades, displays and laser scanning imaging were the main driving force for the development of micromirror arrays (Figure 2.1). The demand for routing Internet traffic through fiber optic networks pushes the development of both digital and scanning micromirror systems for large port-count all-optical switches with the ability to directly manipulate an optical signal. In the biomedical imaging arena, micro-optical scanners promise low-cost endoscopic three-dimensional imaging systems for in vivo diagnostics.

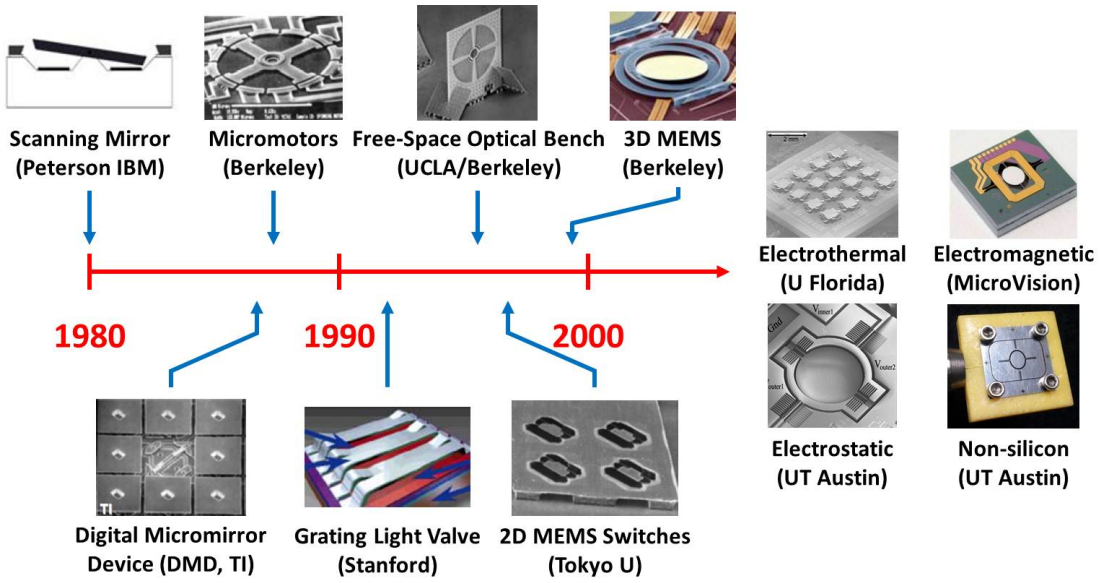


Figure 2.1: 30 years of Optical MEMS development.

For biomedical imaging, fast-scanning mechanisms for deflecting the excitation illumination source over the sample in raster or Lissajous scanning fashion form the core technology in realizing the real-time in-vivo imaging. Optical MEMS technologies are ideally suited to creating the fast-moving micromirror that can be incorporated into

compact imaging systems. Comparing with conventional laser scanning components, MEMS micromirror has its specific advantages. First, great mass could be reduced while dimensions of the device of the micro-device is scaled down. These in total would result in high vibrational resonant mode frequencies of the micro-device that could be utilized for fast scanning. Second, MEMS micromirror takes the advantages of tremendous knowledge and nanofabrication facilities developed for the growth of the semiconductor industry. Batch-fabrication of the devices could guarantees the fabrication precision and economy due to the unprecedented expertise and repeatability of the fabrication methods [22]. Third, the small overall size of these devices allows for integration into compact micro-endoscopes, which is important for translation of innovative optical technologies from research laboratories to clinical application, a primary goal of this dissertation.

The handheld confocal reflectance endoscopy research of this thesis research combines the advantages of electrostatic comb-drive driven micromirrors with CMOS-compatible silicon processing technology. The MEMS micromirror that has been utilized (Figure 2.2) addresses the deficiencies of traditional electrostatic combdriven micromirrors such as nonlinear transformation between input voltage and mechanical scanning angle, and scanning instabilites due to pull-in phenomena [22, 23, 24]. Complicated comb self-alignment procedures were adopted in micromirror fabrication to mitigate this problem [16, 25, 26, 27, 28, 29]. These drawbacks were addressed by introducing a simple 3-mask comb self-aligned micromirror fabrication process compatible with traditional CMOS processing in the semiconductor industry. The major advantage is the monolithic integration of the IC and MEMS components towards multi-functional and intelligent micro-systems.

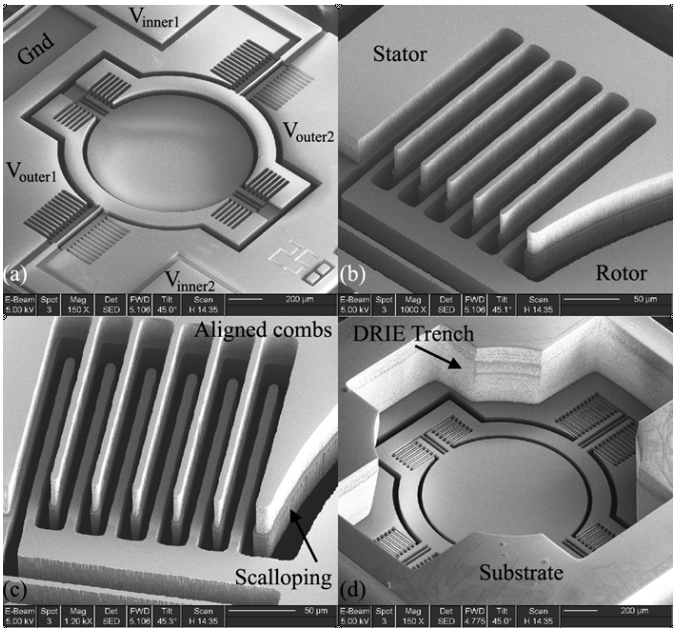


Figure 2.2: Scanning electron micrograph (SEM) images of the fabricated devices. (a) Top view of micromirror showing electrical bond pads, comb drives on both axes, and micromirror surface. (b) Close-in view of layers forming the combdrive actuator on the inner axis. (c) Close-in view of the quality of alignment between the stator and rotor comb fingers. (d) Backside view of the substrate DRIE through-etch, bottom face of the micromirror.

## 2.3 Imaging modalities for micro-endoscopy

### 2.3.1 Confocal microscope

Confocal optics provides an alternative solution to the problem of image degradation by out-of-focus light, improving resolution by physical rather than electronic or computational means. The principle of confocal microscopy was described by Minsky more than 40 years ago [30]. Confocal microscopy offers several advantages over conventional optical microscopy, including controllable depth of field, the elimination of image degrading out-of-focus information, and the ability to collect serial optical sections from thick specimens. The key to the confocal approach is the use of spatial filtering to eliminate out-of-focus light or flare in specimens that are thicker than the plane of

focus. There has been a tremendous explosion in the popularity of confocal microscopy in recent years, due in part to the relative ease with which extremely high-quality images can be obtained from specimens prepared for conventional optical microscopy, and in its great number of applications in many areas of current research interest.

The crucial element of confocal optics is the projection of an image of a focally illuminated point in the specimen onto a small aperture in a conjugate focal plane. In the embodiment shown in Figure 2.3, photons generated from the 632nm laser diode was delivered onto the sample through a single mode polarization-maintaining fiber, and the imaging lens system afterwards. The ballistic photons reflected back as optical signal would be collected after focused back through the single mode fiber, whose small diameter core serves as the pinhole for the confocal imaging system.

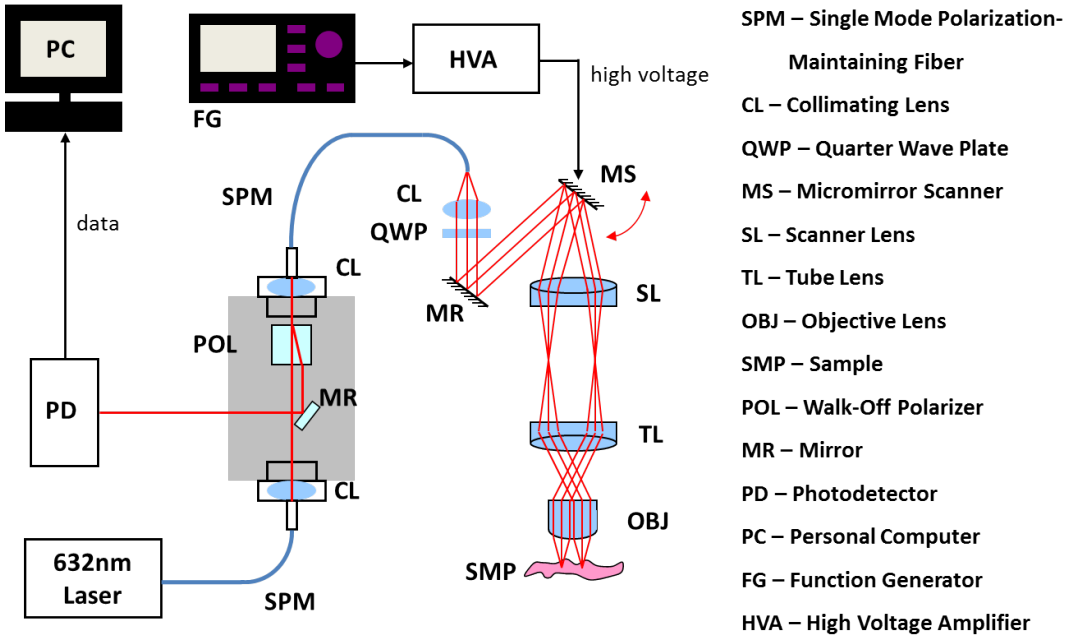


Figure 2.3: Schematic of a fiber coupled laser scanning confocal microscope.

Light from the illuminated point can pass through the aperture and be detected;

light from out-of-focus structures will be spread at, and blocked by, the aperture and will therefore be largely eliminated. By scanning the specimen across the point (or the point across the specimen), a 2D or 3D confocal image can be generated [31].

### 2.3.2 Optical diffuse reflectance imaging

There are many spectroscopic optical modalities that are used to investigate epithelial cancers such as skin cancer. One of the important topics discussed in this dissertation pertains to diffuse reflectance spectroscopy. The formal definition of diffuse reflectance is:

$$\frac{I_1(\lambda)}{I_0(\lambda)} = R(\mu_a(\lambda), \mu_s^{'}(\lambda)) \tag{2.1}$$

,where I1 and Io are the spectral intensities of light that enter and emerge from the tissue respectively. $\mu_a(\lambda)$ and $\mu_s^{'}(\lambda)$ correspond to the absorption and reduced scattering coefficients which are factors in the spectral form of diffuse reflectance 'R'. The coefficients $\mu_a$ and $\mu_s^{'}$ have opposing effects on R, where $\mu_s^{'}$ increases R and $\mu_a$ decreases R.

The functional form of $\mu_a$ is:

$$\mu_s^{'}(\lambda) = \mu_s^{'}(\lambda_0)\left(\frac{\lambda}{\lambda_0}\right)^{-\mathrm{B}} \tag{2.2}$$

where $\lambda_0$ is designated here as 630nm and B refers to the exponential dependence of reduced scattering on wavelength. The functional form of $\mu_a$ is,

$$\mu_a = \ln(10)\sum_{i=1}^{N} \varepsilon_i(\lambda) C_i \tag{2.3}$$

where $\varepsilon_i(\lambda)$ is the molar absorption coefficient of a chromophore with units that depend on the units of chromophore concentration Ci under consideration. The units of $\mu_a$ and $\mu_s^{'}$) are 1/x where x is a unit of distance.

Broadband optical spectroscopy can be used to reveal quantitative functional and morphological characteristics of skin. Using light of multiple wavelengths, various optical and physiological properties of clinical relevance can be derived such as scattering, hemoglobin concentration, oxygen saturation, and mean blood vessel diameter. As it relates to skin cancer, scattering properties have been shown to correlate with the presence of tumors of the skin, breast, and cervix [32, 33]. These correlations have been shown to be attributed to the increased size of the cancer cell nuclei, and number of mitochondria, which are the main sources of tissue scattering [34]. Scatterer size plays a role in the spectral response of tissue spectroscopy.

### 2.3.3 Nonlinear optical imaging

Though nonlinear optical imaging can broadly apply to a wide range of techniques including third harmonic generation and coherent anti-Stokes Raman scattering (CARS), here we limit discussion to Second Harmonic Generation (SHG) and Two Photon Excited Fluorescence (TPEF) microscopy, which provide stronger signals and can be easily realized with a single laser source. Traditionally, this laser source is a femtosecond laser oscillator, which can provide the ultrashort pulse durations (and therefore peak intensities) required for efficient nonlinear interactions while operating at fast enough repetition rates to enable practical imaging speeds.

Two-photon excited fluorescence microscopy is a form of laser scanning fluorescence microscopy capable of imaging to depths in excess of 1 mm in the absence of

strong scattering [35, 36]. In laser scanning fluorescence microscopy, a focused laser spot is scanned in a sample to excite fluorescence and the detected emission is reconstructed to create an image of the sample. Because two-photon absorption uses two photons of lower energy to overcome the bandgap in a fluorophore, wavelengths in the NIR can be used to excite many commonly used fluorophores. Just as in femtosecond laser microsurgery, the use of NIR wavelengths provides TPEF microscopy with depth penetration superior to that of single-photon fluorescence techniques.

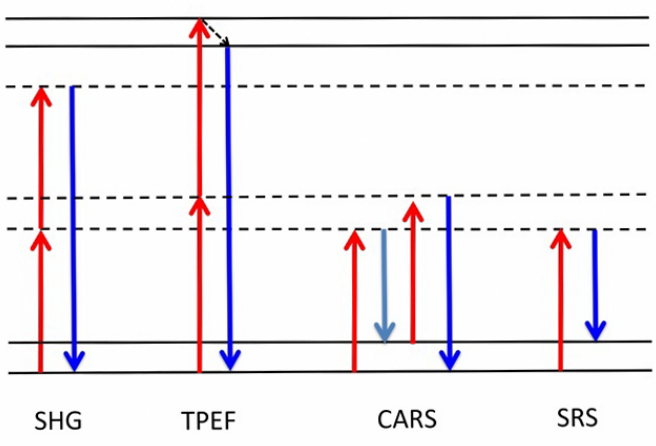


Figure 2.4: Jablonski diagram illustrating several nonlinear processes. SHG: Two photons are converted to a single photon with twice the energy, corresponding to half the wavelength. TPEF: Two photons are absorbed simultaneously to excite a molecular energy state which can emits fluorescene as if excited by a single molecule. CARS: Three beams interact with a vibrational mode to emit photons at slightly longer wavelengths. SRS: Two beams interact with a vibrational level to transfer energy from one beam to the other. [37]

Furthermore, because two-photon absorption depends quadratically on the incident light intensity, the excitation is three-dimensionally confined to the focal volume where the intensity is highest, as illustrated in Figure 2.5. In TPEF microscopy, this confinement provides inherent optical sectioning for highresolution three-dimensional (3D) imaging without the use of a pinhole. Because all emission light can be assumed

to originate from the focal volume, all scattered light can be collected while out-of-focus photobleaching and photochemical damage are greatly reduced.

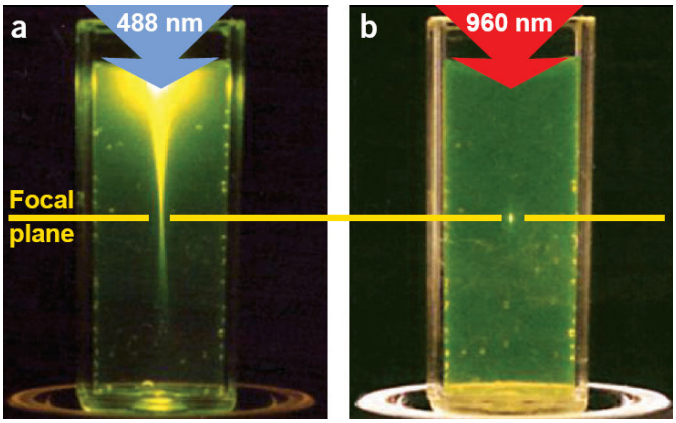


Figure 2.5: Comparison of excitation confinement in two-photon versus single-photon fluorescence. Single-photon excitation, a, exhibits significant out-of-focus excitation which leads to blurring and increased photodamage. Out-of-focus excitation is dramatically reduced in two photon excitation, b, where the nonlinear dependence on intensity for results in a three-dimensionally confined excitation volume. [38]

In addition, TPEF microscopy systems can also be used to image second harmonic generation (SHG) [38, 39]. SHG is a degenerate case of sum frequency generation, in which two electromagnetic waves interact with a material possessing a second-order nonlinear susceptibility ($\chi^{(2)}$) to create a third wave with a frequency equal to the sum of the frequencies of the incoming waves. Images of SHG can provide information about morphology in the extracellular matrix, where there are fewer endogenous fluorophores, which makes SHG imaging a good complement to TPEF microscopy. In practice, SHG microscopy is often performed concurrently with TPEF microscopy and many systems do not distinguish between the two signals.

Both TPEF and SHG microscopy can provide valuable diagnostic information when used to image biological tissue, and commercial clinical two-photon microscopes

have recently become available from JenLab GmbH (Jena, Germany). In addition to morphological information, excitation of endogenous fluorophores (autofluorescence) can be used to visualize other diagnostic indicators, such as the metabolic rate [40]. Specifically, recent studies have found that TPEF and SHG microscopy can be a powerful tool for early cancer diagnostics and staging by imaging cellular autofluorescence and observing changes in morphology and signal intensity [40, 41, 42]. Furthermore, the use of molecularly-specific targeted contrast agents can be used to identify a host of known disease indicators for imaging with TPEF microscopy [43]. The use of contrast agents has also be used to provide additional functional information, such as neural activity in the brain [44], as well as anatomical information, such as vascular pathways [45, 46], which enable a wide range of diagnostic applications.

## 2.4 Hyperspectral imaging: microscopy meets spectroscopy

All the aforementioned imaging modalities could be combined with hyperspectral imaging (HSI). Spectral imaging [47] combines the advantages of two well-known scientific methodologies naming the imaging and spectroscopy techniques. A spectral imager basically outputs a stack of images of the imaging target acquired in continuous bands over a certain spectral range. A simple method for measuring a spectral image is to use a set of color-filters (Figure 2.6B), each of which transmits a narrow band wavelength.A more convenient way is to use variable-filters, which are more compact and robust. Three common variable filters include the circular-variable filter (CVF) as shown in Figure 2.6A, liquid-crystal tunable filter (LCTF) shown in Figure 2.6C, and acousto-optical tunable filter (AOTF), as shown in Figure 2.6D. The CVF transmits a narrow-band light depending on the beam position on its surface (usually around a cir-

cular filter). The AOTF and LCTF are electro-optical components with no moving parts. The most common LCTF system (Lyot design) transmits a narrow-band wavelength by applying a varying voltage on a polarizable liquid crystal mounted between two linear polarizers (Figure 2.6C). Usually a few stages are needed to achieve high resolution which reduces the total transmission within the filter's passband. An AOTF uses a crystal such as Tellurium dioxide ($TeO_2$) on which acoustic waves are applied (Figure 2.6D). At each frequency of the acoustic waves, the crystal deforms to a grating with a specific period and therefore transmits a different wavelength in a given direction. These types of filters capture a full spectral image by measuring one image at a time but each time at a different wavelength.

The ability of hyperspectral imager to measure reflectance, absorption band depth and spectral edge shifts over time coupled with spatial information creates the possibility to analyze material changes. For example in remote sensing applications, the shift in the chlorophyll band edges of observed vegetation indicates stress [48]. Other potential applications of hyperspectral imaging include mineral identification in geology, terrain classification and camouflaged target detection in defense systems, on-line inspection of food products, coastal and inland water studies, environmental hazards monitoring and tracking, cancer detection in biomedical and life sciences.

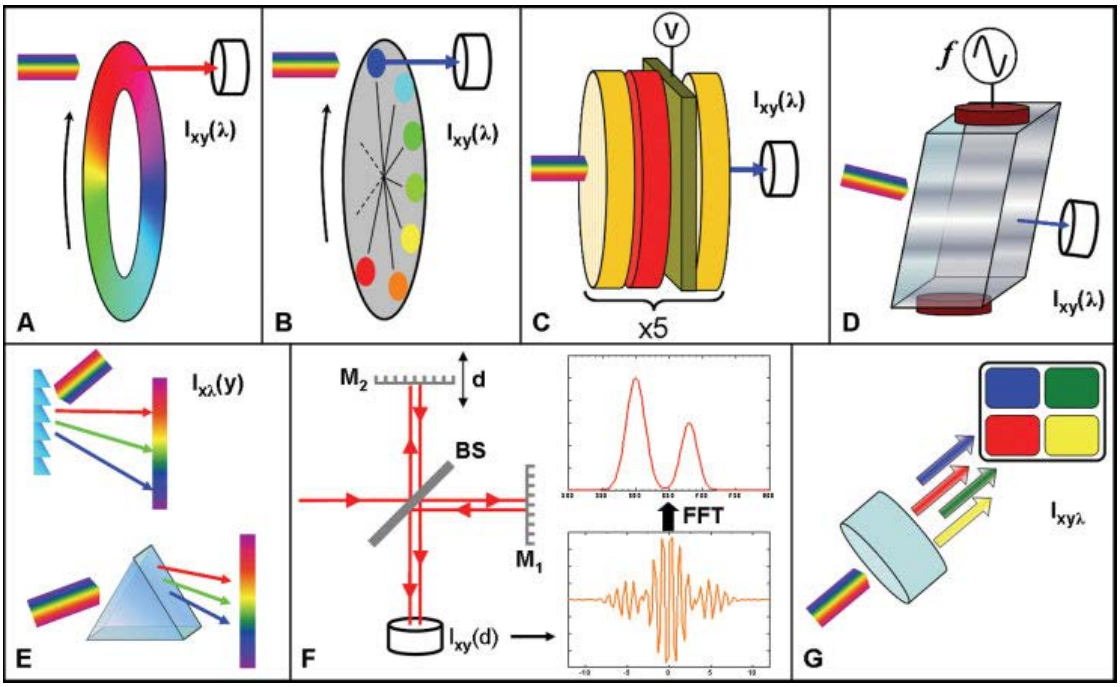


Figure 2.6: Various methods of spectral imaging systems. They can be divided into four main methods: wavelength-scan (A–D), spatial scan (E), time scan (F) and "compromise" methods (G). In wavelength-scan methods, the whole image is measured one wavelength at a time. This can be realized using either a circular variable filter (A), a set of filters (B), a liquid crystal variable filter (C) or an acousto-optic variable filter (D). Spatial-scan methods use a dispersion element, either a grating or prism (E) and the image has to be scanned along at least one axis. There are also confocal microscopes that use a dispersive element and scan the image point by point. In time-scanning method (F), the whole image is measured after passing through an interferometer (or other optical elements). In order to calculate the spectrum at each pixel a mathematical transformation has to be carried out, for example, a Fourier transform. In "compromise" methods (G) only a few spectral ranges are measured and the FOV is limited, but the measurement is fast. [47]

# Chapter 3

# Handheld Laser-Scanning Confocal Oral Cancer Endoscope

This chapter reviews the current status of handheld confocal microscope development and presents a design flow for a complete MEMS enabled handheld endoscope designed for oral cancer detection.

For the end of portable oral cancer detection, we developed a electrostatic MEMS combdrive micromirror enabled hand-held confocal imaging micro-endoscope, where comparatively large field-of-view (FOV) was generated through the programmable Lissajous scanning pattern of the MEMS micromirror. Bench-top MEMS confocal imaging setup was constructed and compared with the miniaturized confocal imaging probe in clinical imaging. For the handheld confocal imaging system, optical design simulations using Code V shows the sub-cellular resolution on both lateral and axial directions, which was experimentally proved and verified. Fast Lissajous imaging speed up to 2 fps was realized with improved LabVIEW and Java based real-time imaging software. Properties such as 3D imaging through auto-focusing and mosaic imaging for extended lateral view (6 mm $\times$ 8 mm) were examined for carcinoma real-time pathology. Neoplastic lesion tissues of Giant Cell Fibroma and Peripheral Ossifying Fibroma, the fibroma inside the paraffin box and ex-vivo gross tissues were imaged by the bench-top and handheld imaging modalities, and further compared with commercial microscope imaging results. We successfully showed the efficacy of the MEMS scanner based hand-

held confocal imaging probe as a potential clinical tool for oral cancer diagnosis and treatment.

We have demonstrated the CMOS compatible 2-axis MEMS micromirror [49] with applications in a variety of imaging modalities, including single fiber confocal microscope capable of sub-micrometer resolution for interventional imaging [49]. Other MEMS involved imaging applications involve forward-looking OCT [50] for cardiovascular applications and hyperspectral imaging system for epidermal carcinoma screening [51]. In this chapter we demonstrate the functionality and efficacy of the developed handheld confocal imaging probe by the imaging of clinical oral cancer samples including giant cell fibroma, epithelial ossifying fibroma, the fibroma treated and mounted inside glass slide, paraffin box and in-vivo gross tissue in UT Health Science Center (UTHSC), with the comparison to conventional laboratory confocal microscope.

## 3.1 Oral cancer overviews

Oral cancer has a lower survival rate comparing with other malignancies, in spite of the oral cavities' easier accessibility for diagnostic instruments (see Figure 3.1) [52, 53]. Its five-year survival various from 30% to 80%, as reported in different geographic regions [54, 55, 56, 57]. Traditional clinical diagnosis of oral cancer involves multiple steps such as tissue freezing and sectioning, paraffin embedding and histological staining and laboratory microscopy [58, 59]. To achieve higher survival rate, early and on-site diagnostic methods are much needed in oral health programs [53]. Early detection and real-time in vivo examination are highly preferred to improve treatment and reduce the processing cost and interpretation inaccuracy [60]. Confocal endomicroscopy has been intensively studied due to its capability of in vivo real-time imag-

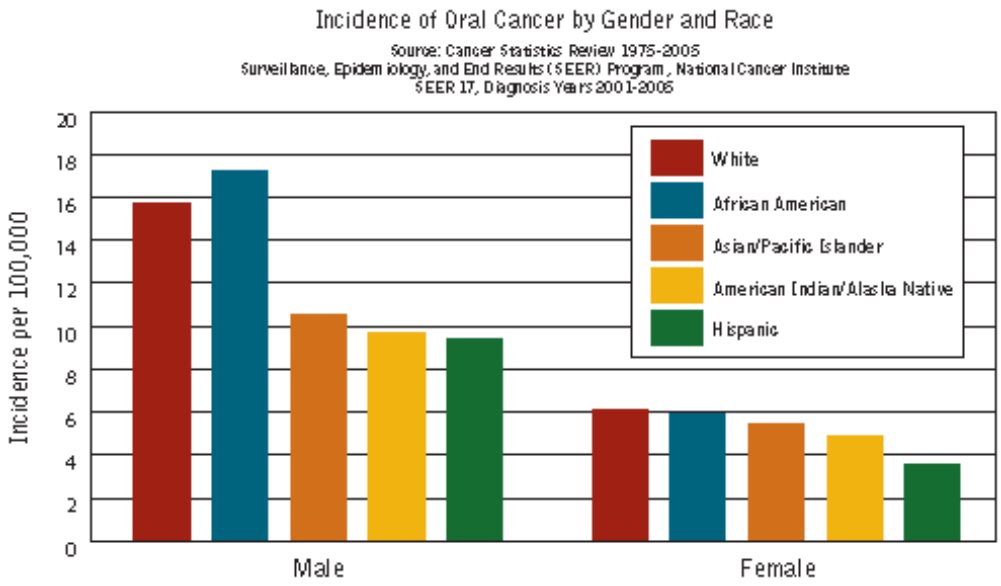


Figure 3.1: Incidence of oral cancer by gender and race. Source: Cancer Statistics Review 1975-2005, Surveilance, Epidemiology, and End Results (SEER) Program, National Cancer Institute. SEER 17, Diagnosis Year 2001-2006.

ing of neoplastic lesions. Laser-scanning confocal microscopy (LSCM) allows high-resolution imaging, while at the same time its optical sectioning ability and in-depth imaging beneath a few hundred micrometers beneath the tissue surface enable precise cancer diagnosis on the tumor sites. Currently confocal laser endo-microscopy has been well developed for gastrointestinal tract, and is under study of the investigation of lesions in human oropharynx [7]. Toward a handheld oral cancer detection device, a novel miniature confocal imaging probe capable of doing fast imaging, wide field of view (FOV) mosaic imaging and 3D imaging for oral cancer detection is demonstrated here, based on a 2-axis self-aligned vertical comb-driven micromirror [61] developed previously in our laboratory.

## 3.2 Endoscope design and system architecture

### 3.2.1 Electrostatic combdrive MEMS scanning mirror

Micro-electromechanical system (MEMS) technology provides the opportunity to offer highly compact single-fiber imaging probes with distal scanning mechanisms to non-invasively characterize epithelial cancers real-time in situ with a sub-micron resolution [62, 49, 27, 63, 64], while at the same time helps brings down the total expense of the medical instrument due to the ease of mass production in mature semiconductor and microelectronics industry.

The MEMS micromirror (Figure 3.2) was the core component enabling the imaging system. The micromirror has a diameter of 1024 $\mu$m, sitting on the microchip which is 2.8mm $\times$ 2.8mm. When applied high voltage on the two orthogonal of comb-drive structure, the staggered vertical comb-drive structure of the chip actuates the micromirror within the gimbal structure to rotate along the two perpendicular axes. The primary mechanical resonant frequencies of the fabricated MEMS micromirror were 2.57 kHz and 1.2 kHz for the inner and outer rotation axis respectively. The applying of sinusoidal high voltage AC actuating signal onto the two axes, the movement of the MEMS micromirror will form a Lissajous curve.

The fabricated MEMS scanning mirror was mounted onto a printed circuit board (PCB) to ease wire bonding, power delivery and packaging, as shown in Figure 3.2 (d). The MEMS chip has the wire-bondings onto it from 4 copper pads. Power wires were soldered onto the board to deliver high voltage MEMS actuation.

To maximize the field-of-view (FOV) of the imaging system, the MEMS scanner was running under the Lissajous scanning pattern. A pair of 75 volts peak-to-peak sinusoidal AC voltage with an offset of 50 volts was used to actuate the MEMS micromirror,

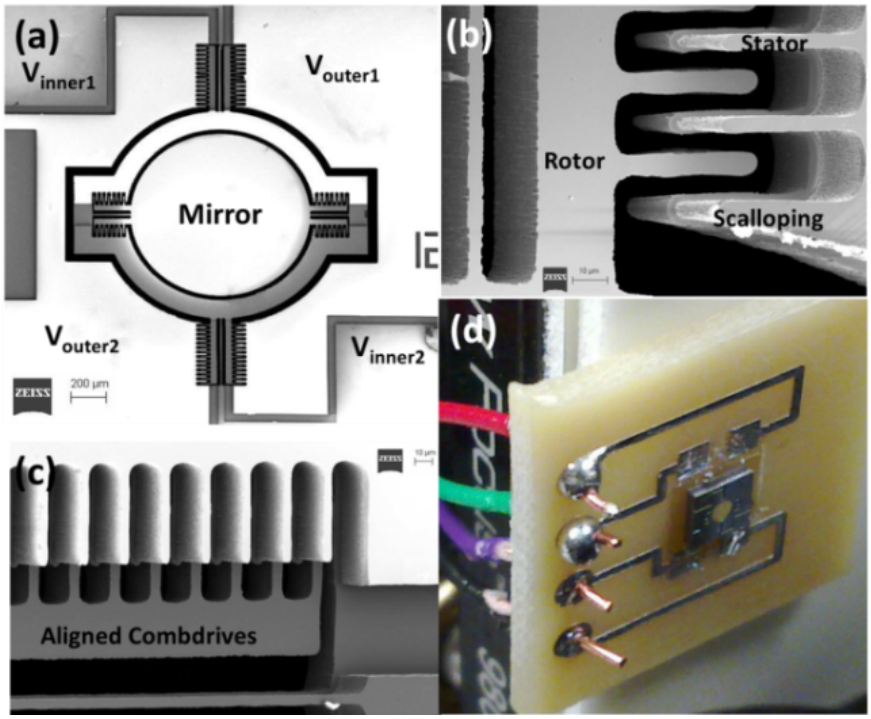


Figure 3.2: Scanning element in the handheld confocal imaging system. (a) Top view of the micromirror. (b) High quality alignment between the stator and rotor comb fingers on the inner axis, as defined by photolithography and deep reactive ion etching of silicon. (c) View of the comb-drive actuator on the outer axis. (d) Photograph of the MEMS micromirror mounted on a printed circuit board.

actuating the MEMS mirror to reach the maximum optical deflection angles at 28° and 25° respectively for the inner and outer axes.

### 3.2.2 Confocal imaging instrumentation

The schematic of the complete system is shown in Figure 3.3. The 635nm diode (Blue Sky Research, Inc., FMXL-635-017-PA-0B) generates laser beam which was then collimated, and delivered by a single mode polarizing maintaining fiber into the inner piece of the handheld probe, before reflected by the MEMS micromirror. The micromirror scanner pivots the laser beam at a stationary point that is conjugate with the rear

aperture of the first achromatic doublet lens (Thorlabs, Inc., AC064-013-A) and deflects the beam across its entrance aperture in a Lissajous pattern. After the first achromatic doublet lens the angular scanning beam from the micromirror scanner is converted to the linear fashion, and further focused by the second achromatic doublet lens (Edmund Optics, Inc., NT45-264). The position of the back focal plane of the second doublet lens is adjusted to meet the front focal plane of the first doublet lens , therefore the first two doublet lenses form an afocal Keplerian beam expander system, expanding the laser beam diameter from 1mm to 3mm, filling most of the clear back aperture of the objective. The laser beam exiting the second doublet lens is further focused onto the sample by an objective lens (Thorlabs ®, 352330-B NA=0.68). The reflected light indicating sample's refractive-index change was collected by the micromirror simultaneously, focused into the SMF again, and then transmits through a walk-off polarizer, before acquired by a photomultiplier tube (PMT, Hamamatsu Inc., H9858-20). The core of the SMF optical fiber was used as the "pinhol" for confocal imaging system here. A zero-order quarter wave-plate (Red Optronics, Inc., 0.1" $\times$ 0.1" MicroWaveplate) was used between the Kaplan lens system and the objective lens, for polarization-based noise reduction.

While the function generator (Tektronix, Beaverton Oregon) outputs the high-voltage AC sinusoidal scan signal at the resonant frequencies of the MEMS micromirror scanner to dictates the micromirror to scan in a Lissajous path, it also outputs the synchronizing signal acquired by the NI PCI-611 data acquisition card (DAQ) (National Instruments, Austin Texas) for the software to reconstruct the sampled signal intensity data from PMT into real-time images. A pair of lateral dual directional motorized stages was placed beneath the handheld probe in the case of mosaic imaging.

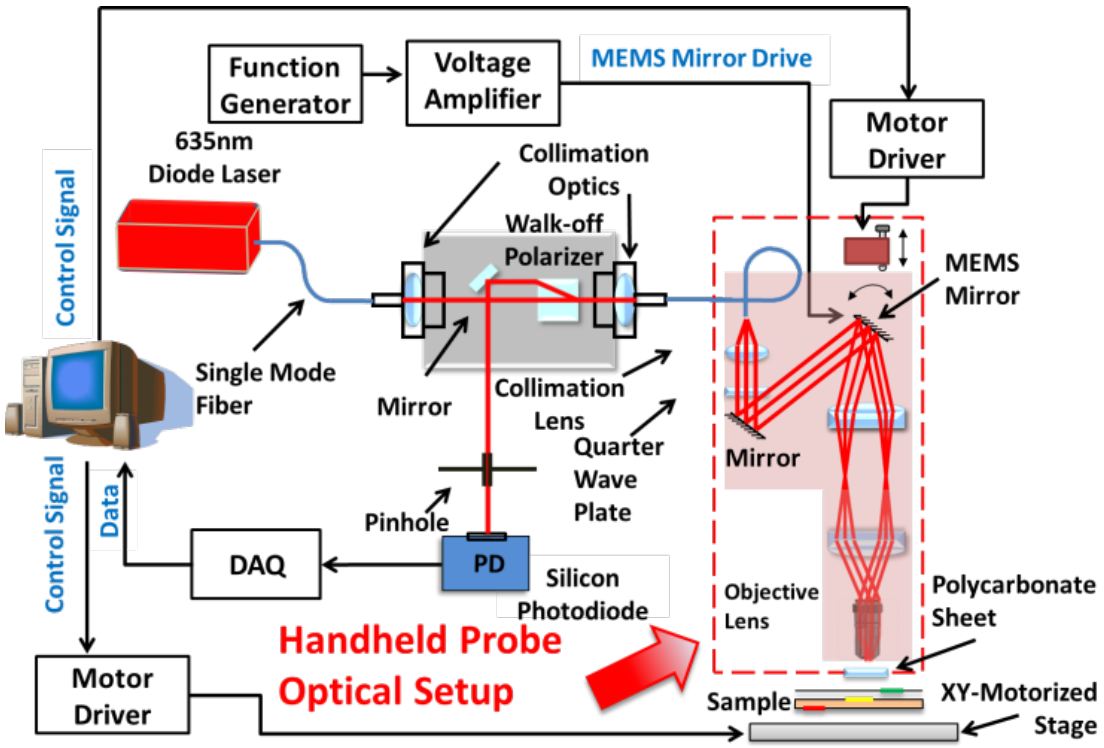


Figure 3.3: Schematic of the MEMS handheld confocal imaging system. The part enclosed in the dashed line box indicates the parts inside the handheld probe, which has the same functionality as a bench-top confocal imaging setup.

## 3.3 Optical design simulations

Figure 3.4 shows the schematic of the optical layout of the 3-lens scanning imaging system using optical simulation software CODE V®. With the total optical scanning angle of the MEMS micromirror of 20 degrees, the field of view of the simulated optical system is 385.7 $\mu$m $\times$ 385.7 $\mu$m.Figure 3.4 (b) indicates the field distortion within the field of view, and Figure 3.4 (c) assets the astigmatic field and distortion with the reference of scanning angle of the MEMS micromirror. These simulation results are evaluated at the focal plane of the whole optical system.

Lateral and axial resolutions are evaluated in Figure 3.5. The diffracted Gaussian

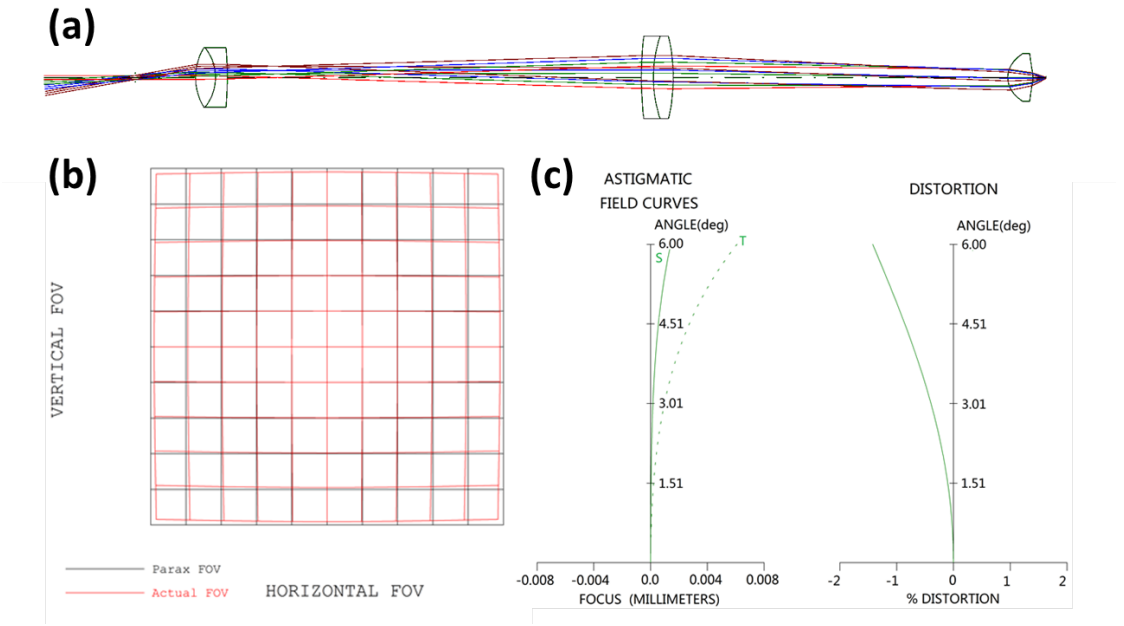


Figure 3.4: Schematic showing the distal scanning objective system simulated in CODE V®. (a) 2D layout of imaging optical system. (b) Simulated distortion in the lateral field of view. (c) Simulated astigmatic field curves and distortion with reference to the scanning optical angle (increase font size: numbers need to be visible).

spot shapes at the focal plane of the 3-lens optical system at different scanning angles are plotted in figure 4 (a), indicating the airy disk shapes over the entire imaged field of view. The quantitative determination of the optical system's resolution is shown in Figure 3.5 (b), indicating the minimum spot size of 0.977 $\mu$m at the intersection position of the main optical axis and the focal plane, while the maximum spot size is obtained to be 8.90 $\mu$m when the MEMS micromirror is rotated by 10 degrees.Figure 3.5 (c) plots the modulation transfer function (MTF) of the four scanning angles and the comparison with the diffraction limit. The drop of lateral resolution from the center to the edge of the FOV indicates the presence of Petzval curvature in our imaging system which undermines the optical performance when the scanning angle of the micromirror is increasing.

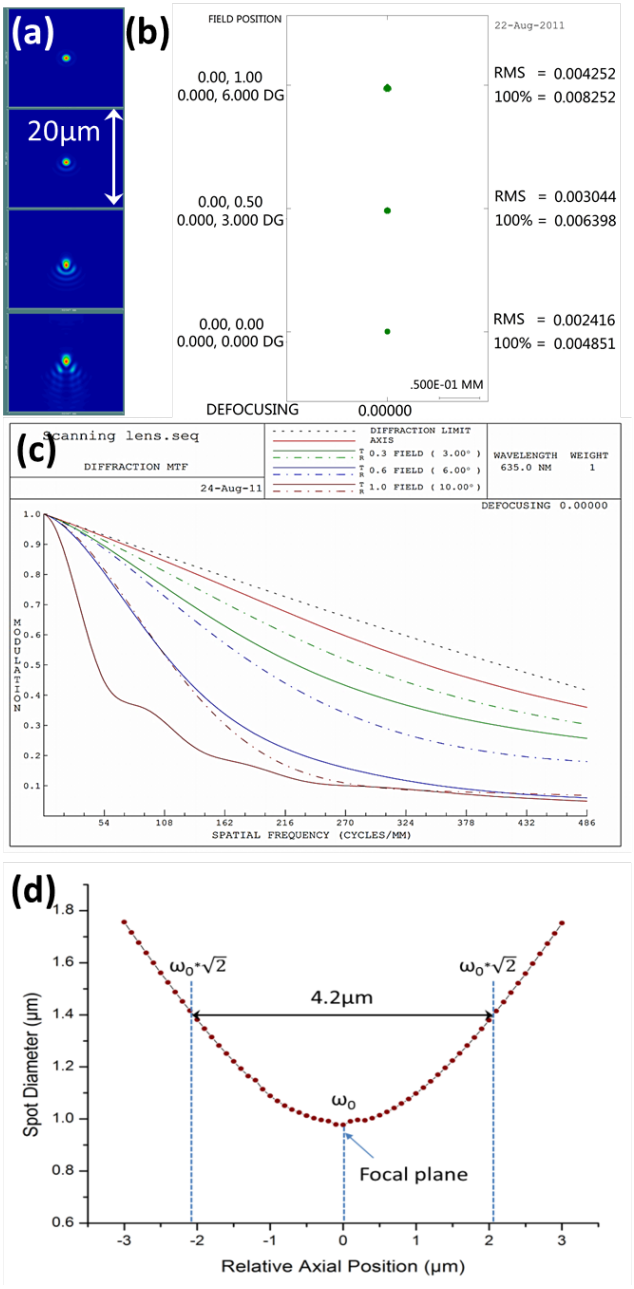


Figure 3.5: Optical performance of the distal scanning imaging system simulated in CODE V®. (a) Focused diffraction Gaussian spot plot at different scanning angles of the micromirror. (b) Quantitative determination of Gaussian spot size with different scanning angles along the focal plane. (c) Modulated transfer function (MTF) for different scanning angles with comparison of diffraction limit.. (d) Simulated Gaussian spot size at difference z-directional positions along the beam-waist area of the imaging system.

Figure 3.5 (d) is the simulated plot of the Gaussian beam size along the beam waist area, determined by plotting the spot diagram with the changing of the observation plane. The spot size increases from $\omega_0$=0.977 $\mu$m at the position of focal plane to the size of $\omega_0 * \sqrt{2}$ which is at the end of the Rayleigh range. This quantitative evaluation indicates the capability of optical sectioning for the confocal imaging.

## 3.4 Handheld imaging system development

The assembled miniature handheld confocal imaging probe is shown in Figure 3.6. The handheld probe was designed incorporating the inner case and the outer one, which are two separate parts, however connected using 4 springs and a pico-motor. Both the inner case and the outer case were first designed and modeled using 3D modeling software SolidWorks® before physically crafted.

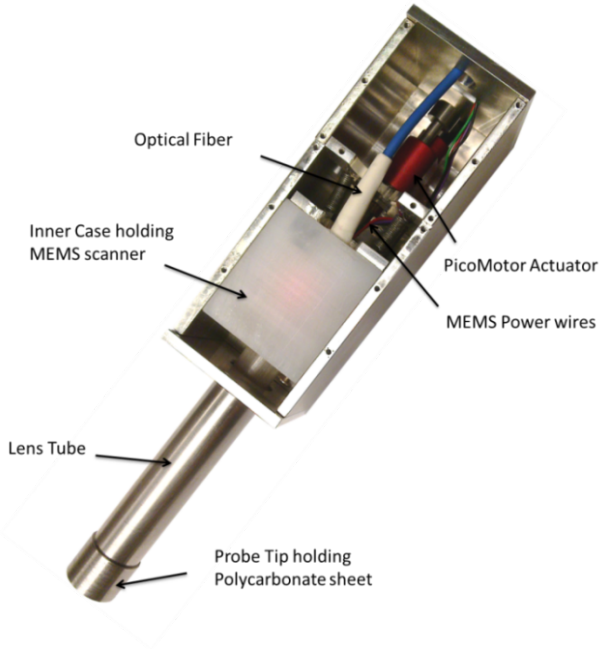


Figure 3.6: Photograph of the assembled handheld confocal imaging probe.

The inner case wall was made of clear polyJet resin (FC720) through a 3D printing objet polyjet process. It holds the printed circuit board where the MEMS micromirror scanner was mounted on. All the optics elements including static mirrors, three lenses and the quarter wave plate were also incorporated. The single mode polarizing maintaining fiber (SMF) and the power wires went into the inner case through a couple adaption ports on its wall, delivering collimated laser beam and actuation voltage onto the MEMS micromirror scanner. The lenses were placed inside the inner lens tube of the inner case. The tiny micro-motor placed between the inner case and the outer case controls the gap between the two cases, therefore controlling the z-directional scan over the depth across the sample. A polycarbonate sheet was placed on tip of the outer case as the probe-sample interface, therefore performing the point-touch imaging scheme to eliminate the interference of sample movement.

The outer case was made of stainless steel, which holds the whole inner piece inside and allows it to smoothly slide in z-direction. The depth sliding of the inner case inside the outer case was realized through the countering force applied by the 4 pulling springs and one pushing pico-motor placed between the inner and outer cases.

A novel acquisition controlling software for this handheld imaging system has been developed using LabView® (National Instruments, Austin Texas) and Java® for improving the usability, image quality, FOV and the rendering frame rate for this Lissajous scanning imaging system ( Figure 3.7). The LabVIEW program captures the data sampled at 1M samples per second from the NI DAQ card and transfers the data blocks periodically through the TCP/IP port. High-level Java programming language was used to enable the parallelization of data processing and acquisition, and to acquire data through TCP/IP protocol from LabVIEW for imaging rendering and real-time

post-processing. The incorporating of real-time processing algorithms including auto-scaling, contrast enhancing, noise reduction increases the computing intensity. The user-friendly GUI guarantees the ease of use for pathologists and surgeons in clinical environment.

Meanwhile, to further enlarge the FOV for the imaging system, mosaic imaging stitching multiple frames acquired by Java while LabVIEW program actuates the moving of the sample stage was developed. The auto-focusing program with the aid of z-directional position controlling of the objective guarantees the right imaging plane for the mosaic imaging. This guarantees the imaging's robustness in the presence of sample moving for handheld imaging. The Java based software handles the image processing and rendering in a high efficiency, ensuring a real-time imaging rate (2 fps) for the whole imaging system.

## 3.5 Experimental Results and discussions

### 3.5.1 Bench-top Setup Imaging Results

As verification for the handheld confocal imaging idea, desk-top MEMS enabled confocal imaging system was first developed and brought to UT Health Science Center (UTHSC). 7 different types of stained oral cancer tissues were investigated as samples. Those sample tissues used were made by a protocol process of slicing, staining and fixed on a microscope glass slide, before taken from the UTHSC patients. A Leica 10X objective lens was used and a FOV of 1.85mm by 1.85mm was achieved for the bench-top MEMS based confocal imaging setup. Comparisons with images taken from a commercial Olympus microscope under a Leica 2X magnification objective lens were made to evaluate the MEMS based portable confocal imaging system's optical and clinical

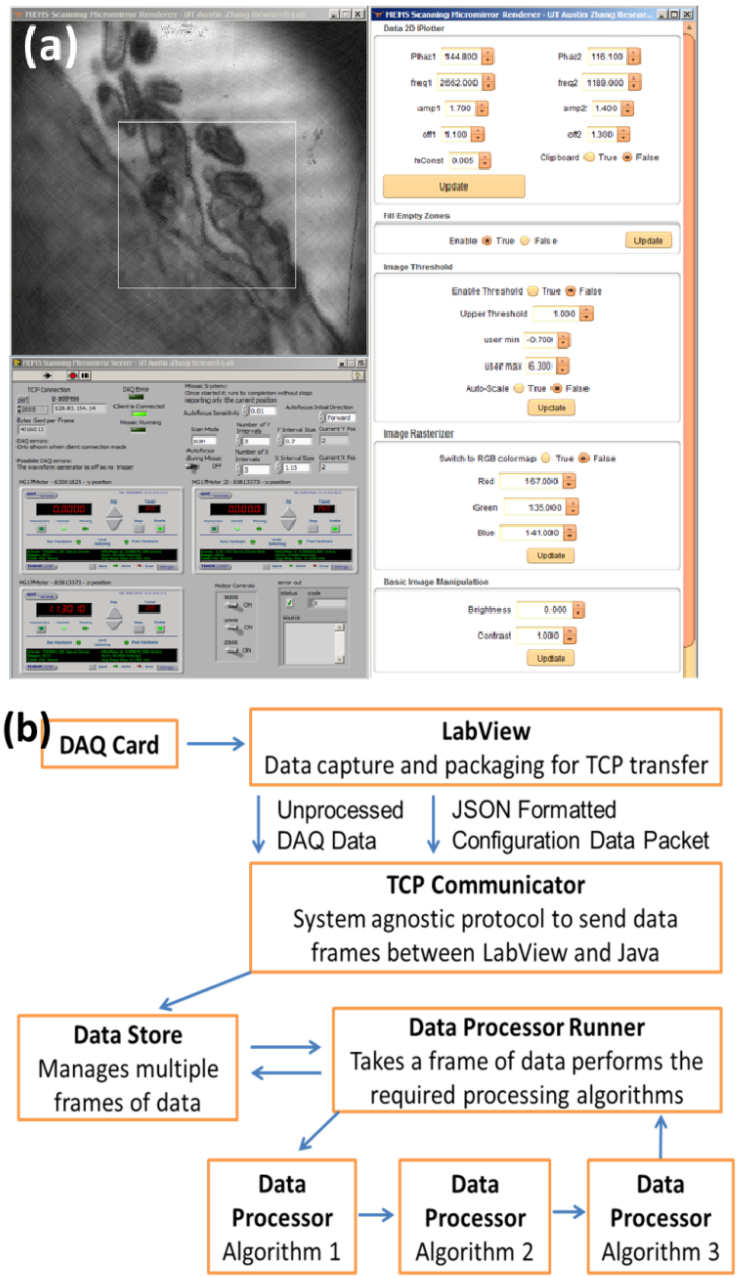


Figure 3.7: Miniature confocal imaging user interface and software architecture. (a). The Java & LabVIEW software GUI interface enabling the real-time modifications to the processing tool used to render images from the lissajous scanning. (b). Architecture diagram illustrates the flow of data from acquisition to the completion of data processing where the data is then rendered to the screen for the user.

performances.

Figure 3.8 shows the comparison between the false-color treated figures from our MEMS enabled desk-top confocal imaging setup and those from a laboratory microscope. In Figure 3.8 (a) and (b) a stained biopsy of giant cell fibroma mounted on a glass slide were examined, while in Figure 3.8 (c) and (d) the stained biopsy of peripheral ossifying fibroma mounted on glass slide were examined. The blood vessel areas as well as the neoplasm area outlined by the uncontrolled growing cells are clearly visible. To ease the diagnosis of the whole sample area, mosaic imaging was developed by fast stitching frames imaged real-time while linearly translating the lateral position of the sample stages in x and y directions. Figure 3.9 compares the FOV acquired from MEMS confocal desk-top imaging setup with the control image from a Leica SP2 AOBS microscope. The sample is a biopsy of benign oral tissue H&E stained and mounted on a glass slide. Detailed features outlining individual cells are visible, while the whole FOV is further increased to 8.5mm by 11.5mm. The area enclosed with yellow dotted box on Figure 3.9 (a) indicates the area of control image acquired from Leica microscope in Figure 3.9 (b)

### 3.5.2 Handheld Confocal Imaging System Calibration

Optical performances including lateral and axial resolutions, and field of view were examined for the assembled handheld confocal imaging system. A lateral resolution around 3 $\mu$m referring with the FOV of 300 $\mu$m by 280 $\mu$m was demonstrated by this handheld imaging system, by the imaging of elements group 6 and 7 of the standard US Air Force resolution target, as shown in Figure 3.10.

Mosaic imaging for handheld imaging acts as a functionality to acquire images

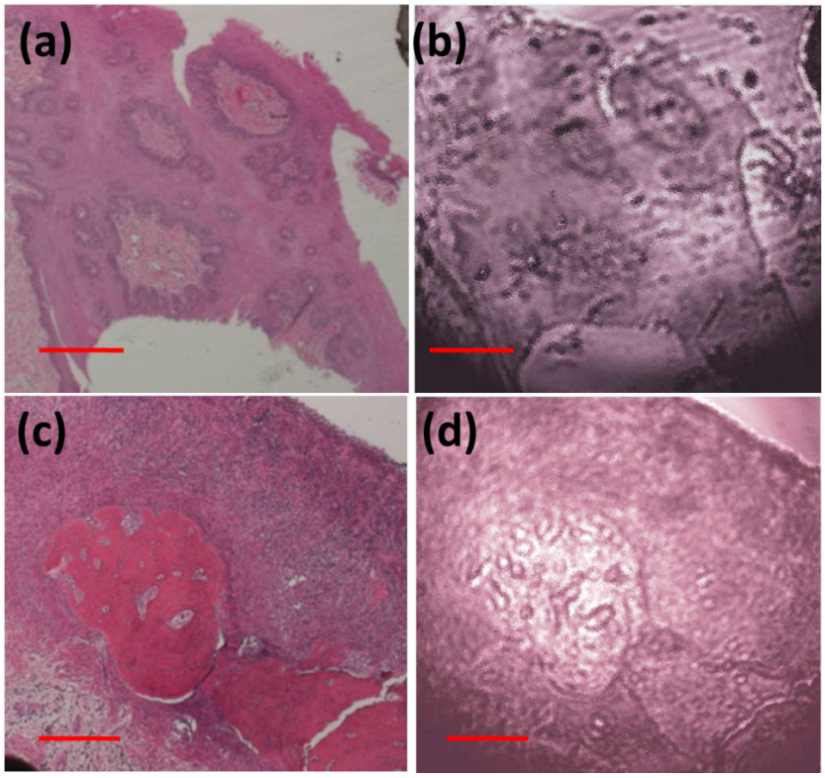


Figure 3.8: Comparison of imaged obtained from desk-top MEMS confocal imaging setup and those from a commercial Olympus microscope under a 2X objective , (a) and (b) are compared images for a stained biopsy of a giant cell fibroma from a patient, (c) and (d) are compared images for the stained biopsy of a Peripheral Ossifying Fibroma from a patient. Scale bars are 100 $\mu$m.

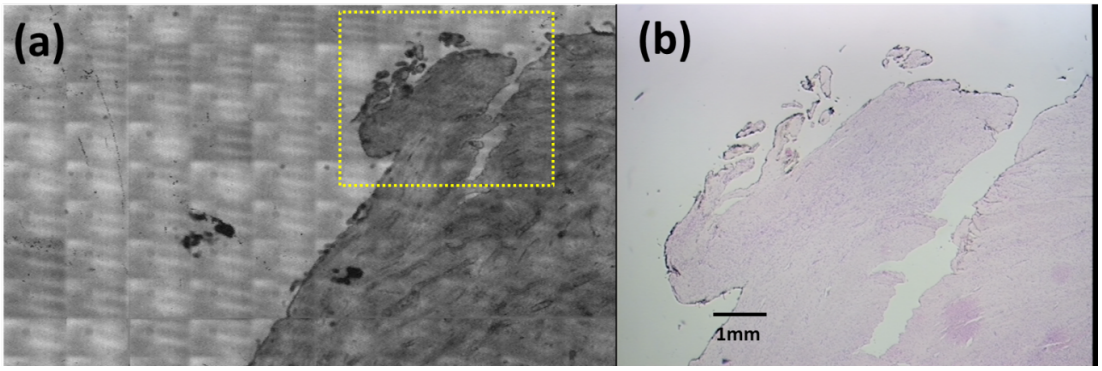


Figure 3.9: FOV Comparison of mosaic image obtained from desk-top MEMS laser scanning confocal imaging setup and those from a commercial Olympus microscope under a 2.5X objective (b).

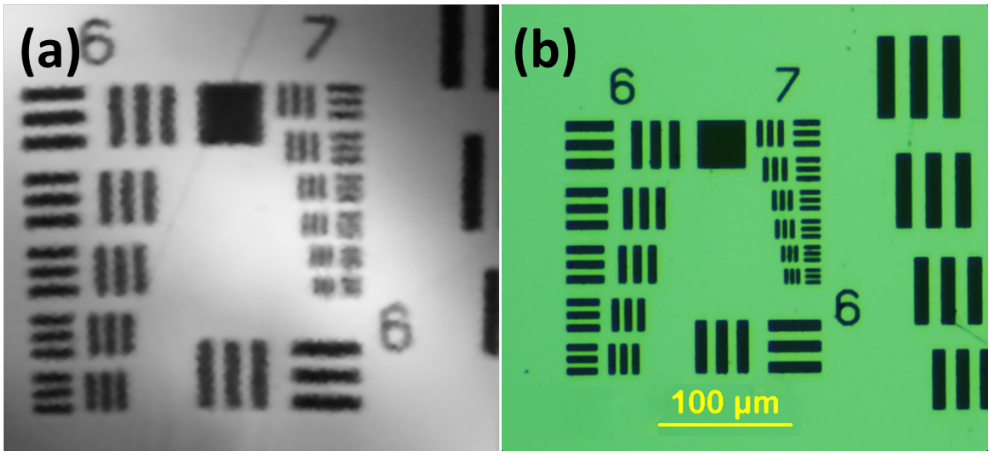


Figure 3.10: Imaging calibration using USAF resolution target. (a) The image of the elements of group 7 of a USAF 1951 standard resolution target, acquired using MEMS enabled confocal system. (b) Image of the USAF target using Olympus BX51 microscope.

with similar specification to laboratory microscopes in terms of FOV and resolution while observing histological sample slides. Aimed by the actuation of motorized linear stages the FOV for the handheld confocal imaging setup was increased up to 6mm by 8mm, as indicated in Figure 3.11 using the same USAF resolution target as shown in Figure 3.10. To demonstrate the functionality of 3D sectioning imaging for handheld confocal imaging probe, the axial resolution is verified in Figure 3.11. The measured back reflectance light intensity distribution against the axial position around the focal plane was examined, which presents good accordance with the fitted Gaussian function curve. The measured full width half maximum (FWHM) of the fitted Gaussian function for the reflection intensity distribution is 5.8 $\mu$m, which is the length of the focus beam spot beam waist Rayleigh range.

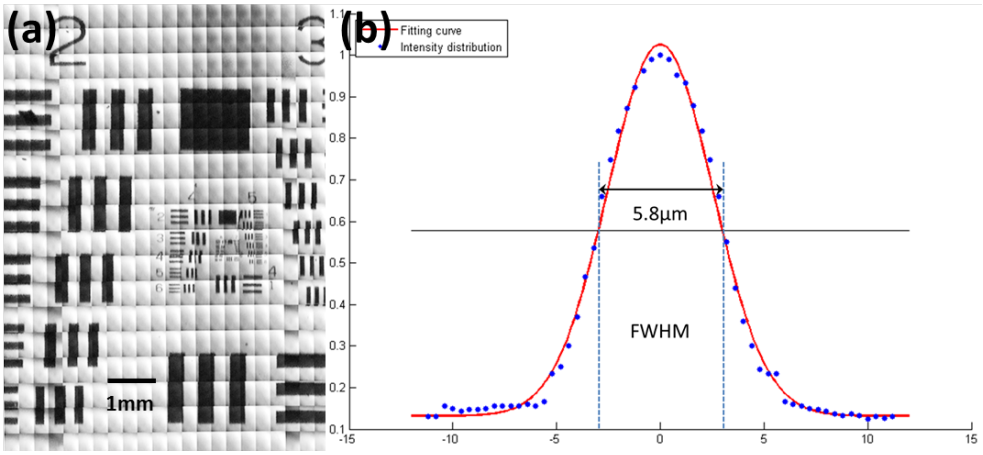


Figure 3.11: Mosaic imaging for extended field-of-view. (a) Real-time mosaic imaging results of a part of the USAF target showing a FOV of 6mm by 8mm. (b) Experimental result of the axial resolution, which is 5.8 $\mu$m.

## 3.6 Handheld Confocal Probe for Oral Tissue Imaging

The complete MEMS handheld confocal imaging system was built and placed on a portable cart, integrated with necessary electronic and optical accessories. Clinical experiments investigating H&E stained oral cancer tissues as well as gross oral tissues were taken in UT Health Science Center (UTHSC) on this portal system. Figure 3.12 (a) shows the mosaic image for a stained benign oral tissue biopsy mounted on glass slide from the handheld confocal imaging setup, whose FOV is measured to be 6mm by 8mm. Interference noise brought by the air gap between the cover slip and the sample glass slide blurs the overall view. However when zooming into locale areas as shown in Figure 3.13 (a), details specs including the outlines of cells could be recognized, showing good accordance with the control image shown in Figure 3.13 (b), which is obtained from a Leica SP2 AOBS microscope, using a 20X magnification objective lens.

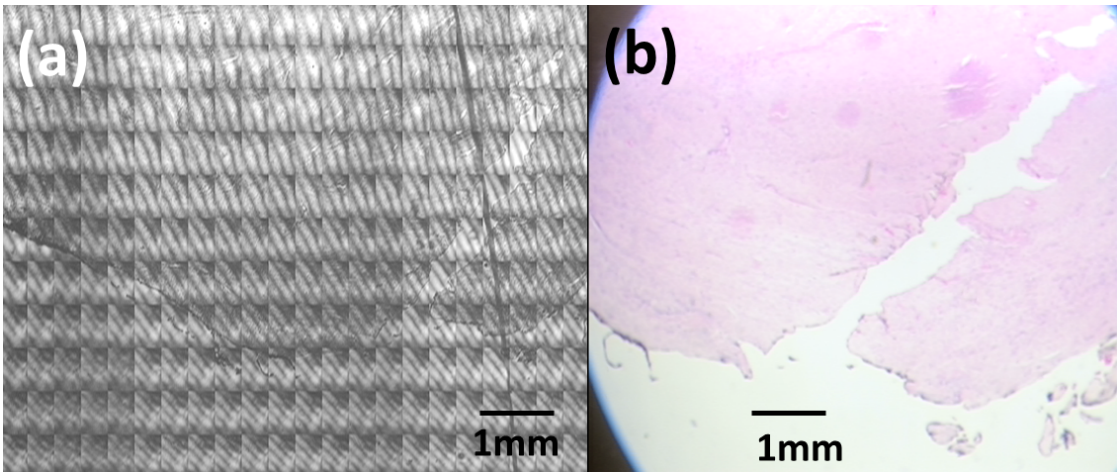


Figure 3.12: (a) Mosaic microscopic of a benign oral tissue sliced, stained and mounted within a glass slide (b) Comparison image from Leica microscopic using a 2.5X objective lens

Figure 3.14 is the mosaic image obtained from a gross Peripheral Ossifying Fi-

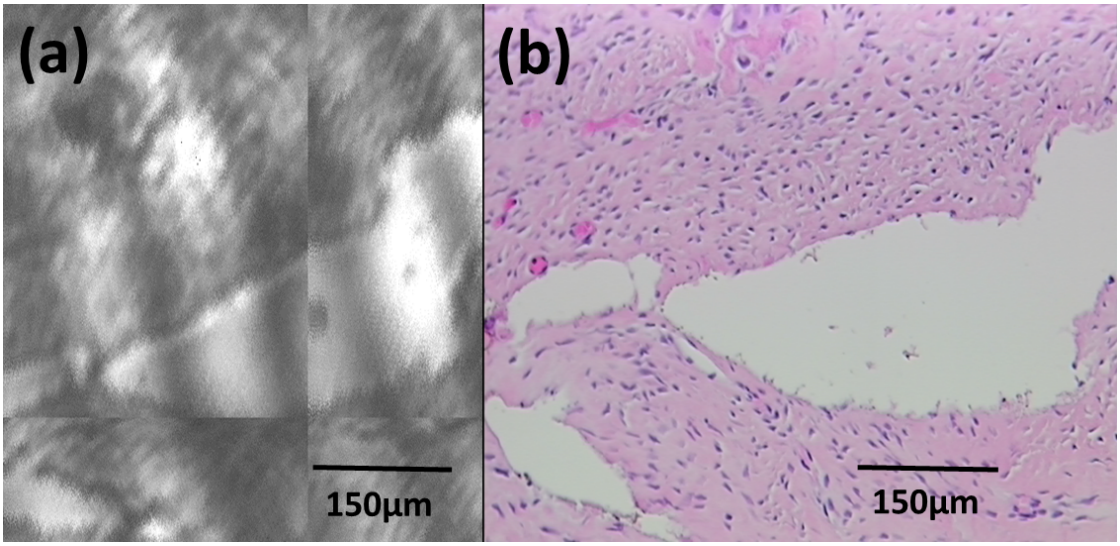


Figure 3.13: (a) Sub-area of the mosaic microscopic image (b) Leica microscopic image from a 20X objective lens.

broma tissue. The varying depth along the surface of the gross tissue adds to the discontinuity of obtained images' signal to noise ratio (SNR), while the micrometer level resolution handheld imaging observing the presence of cellular level structure of the in-vivo tissues addressed the incapability of traditional confocal microscopes to observe them in a fast and convenient way.

## 3.7 Summary

This chapter demonstrates a functional prototype of handheld confocal imaging probe utilizing the MEMS micromirror as core scanning device with versatile imaging pattern control. Cellular-scale lateral resolution around 3 $\mu$m with FOV up to 300 $\mu$m $\times$ 280 $\mu$m was achieved at 2 frames per second. To ensure a real-time imaging rate and provide a user-friendly operation interface, imaging controlling software utilizing LabView and Java GUI integrated with image processing and rendering algorithms for

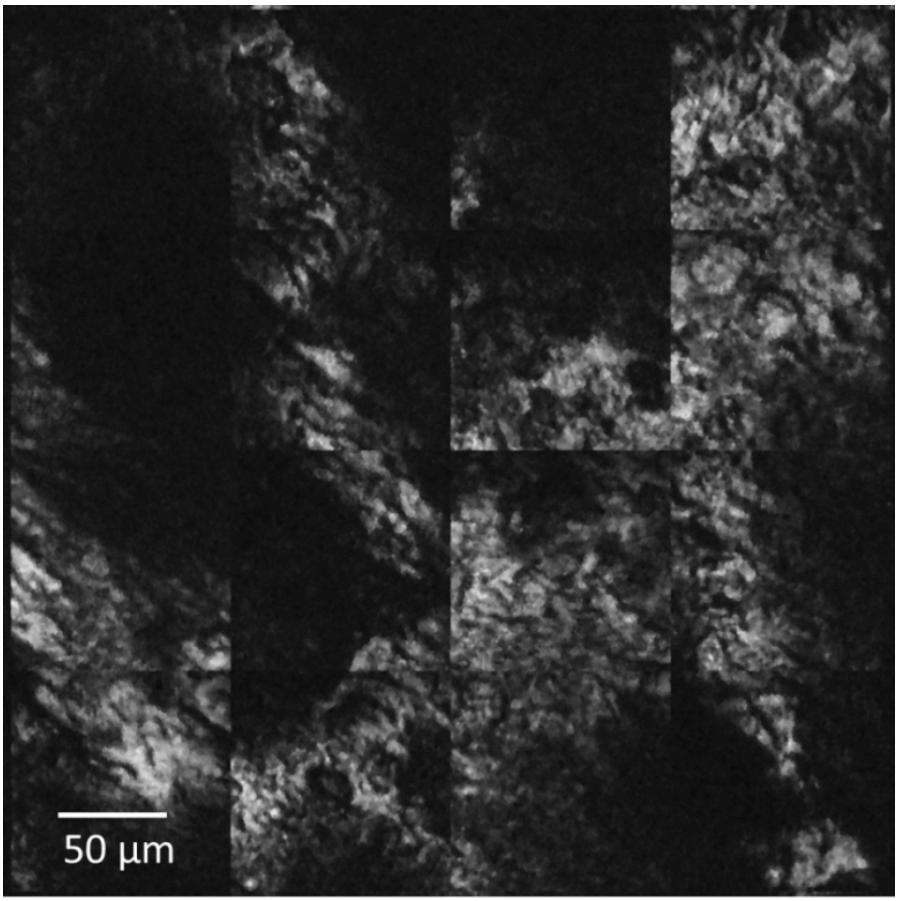


Figure 3.14: Mosaic image of a gross Peripheral Ossifying Fibroma tissue from the handheld confocal imaging probe.

lissjous scanning was developed. Additional functions including mosaic imaging coupled with auto-focusing were developed for FOV enhancement up to 6mm by 8mm at suitable axial resolution of 5.8 $\mu$m for the better examination with extended visible area for pathologists. Benign oral tissue and carcinoma tissues including Neurofibroma, Peripheral Ossifying Fibroma, giant cell fibroma, wart and Verrucous Epithelial Hyperplasia in the presence forms of stained biopsy, paraffin block and gross tissue were examined for the the handheld imaging system in the UT Health Science Center, showing a good accordance with control images acquired from white field Olympus and Leica laboratory microscope and the feasibility for clinical diagnosis. The compact handheld confocal imaging system shows great promise for clinical early oral cancer diagnosis and treatments.

# Chapter 4

# Handheld Optical Diffuse Reflectance Hyperspectral Imaging (HSI) Probe for Skin Cancer Diagnosis

The designs and experiments described previously in this dissertation clarified the use of a portable, handheld laser-scanning microscope in various imaging modalities could well fit the goal towards early detection of various types of epithelial cancer. The capabilities of the silicon electrostatic combdrive driven MEMS micromirror used is well suited to be incorporated into a miniature handheld imaging probe. However, moving forward there is a need calling for higher signal to noise (SNR) and sensitivity level, finer details revelation and more robustness for instrument use. In the following chapters, our endeavors in the following directions will be summarized: 1). Fluorescence imaging increases in maximum imaging depth and, particularly, in the gain of contrast extraction. 2). The application of an array of fluorochromes has made it possible to identify cells and sub-microscopic cellular components with a high degree of specificity amid non-fluorescing material. 3). Through the use of multiple fluorescence labeling, different probes can simultaneously identify several target molecules simultaneously. 4). Use scanning status feedback controlling to track the trajectory of MEMS's mirror's scanning path, avoid the manual prediction of the phase different between electrical actuation signal and mechanical movement, which is subject to changes due to environmental noises. 5). Use real-time mosaic imaging: significantly reduces excited area of specimen and increases acquisition rate at constant SNR; several ROIs of any

shape can be defined and used simultaneously.

The clinical need for noninvasive skin cancer detection devices has led to intensive commercial and research efforts to develop novel instruments for imaging, spectroscopy or the combination of both [65]. In particular, portable hyperspectral imaging (HSI) screening devices are highly desirable for the sensitive, biopsy-free characterization of diseases in situ and precision guided microsurgery. This will not only reduce the millions of costly, unnecessary biopsies performed every year, but will also make the diagnosis and treatment for diseases like melanoma more convenient and timely. A single-point diffusion reflectance spectroscopic (DRS) probe has been developed for the noninvasive diagnosis of skin cancer using optical fiber based probes placed in gentle contact with the skin surface [66]. The high accuracy of the preliminary results demonstrated the potential of DRS for non-invasive, real-time diagnosis of skin cancer. However, these results suffer from inaccuracies from "sampling errors" inherent in point measurements. While DRS provides detailed physiological data that can be useful for diagnosis, it does not allow for mapping or imaging of skin sites.

This chapter details the design and characterization of a MEMS scanner based handheld hyperspectral imaging system combining the functionalities of diffuse reflectance imaging for skin cancer diagnosis. Integrating the silicon combdrive dual-axis micromirror, this new system is capable of hyperspectral and depth-sensitive imaging with adjustable field of view and spatial resolution.

## 4.1 Skin cancer overviews

Skin cancer is currently the most common cancer type in the world with prevalence rates estimated to be 1 in 5 [67]. Over 2 million cases of skin cancer are diagnosed

annually, which is more than all other cancers combined [68]. The most common types of skin cancer are Basal Cell Carcinomas (BCC) and Squamous Cell Carcinomas (SCC), which rarely result in fatal cases when detected in early stages. Melanoma skin cancers account for less than 5% of skin cancer cases, but they also cause the most deaths. The 5 year survival rates are greater than 90% for melanomas that are discovered and treated in the initial stage of development. These survival rates can drop to as low as 50% once they spread to nearby lymph nodes. Far more common are non-melanoma skin cancers, of which 13 million people (5% of the U.S. population) are estimated to have at some point in their lives. The estimates for non-melanoma skin cancer incidence rate are between 0.9 and 1.2 million [69, 70]. Non-melanoma skin cancer has been estimated to be 5 times more prevalent than breast and prostate cancer [68]. Previous estimates show that non-melanoma skin cancer (NMSC) was the fifth most costly cancer to treat in the across all Medicare recipients [71] and across most treatments.

A hallmark of tumor development is the sign of the rapid growth, tumor cells are distinguished by enlarged cell nuclei [72] with respect to the overall cell size. The development is also characterized by increased metabolic rate which is correlated with the density of mitochondrion and NADH concentration [73, 74]. When these tumors grow they produce Matrix Metalloproteinases (MMPs) that break down collagen, making it easier for the tumor to expand into the deeper layers of skin [75, 76]. To supply the growing demand for fueling a constantly growing tumor, genes promoting angiogenesis are expressed, and a dense network of blood vessels are formed. These tumor blood vessels are non-uniform in structure and are porous, enhancing the chances for cancer to leak out into the bloodstream and metastasize.

The visual obscurity of tumor morphology and physiology can make early de-

tection a difficult task for dermatologists, particularly in the initial stages of dysplasia. Tumor resection is a common course of action once they are discovered, however as with any surgical procedure, there are associated risks of morbidity. Additionally, healthcare costs have been a burden not only to patients but also health facilities. Seeking the methodology of tracking the development of skin tumor, the cytomorphology and physiology of tumor tissues can be used to profile a malignant lesion, and subsequently treat it if necessary. Densely packed cells with enlarged nuclei, the proliferation of non-uniform and leaky blood vessels, collagen breakdown, and concentration of metabolic biomarkers are some of the main micro and macroscopic features to consider when developing a cancer imaging strategy.

## 4.2 Optical diffuse reflectance HSI of cancer

Point scanning imaging combined with hyperspectral imaging approach as mentioned in Chapter 2 was utilized for handheld optical diffuse reflectance imaging of skin cancer. Point scanning approach obtaining images spatially and spectrally through resolved diffuse reflectance acquisition is performed by focusing and scanning a beam of light across a sample. The signal returning from each point of scan is dispersed with a grating or prism onto an array detector such as a line-scan charge coupled device (CCD) or a multi-cathode photomultiplier tube (PMT). To process the acquired spectra for optical and physiological property estimation, a spectral density of bands that is high enough to be considered a hyperspectral signature was recorded.

Due to the well-defined source-collector geometry of optical probes, it is possible to draw quantitative conclusions from the spectral images and attain optical and physiological property maps. Models that the optical spectra are fit to can be analytical

models such as, diffusion theory [77, 78], computational models such as Monte-Carlo [79, 80], or empirical models such as the look-up-table [81]. All of these models generate a reflectance value that would be observed in response to the sampling of a medium of a particular reduced scattering and absorption. Many algorithms are used for spectral fitting of reflectance spectra, including least squares support vector machines which have been used to achieve tight fitting between the model and the reflectance data collected at high rates of speed [82].

We present a hyperspectral diffuse optical fluorescence imaging system that acquires a widefield spectral cube of image data (x,y,λ). The spectra at each pixel was be processed for the estimation of multiple optical and biological properties and formed into respective property maps for analysis. The acquisition of spectral and spatial information multiplies the diagnostic strengths of dermal inspection. The laser scanning design allows for configurable diffuse reflectance collection geometry for depth sensitive images.

## 4.3 Optical diffuse reflectance HSI probe instrumentation design

The optical diffuse reflectance HSI system (Figure 4.1) used a 488nm-514nm argon laser (Coherent Medical, Baltimore Maryland) as excitation source. The illumination light was coupled into a single mode optical fiber (SMF) which transmits the excitation laser light into the handheld probe, where a lens fixed to the terminated fiber end collimates the beam.

Guided by the SMF which was attached on the customer designed handheld probe using a pigtailed connector, this illumination was transmitted through a hot (dichroic) mirror (NT69-865, Edmund Optics, Barrington, New Jersey) with 520nm cutting-off

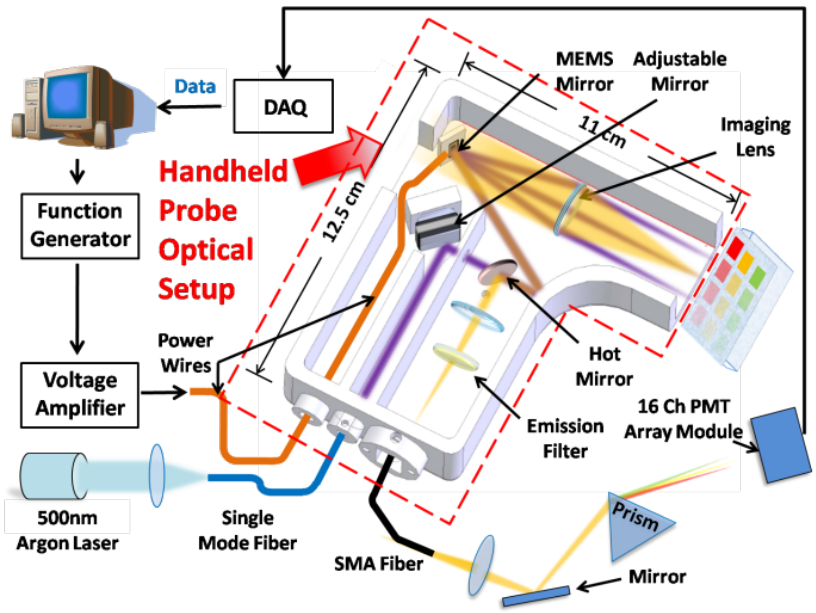


Figure 4.1: Schematic of the handheld MEMS hyper-spectral imaging system, the packaging design of the probe, and the signal flow for the actuation of the MEMS scanning mirror and the data acquisition from 16Ch PMT.

wavelength. After passing through the dichroic, the illumination beam is deflected onto the surface of the microelectromechanical (MEMS) scanning mirror before being focused by the objective lens (AC127-050-A, Thorlabs, Jessup, Maryland) onto the sample. The fluorescence light emitted from the quantum dots (QDs) sample was simultaneously de-scanned by the MEMS mirror and reflected by the hot mirror onto the collection arm, where it is coupled into a multimode SMA (SubMiniature version A) collection fiber leading out of the probe. The collection fiber terminates on a spectral acquisition module, where the collection light was spectrally dispersed by a triangular prism onto the photocathodes of a 16 channel array photomultiplier tube (PMT) (H7260, Hamamatsu, Japan).

Data acquisition was performed using a 16 Channel analog input NI PXIe-6358 data acquisition card (DAQ) (National Instruments, Austin Texas), in concert with a

LabVIEW® (National Instruments, Austin Texas) and Matlab® based software to simultaneously acquire 15 bands of fluorescence signal. The remaining one Analog Input (AI) channel was used to synchronize the acquisition timing with the scan signal for image rendering. The MEMS scanning mirror is actuated in resonant modes on both axes upon applying the sinusoidal scan signal from function generators (Tektronix, Beaverton Oregon).

As shown in Figure 4.2, the handheld imaging probe consists of a case cover and the main case which incorporates the MEMS scanning mirror and the optical elements including lenses, reflection mirrors and the short-pass dichroic mirror. The handheld probe interfaces the single mode excitation laser fiber, the SMA collection fiber and the power delivery wires through three I/O ports. The handheld probe measures 13cm $\times$ 11cm $\times$ 3.7cm in outer dimensions, the pieces were first designed and modeled using the 3D modeling software SolidWorks® before physically crafted by a ZCorp® 3D printing technique using the material of plastic powder, and adhered by cyanoacrylate. Peripheral serving facilities for the handheld imaging probe including the dispersing optics and the 16 Channel PMT were mounted onto an optical board.

The optical adjustments for the alignment of the SMA collection fiber were made possible through two degrees of freedom design. First a one dimensional lateral adjustment screw was used at the collection fiber port for vertical position adjustment. The lateral direction adjustment was realized through the use of an adjustable mirror stage for the mirror reflecting the excitation laser beam, which has pitch and roll adjustment screws on it. Thus focusing of the emitted fluorescence light into the core of the collection fiber was guaranteed. While tuning the reflection angle of the first mirror to adjust the focusing of fluorescence beam, the position and spatial angle of the MEMS mir-

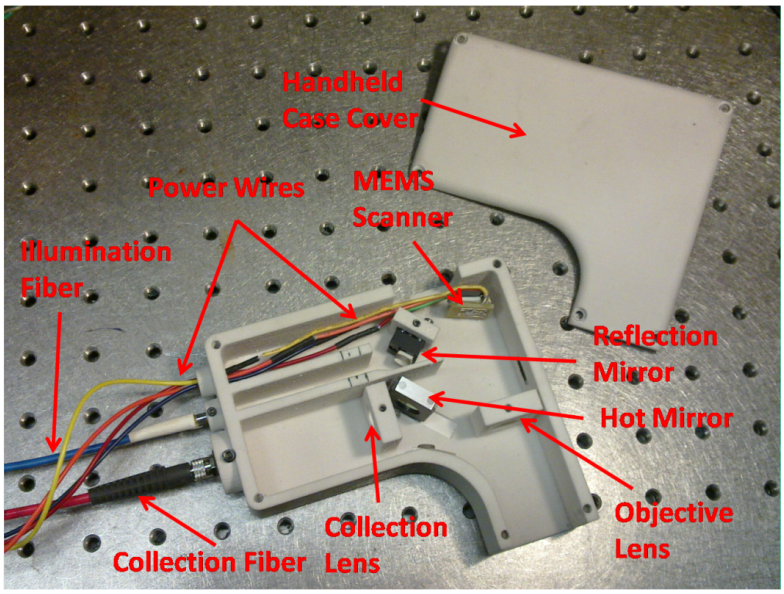


Figure 4.2: Photograph of the assembled handheld MEMS hyper-spectral imaging system shows the case cover, and the main case with the MEMS scanning mirror and the optical elements inside.

ror were also adjusted by tuning the stage where the PCB holding MEMS mirror was mounted on, to ensure the excitation beam is hitting the center of it.

## 4.4 Ray-tracing imaging performance simulations

Figure 4.3 (a) shows the schematic of the optical layout of the optical scanning imaging system using optical simulation software CODE V®. With the total optical scanning angle of the MEMS micromirror of 20 degrees, the field of view of the simulated optical system is 13.4 mm $\times$ 13.4 mm. Figure 4.3 (b) shows the simulated distortion in the lateral field of view, which indicates the optical path difference (OPD) with both tangential and sagittal directions within that field of view for three wavelengths: 520nm, 580nm and 610nm.

The selection of the simulation wavelengths are based on the emission spectrum

of the sample we use.

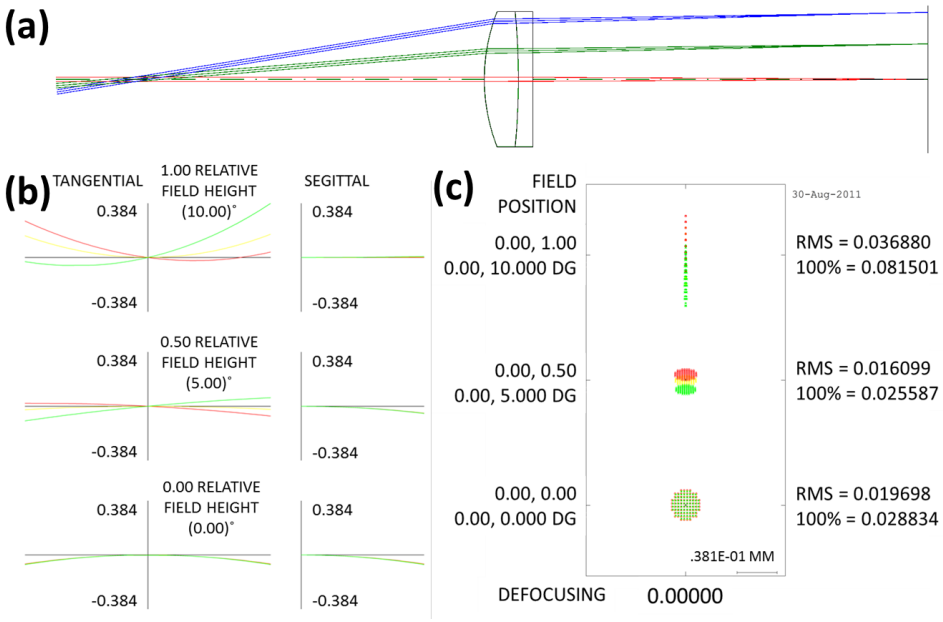


Figure 4.3: The optical layout of the scanning objective system simulated in CODE V. (a) 2D layout of imaging optical system. (b) Simulated distortion in the lateral field of view. (c) Simulated spot diagram for three wavelengths with reference to the scanning optical angle.

The quantitative determination of the optical system's resolution is shown as well, indicating the minimum spot size of 19.7 $\mu$m at the intersection position of the main optical axis and the focal plane, while the maximum spot size is obtained to be 36.90 $\mu$m when the MEMS micromirror is rotated by 10 degrees. The position offset caused by the wavelength difference of illumination was marked by different color patterns.

## 4.5 Phantom sample preparation for optical diffuse reflectance HSI

We characterized the MEMS hyperspectral imaging system using both Poly-dimethylsiloxane (PDMS)-Quantum Dots (QDs) phantoms and biological samples such as porcine epithelium. A multilayer QD PDMS phantom sample was fabricated for

evaluating the quality of depth sensitive and hyperspectral imaging simultaneously (Figure **??**). Micro-contact printing ($\mu$CP) is used to pattern QDs on the surfaces of multi-stack PDMS thin layers. Each spin-coated PDMS thin-layer is 200 $\mu$m thick, infused with titanium dioxide to simulate the scattering in tissue. The sample contained a 3x3 QD pattern array, each depth containing 3 different colors on it.

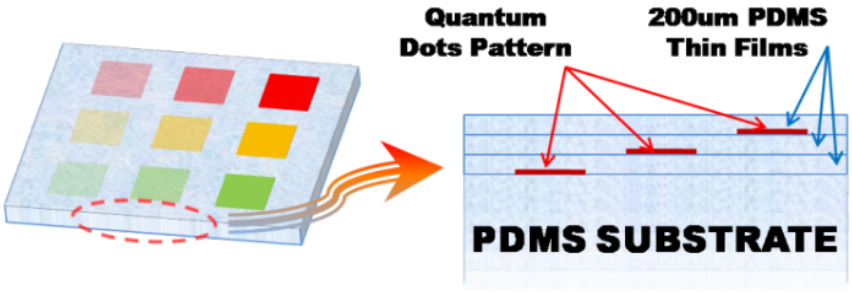


Figure 4.4: Schematic of the $\mu$CP fabricated QDs multilayer PDMS sample. Left: Isometric View. Right: Side View.

## 4.6 Hyperspectral optical diffuse reflectance imaging results

The fluorescence images of the phantom sample under 15 wavelengths acquired simultaneously are shown in Figure 4.5. Yellow and red QDs patterns have much stronger fluorescence signal yield out at the shallower columns, while the green QDs pattern does follow this rule due to the distribution uniformity.

Using the images of 3 peak wavelengths for each color, the pseudocolor image was merged and rendered (Figure 4.6a), which shows good preserving of features when comparing to the mosaic image from commercial microscope (Figure 4.6b). The resolution of the image is visually measured as roughly 100$\mu$m, suggesting that for a confocal arrangement (zero source-detector separation), the resolution is related to pinhole size.

Source-detector (SD) separation is radial distance on the sample surface between

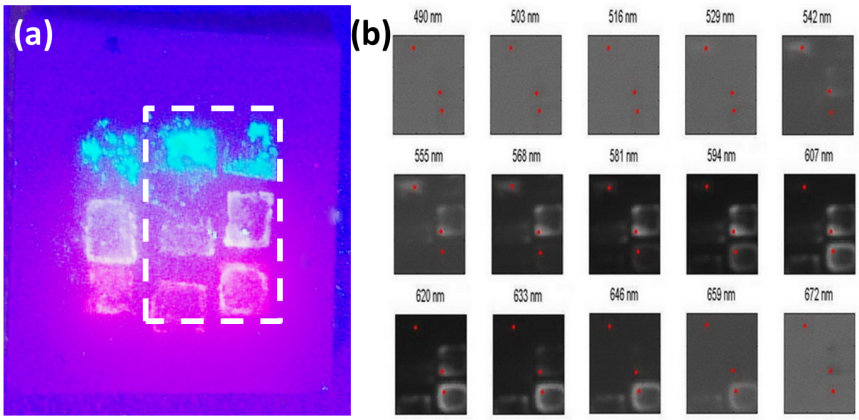


Figure 4.5: (a) The photograph of the QD sample under UV illumination, the area inside the dashed box is that imaged from the hyperspectral imaging system. (b) Fluorescence images of the phantom sample under 15 wavelengths acquired simultaneously.

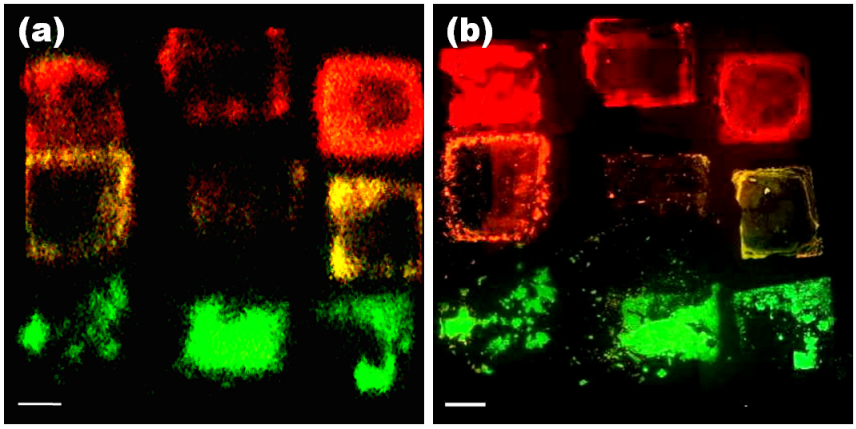


Figure 4.6: Comparison of images acquired using MEMS HSI and Olympus microscope. (a) Pseudocolor image merged from 3 peak wavelength images. (b) Microscope image using Olympus BX51 microscope. Scale bars are 1mm.

the source spot and the spot imaged by the collection aperture. This radial separation will be proportional to the mean sampling depth of the collected photons due to the diffuse nature light scattering in turbid samples. Offsetting the collection from the source spot on the sample creates a Source-Detector 'σ' separation. Eq. 4.1 describes the relationship of the fluorescence intensity comparison collected between the deeper and shallower layers:

$$\frac{I_{QD\_shallow}}{I_{QD\_deep}} \propto \frac{1}{\sigma} \tag{4.1}$$

Here we refer to the collected fluorescent light intensity from the quantum dots layers, and σ stands for different source-detector separation values.

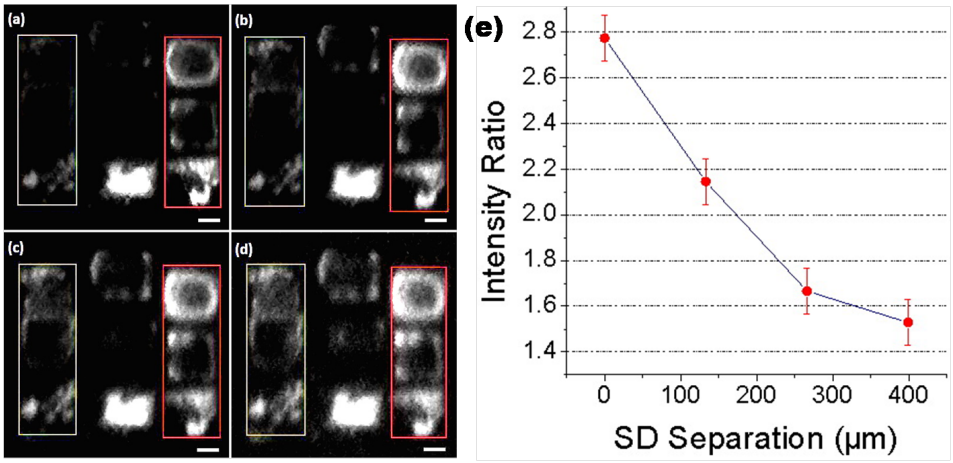


Figure 4.7: (a)-(d): Depth sampled images for four different SD separations. Fluorescence intensities within selected regions of the image were calculated to obtain ratios of shallow to deep intensities. Red and yellow outlined regions contain shallow (200 $\mu$m) and deep (600$\mu$m) QDs respectively. (e) Mean intensity ratios of shallow vs. deep quantum dot stamps over 0 to 399 $\mu$m SD separations. Scale bar is 1mm.

In Figure 4.7 our different SD separations were performed, showing the sampling depth selectivity in terms of the ratios of fluorescence intensities between the shal-

lowest and deepest layers. Each image was normalized to full dynamic range so that the trend could be seen qualitatively in the figure. Figure 4.7e implies the diminishing trend of the intensity ratios with increasing SD separation. This implies that fluorescence emanating from more deeply implanted quantum dots account for an increasing percentage of the overall collected light as SD separation increases, as indicated by previous studies [83]. Here we have demonstrated that by increasing the SD separation from 0 to 400 $\mu$m, the selectivity of the deepest layer increases by a factor of 1.83 times. While boosting the relative signal of deeper features, close inspection of Figure 4.7 will reveal that SD separation has an adverse effect on spatial resolution and signal to noise ratio.

Upon the observation of the collected spectra from the handheld hyperspectral imaging system with comparison with that from a commercial standard spectrometer, the spectral broadening effect of the fluorescence signal can be seen. This spectral broadening from our system was due to the low magnification of the collection optics, combined with the relatively large size of the collection fiber (1mm). The large collection fiber image on the PMT cathode plane was necessary to increase the signal to noise ratio (SNR) to acceptable levels, although at the expense of spectral resolution. QD signal from red, yellow and green patterns were measured across the visible spectrum, demonstrating a spectral resolution of 20nm (Figure 4.8). Due to the dichroic mirror's 500 nm cutoff and transient slope, the green spectrum is slightly attenuated on its 'blue' side, giving the impression of a peak at 520 nm. A commercial spectrometer (Ocean Optics, Dunedin Florida) was used for comparison to the spectral performance of our handheld hyperspectral imaging system. The spectra from both the commercial spectrometer and our system were normalized for comparison.

Biological imaging potential was demonstrated using quantum dots with 2 differ-

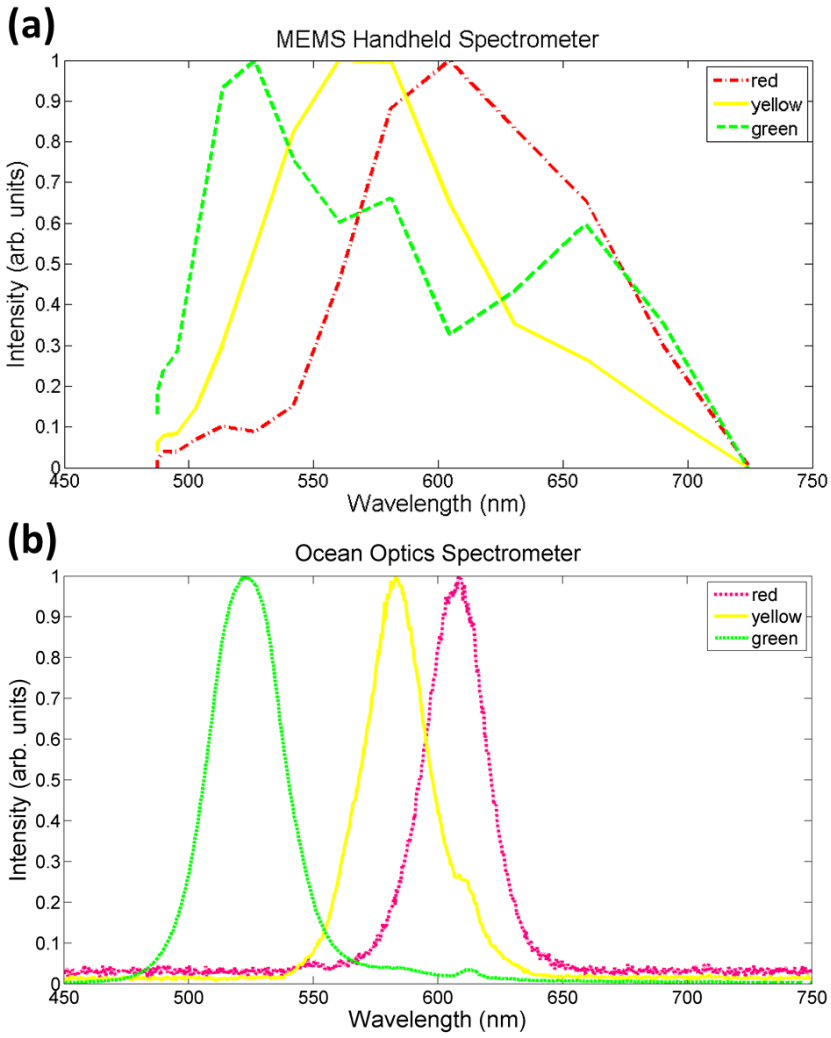


Figure 4.8: Comparison of the spectrum acquired for the quantum dots sample from handheld hyperspectral imaging probe and commercial spectrometer. (a) spectrum of the 3 color quantum dots on the red marker positions of Figure 4, acquired by handheld FSI system; (b) spectrum of the quantum dots at same position, acquired by a commercial standard spectrometer (USB 4000, Ocean optics).

ent emission peaks placed under the surface of ex vivo porcine epithelium (Figure 4.9).

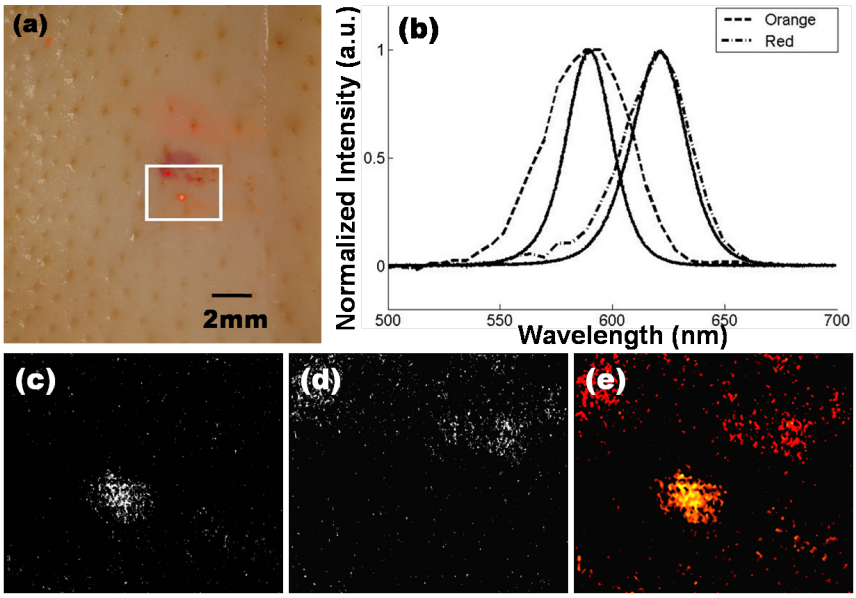


Figure 4.9: Biological Sample of porcine epithelium with QDs placed underneath the surface, with SD separation being zero (essentially, the confocal configuration). (a) Camera image of sample, MEMS HSI scan area is delineated by the white box. (b) Emission spectrum of quantum dots used. Bold curve derived using USB4000 spectrometer, broken line curves derived from the hyperspectral imaging system (25 points from 550-700nm). (c)-(d) De-mixed image acquired at the peak wavelength of orange and red QDs. (e) Pseudocolor image merged from (c), (d) after thresholding despeckling denoise.

The spectra of two QD implanted sites were measured. Image processing techniques including noise despeckling and contrast enhancing were used here to improve the image quality. Pseudo color images were acquired from hyperspectral images using the method of spectral unmixing. Using this method, we demonstrate our system's capability of optically distinguishing between fluorophores. This shows the potential of using bio-conjugating agents for hyperspectral fluorescence imaging towards biomarker detection.

## 4.7 Summary

Miniaturized portable optical diffuse reflectance HSI probe using the silicon MEMS micromirror has been developed for the purpose of skin cancer diagnosis. It is the first MEMS enabled hyperspectral micro-endoscope. Comparing with previous confocal reflectance microscope design, it integrates fluorescence imaging for enhanced contrast and specificity.

# Chapter 5

# Micromirror Innovations for Imaging Enhancements

In the circumstance of medical imaging, certain features including low-voltage restriction for patient safety, fabrication infrastructure demand and many others require a different fashion of miniature micromirror design. On the other hand, while batch fabrication of MEMS micromirror brings down the total cost of the handheld imaging instrument, the total cost of the system still large relies on the budget on optics and other opto-mechanical components. Besides, the handheld probe or the catheter's rigid length and its outer diameter are mainly limited by the focusing optics. To further reduce the size and cost of the handheld imaging systems, limit or replace the use of conventional optics provide one key to the solution.

To address the aforementioned concerns, this chapter introduces two insightful modifications on the current MEMS micromirror design on the device level that has been proposed and implemented. The first is to explore various material out of traditional silicon fabrication flow fitting the special use of electromagnetic MEMS device driving mechanism to meet the needs of medical imaging. This wide-scanning, low-voltage driven, gimbaled torsional stainless steel MEMS scanner is designed and then fabricated using electrical discharge machining (EDM). This technology offers unique advantages by allowing larger mirror surface areas (4 mm $\times$ 5 mm) to enhance the fluorescence collection efficiency at low incoming signal level and providing a rapid prototyping and low-cost alternative to silicon based MEMS devices, particularly when

large displacements and large field of view (FOV) are required. A maximum total optical scan angle (TOSA) of 20.6° at 112 Hz for a drive power of 200 mW is required for the slow-scan movement whereas the fast-scan movement occurs at the resonance frequency of 1268 Hz and has a TOSA of 26.6° using a drive power of 400 mW.

The second is a Fresnel zone plate monolithically integrated on the surface of the scanning micromirrors via patterning of optically reflective binary-phase modulation elements. The invention allows scanning and focusing functions to be integrated into the same device, thus obviating the need for multiple optical elements and eliminating cumbersome alignment. Both theoretical analysis and experimental results in this chapter prove its applicability to a handheld lensfree micro endoscope. We envision that this device can contribute to significant size reduction of the probe, thus enabling fast-scanning forward-imaging endoscopic devices.

## 5.1 Magnetic-actuated non-silicon MEMS micromirror

### 5.1.1 New MEMS micromirror design considerations

Actuators are important engines for Optical MEMS, we will introduce different kinds of actuation mechanisms first and explain the working principles in detail. Furthermore, for more specific applications, there are many variants or requirements based on these basic actuation mechanisms. Electrostatic MEMS devices work at different motion modes. Specifically, electrostatic MEMS devices with torsional rotation can be described as follows: when voltage is applied between the movable and the fixed electrodes, the moving part rotates about the torsion axis until the restoring torque and the electrostatic torque are equal. There are two major types of electrostatic actuators. The first is based on parallel-plate capacitance, and the other is based on comb-drive capaci-

tance. The vertical combdrive design, which we have utilized in our handheld confocal endoscope design, offers several advantages: (1) the structure and the actuator are decoupled; (2) the gap between the interdigitated fingers of the combdrive is typically quite small, on the order of a couple of microns. However, combdrive electrostatic micromirror at the same time is suffering from deficiencies such as requiring high voltage for actuation, therefore undesired for medical safety.

Thermal actuation utilizes the mismatch between thermal expansion coefficients of materials, which yields structural stress after temperature change. The structure deforms due to this built-in stress. The major advantage of thermal actuation is its ability to generate large deflection. Electrical current injection is one of the common mechanisms used for heating up the structure. However, temperature control and power consumption are issues for this type of actuators.

Meanwhile, magnetic actuation is practical when the structural dimensions are on the millimeter scale since the magnetic torque (generated by the magnetic device interacting with an external magnetic field) scales with volume for permanent magnetic materials and with total coil area for electromagnets. The overall system size must accommodate the magnets (permanent or electric coils) used to generate the external magnetic field. Therefore, the motivations for this type of scanner are usually cost reduction through batch fabrication and lower power consumption rather than miniaturization.

To design a low-cost, durable, and high-performance portable MEMS based TPM for real-time imaging, the micro-scanner needs to have the following desirable characteristics: (1) large optical scanning angle which translates into a larger FOV; (2) comparatively large mirror surface area and high-reflectance for better fluorescence light collection efficiency; (3) high fast-scan to slow-scan ratio to increase the image resolu-

tion; (4) smaller total system size and power consumption to ameliorate the portability of the microscope for in vivo use; (5) utilize low-cost and abundant structural material. Stainless steel is an alternative micro-scanner fabrication material to conventionally used silicon. This material offers various inherent advantages like simple actuation mechanisms with low actuation voltages, simple and low-cost fabrication processes, and preferable mechanical properties [84]. In this section, we introduce a 2D gimbaled stainless steel micro-scanner where both the mirror and the outer frame rotate about the fast and slow axes at their respective resonant frequencies to generate the Lissajous scanning pattern from the incoming laser beam for use in TPM.

### 5.1.2 Non-silicon MEMS micromirror design and fabrication

Figure 5.1 (a) and (b) depict the 2D torsional gimbaled micro-scanner structure and the magnetic actuation scheme, respectively. The design parameters are listed in Table 5.1. A small external permanent magnet creates a strong DC external field used to magnetize the ferromagnetic material (stainless steel material type 420) into its saturated state thus creating a fixed magnetization vector M that remains in-plane due to the micro-scanner's anisotropic design. The function generator that is controlled by the PC shown in Figure 5.1, provides a frequency dependent current input I($\omega$) to the driving electrocoil which creates an H-field to actuate the steel micro-scanner.

A torque component acts on the structure to minimize the overall energy in an actuator system by aligning the magnetization vector M with the field lines of the external magnetic field created by the driving electrocoil. Torque created in counter-clockwise direction can be calculated using the following equation [85, 86]:

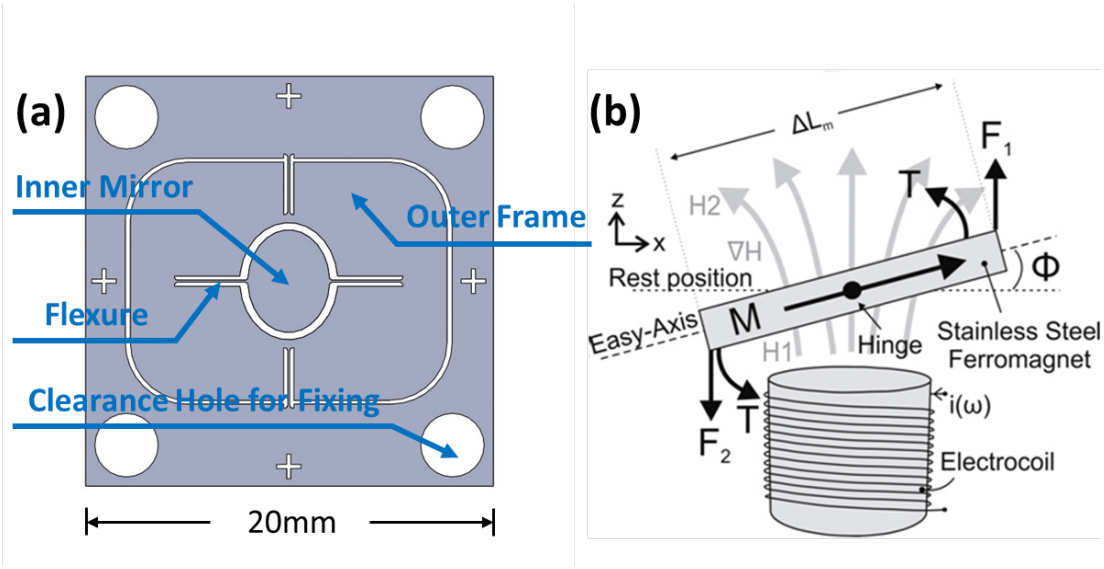


Figure 5.1: Scanner Design and Operations. (a) Computer aided design (CAD) for the stainless steel scanner. (b) Schematic representation of forces and torques under non-uniform H-field for the proposed steel scanner

$$T = MHV\cos\phi \tag{5.1}$$

where V is the volume of the magnetic material, M is the magnetization vector, H is the applied magnetic field, and $\phi$ is the easy-axis of the scanner and the scanners resting position normal to the surface of the electrocoil. When the frequency of the AC current driving the electrocoil matches the resonance peaks of the vibration modes of the micro-scanner, the displacement is enhanced by the mechanical quality factors of the respective motion.

Finite-element analysis (FEA) results of the designed micro-scanner are shown in Figure 5.2 for slow and fast scan axes, respectively. Outer frame generates an angular displacement about the slow-scan axis at the resonant frequency of 125.4 Hz corresponding to the refresh rate of the 2D Lissajous scanning whereas the inner mirror generates

Table 5.1: Stainless steel scanner design parameters

| Parameters | Devices |
|---|---|
| Length (mm) | 20 |
| Width (mm) | 20 |
| Thickness ($\mu$m) | 200 |
| Mirror Major Axis (mm) | 6 |
| Mirror Minor Axis (mm) | 4.8 |
| Mirror Surface Area ($mm^2$) | 22.62 |

a scan-line that is orthogonal to the slow-scan mode at approximately 1223.7 Hz.

Standard EDM process is used to fabricate the designed structure. After fabricating and defining the shape of the scanner, a 5 $\mu$m thick SU8 photoresist is spin coated onto the inner mirror in order to decrease the roughness of the steel surface. Following this, a 50 nm thick Ti is sputtered onto the SU8 mold as an adhesive layer. Then a 300 nm thick Al is sputtered onto the Ti layer to enhance the reflectivity of the inner mirror surface. A holder for the scanner is designed and fabricated using three dimensional (3D) printing technologies from acrylonitrile butadiene styrene (ABS) thermoplastic material as shown in Figure 5.3. The fabrication of the scanner system is finalized with the placement of the off-the-shelf electrocoil and the permanent magnet as shown in Figure 5.3 (b).

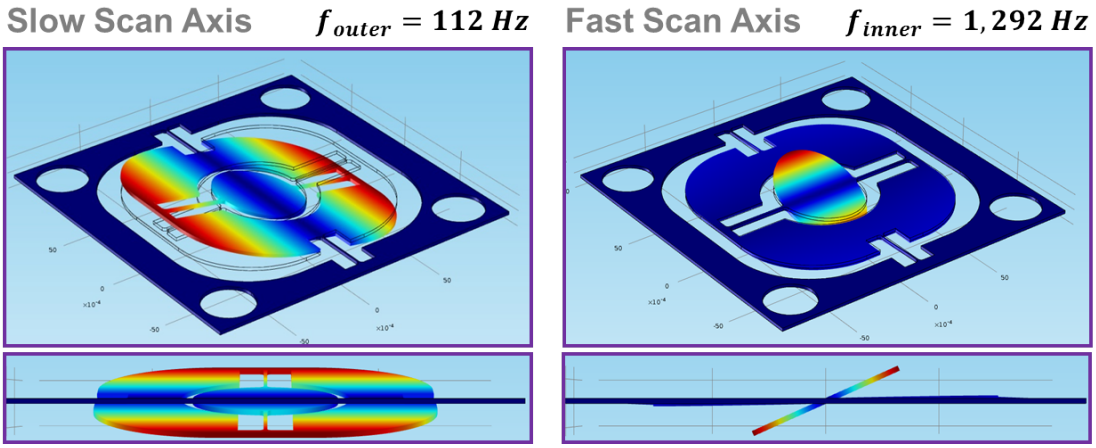


Figure 5.2: Finite-element analysis of the micro-scanner showing the torsional movement for both the slow and fast-scanning axis at 125.4 and 1223.7 Hz respectively.

### 5.1.3 MEMS micromirror experimental characterizations

Fabricated structure is shown in Figure 5.3 along with its ABS plastic holder. The steel scanner that is shown is 2 cm by 2 cm in length, with the inner mirror 5 mm in semi-major axis and 4 mm in semi-minor axis respectively. The plastic holder was designed to ensure the micro-scanner's mounted securely and to reduce the vibrational power loss, which could be delivered to the micro-scanner as scanning actuation power. Figure 5.3 (b) summarizes the entire scanning actuation system containing the electro-coil, plastic holder.

The peak displacements and corresponding resonance frequencies of the actuator for different drive levels are plotted in Figure 5.4 (a). As can be seen from this figure, there is a linear relationship between the drive voltage and the displacement, as expected as the drive level is increased, electrical spring softening effect is observed [87], which results in a small 2% downward shift in the resonance frequency. Figure 5.5 (b) exemplifies the acquired scan line at 112 Hz.

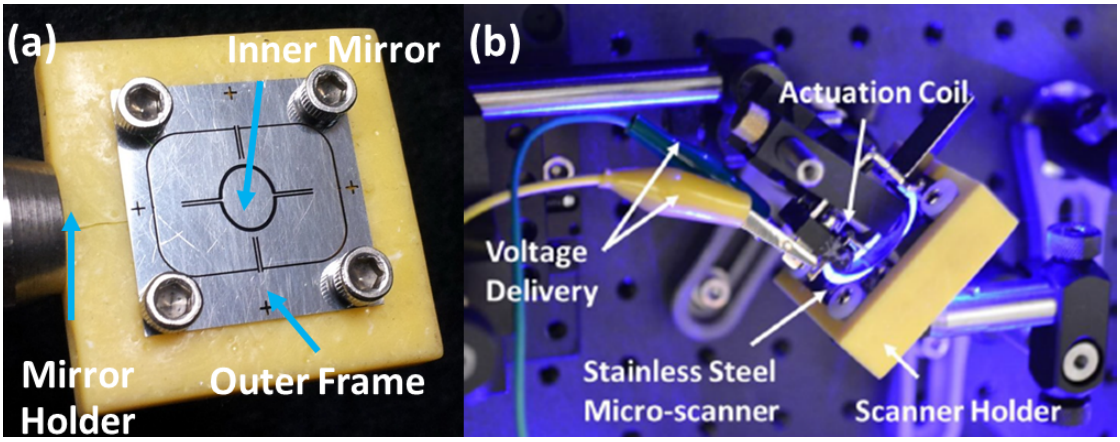


Figure 5.3: Micro-scanner and Device Assembly. (a) The fabricated 2 cm $\times$ 2 cm stainless steel scanner mounted on an ABS holder; (b) the actuation module together with the mounted stainless steel scanner in the bench-top TPM characterization system.

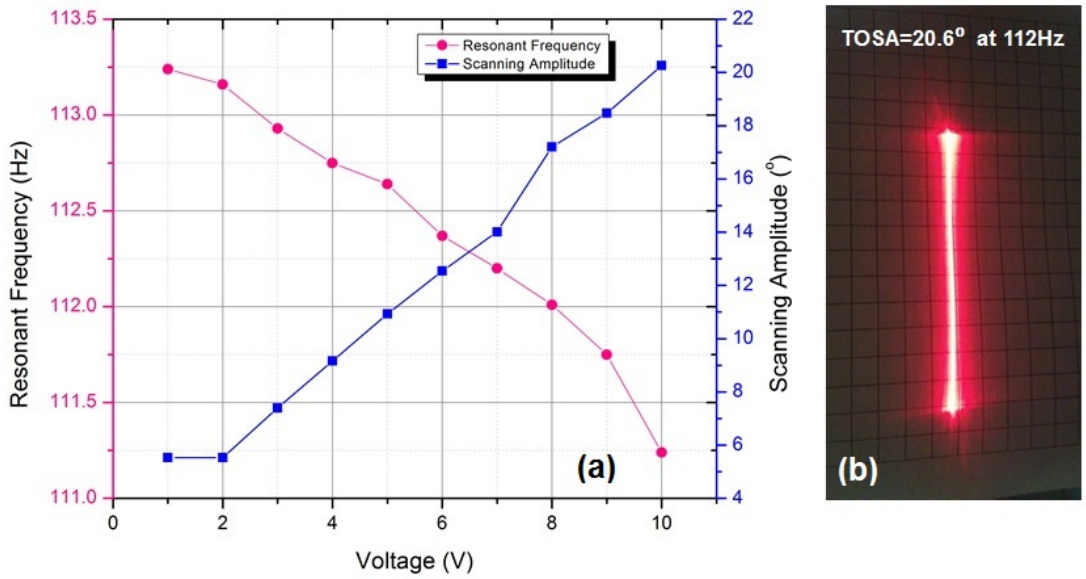


Figure 5.4: Characterization of the Micro-scanner. (a) Voltage dependence of the scanning amplitude and the resonant frequency of the steel scanner; (b) slow-scan line acquired at 112 Hz.

Figure 5.5 (a) and (b) plots the mechanical transfer characteristics of the tested device as a function of the operation frequency for slow and fast scan movements, respectively. The slow-scan operation takes place at 112 Hz whereas the fast-scan motion generates a scan line at 1268 Hz with a constant drive power of 200 mW.

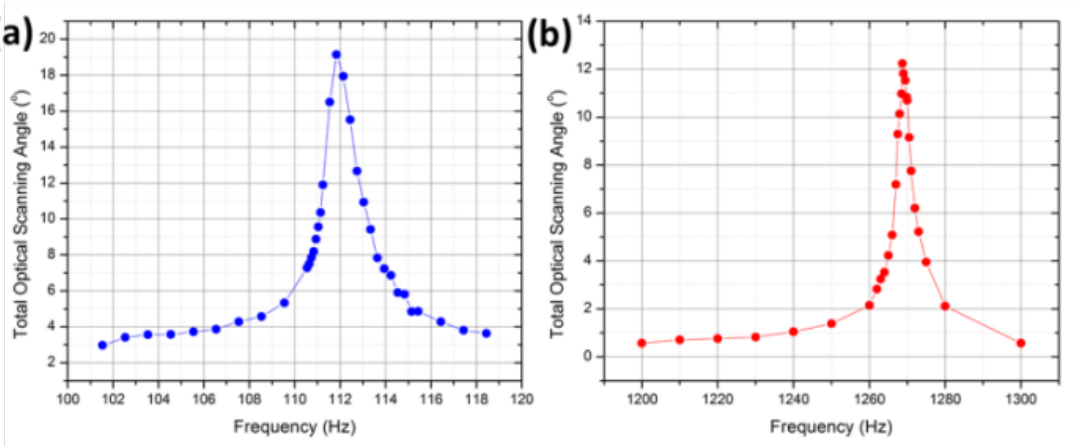


Figure 5.5: Total optical scanning angles of the gimbaled steel scanner versus drive frequency (a) outer frame (b) inner mirror.

## 5.2 Binary-phase Fresnel zone plate (FZP) objectives on 2-axis scanning micromirrors

Vertical combdrive micromirrors have been shown to provide the large rotational torque, deflection angles and mirror surface quality for laser-scanned imaging systems [88, 61, 89, 62, 49, 63, 64], while bringing down the cost of instruments by taking its advantage of mass production compatibility with semiconductor integrated circuit industry. However, the catheter rigid length and its outer diameter are mainly limited by the focusing optics. In other literatures, micro-machined 3-D optics has been assembled into integrated free-space systems [90], though catheter assembly becomes difficult and expensive in multi-element systems. In this section, we address this limitation by mono-

lithically integrating a micro-machined Fresnel zone plate objective on the surface of the micromirror via patterning of reflective binary phase modulation elements. Both theoretical analysis and experimental results proved its applicability to a handheld lens-free micro endoscope.

### 5.2.1 FZP theoretical background

Coherent illumination incident on the micromirror surface at an angle to the mirror normal can be concentrated at a wavelength-dependent focal distance by an elliptical zone plate (EZP, Figure 5.6) designed according to Eq. 5.2:

$$\left(\frac{x}{a_n \cos\theta}\right)^2 + \left(\frac{y-b_n}{a_n}\right)^2 = 1 \tag{5.2}$$

Where $a_n = \sqrt{n\lambda\left(f\cos^2\theta + \frac{n\lambda}{4}\right)} \Big/ \cos^2\theta$ and $b_n = n\lambda\sin\theta/2\cos^2\theta$.

In Figure 5.6, $\theta$ is the off-axis illumination angle, $\lambda$ is the illumination wavelength, and f is the focal distance, and an and $a_n cos(\theta)$ are the semi-major and semi-minor axes of the elliptical boundary of the $n^{th}$ zone of the EZP. Degradation in focal spot size due to changing illumination angle (by micromirror rotation) and illumination wavelength is negligible for optical path difference deviation of less than $\lambda/4$ from nominal value [91, 92]. Design boundaries to prevent aberrations are derived as:

Spherical Aberration:

$$n \approx \sqrt{2f/\lambda} \tag{5.3}$$

Chromatic Aberration:

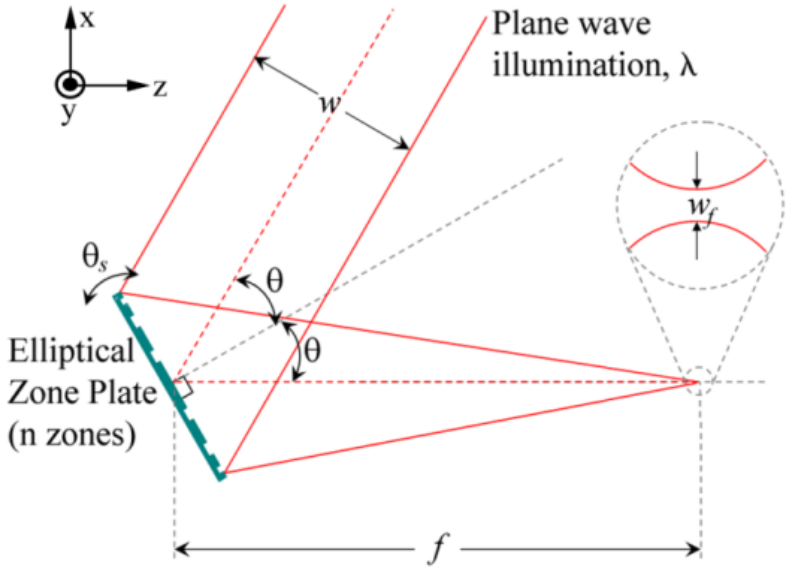


Figure 5.6: Illustration of design parameters for scanning binary-phase reflective Fresnel Zone Plate objectives. θ is the incident angle of the off-axis plane illumination of wavelength, w and $w_f$ are the incident and focused beam waists, f is the focal distance, and $\theta_s$ is the scan angle of the elliptical zone plate having n zones.

$$n \approx \lambda/\Delta\lambda \tag{5.4}$$

Off-Axis Aberration:

$$\alpha \approx (3n)^{-1/2} \qquad (for\ small\ n) \tag{5.5}$$

These conditions determine number of EZP zones and scanning angle, therefore number of resolvable points in the image. Variation in focal distance with wavelength may be utilized for axial scanning in 3D imaging systems [93].

As depicted in Figure 5.7, optical field diffraction of the Fresnel EZP propagates from reference plane ζ =0 in the (ξ, η, ζ) coordinate system, which is the Fresnel EZP surface plane, to reference plane z=0 in the (x, y, z) coordinate system, which

is the imaging plane shown in Figure 5.7. To verify optical performance, commercial software like CODE V or ZEMAX typically use approaches include ray-tracing which is valid only in the geometrical optics approximation to the light propagation. In our case, diffraction must be precisely taken into account, starting from the scalar diffraction theory to propagate the optical fields. There are some other commercial software like PARAXIA and GLAD handling scalar diffraction theory by using the Fresnel and the Fraunhofer approximations or direct integration. However, when dealing with light propagation between titled planes as in our case, all the existing software could only resort to direct numerical integration rather than adopting the Fast Fourier Transform (FFT) for calculation, while direct numerical integration could be extremely time-consuming comparing with FFT, especially when the computational window size is large. Direct numerical integration does not work effectively for our EZP imaging, since the aperture size is comparatively too large as a two-dimensional integration computation window considering the imaging wavelength is only 635nm. Conditions for the Fresnel and the Fraunhofer approximations do not hold either in our case, therefore requiring a specially developed FFT based scalar diffraction integrated program compatible with tilts to calculate the optical performance for our Fresnel FZP imaging.

Conditions for the Fraunhofer approximation and the Fresnel approximation are illustrated in Eq. 5.7 and Eq. 5.7 respectively:

$$z_0 \gg \frac{k(\xi^2+\eta^2)}{2} \tag{5.6}$$

$$z_0 \gg \sqrt[3]{\frac{\pi}{4\lambda}[(x-\xi)^2+(y-\eta)^2]^2_{max}} \tag{5.7}$$

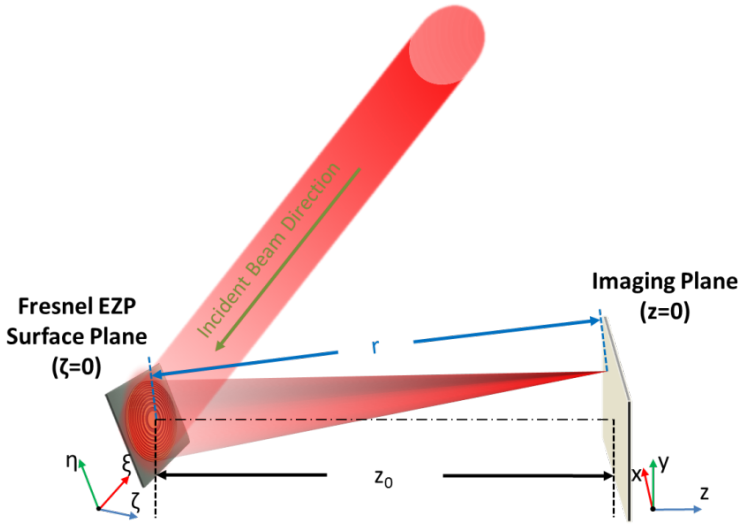


Figure 5.7: Coordinate systems involved in the Fresnel EZP diffraction integral analysis. r is the light path length from the Fresnel EZP surface plane to the imaging plane, $z_0$ is the distance between the micromirror center of the Fresnel EZP to the imaging plane in its orthogonal direction (z direction). The imaging plane is placed at a distance which is the EZP's focal length along z-direction ($z_0 = f$).

in Eq. 5.7 and 5.7, $k = 2\pi/\lambda$, $\lambda$ is the imaging wavelength. In our case, the distance between the imaging plane and the micromirror is designed to be the same as the micromirror's focal length, which is 7mm ($z_0$=f), the field size on the imaging plane is set to be the same as the size of the micromirror, which is 1mm by 1mm, and the imaging wavelength $\lambda$ is 635nm. So in our case the valid range of the Fraunhofer approximation and the Fresnel approximation are $z_0 \gg$ 9.89m and $z_0 \gg$ 42.9mm, while $z_0$ is truly 7mm. Therefore, conditions for Fresnel approximation illustrated in Eq. 5.7 and Fraunhofer approximation illustrated in Eq. 5.7 do not meet in our occasion.

The most accurate methods for scalar treatment is the Rayleigh-Sommerfeld diffraction integral [94], the only approximation would be the ignoring of the vectorial nature of light. To understand the optical performance of the EZP model defined by Eq. **??**, a Rayleigh-Sommerfeld integral numeric simulation was carried out. Further,

Fast Fourier Transform (FFT) based numerical simulation in Matlab has been used to replace traditional numerical integration for efficient computation.

Eq. 5.8 indicates the full form Rayleigh – Sommerfeld integral equation according to the coordinate system illustrated in Figure 5.7:

$$U(x,y,z) = -\frac{1}{2\pi}\iint_{A} U(\xi,\eta,0)\times\frac{\partial}{\partial\zeta}\left(\frac{e^{-ikr}}{r}\right)dxdy \tag{5.8}$$

Where $r=\sqrt{z^2+(x-\xi)^2+(y-\eta)^2}$, therefore Eq. 5.8 can be seen as a convolution of two parts as indicated in Eq. 5.9:

$$U(x,y,z) = F^{-1}\{F\{U(x,y,z)\}\} = F^{-1}\left(F\{U(\xi,\eta,0)\}\times F\left\{\frac{1}{2\pi}\frac{\partial}{\partial\zeta}\left(\frac{e^{-ikr}}{r}\right)\right\}\right) \tag{5.9}$$

Where:

$$F\{U(\xi,\eta,0)\} = A_0(\nu_x,\nu_y,0) = \iint_{A} U(\xi,\eta,0)\times\exp\left[-2i\pi\left(\nu_x x+\nu_y y\right)\right]d\xi d\eta \tag{5.10}$$

Considering the case when the diffraction propagates between two tilted planes, the focusing spots under different MEMS mirror deflection angles may deviate away from the origin point on the observation plane. To shift the focusing spot back to the center of the FFT computational window and evaluate such deviation and its impact on focusing spot size for imaging, we applied transformation matrix and origin offset adjustment in coordinate system for the FFT algorithm [95]. The simulated focusing spot profile under different deflection angles with off-axis illumination angles of 20°

are depicted in Figure 5.8, in which the focused Airy disk remains the center of the observation area, and little degradation of focusing profile has been observed when the scanning angle of the MEMS EZP increases The focusing spot size were obtained by calculating the area size of positions where the normalized intensity is over the 1/e of the maximum intensity as shown in Figure 5.8 (a)-(c), and then derive the equivalent diameter based on the area size.

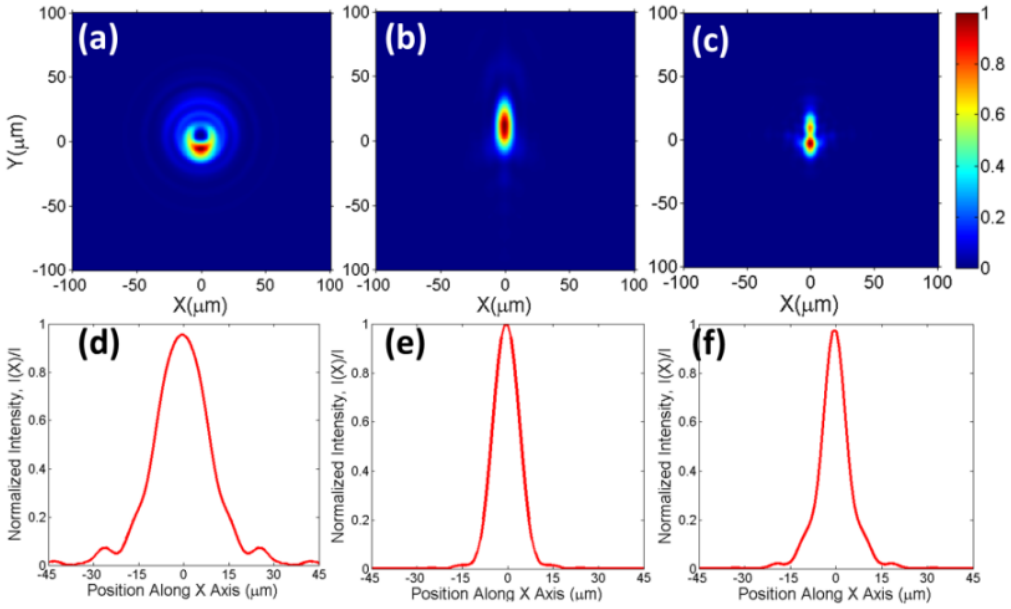


Figure 5.8: (a)-(c): Diffraction focusing spot 2-D profiles on the observation plane while the MEMS EZP tilts along y axis with different angles of (a) 0° (b)5° and (c) 10°. (d)-(f): Intensity distribution plot along X axis passing through the maximum intensity position. The tilts angles along y axis used in (d)-(f) are the same to those in (a)-(c) respectively. The incident laser beam has a 20° offset with the EZP plane.

To evaluate the focusing spot size on the full field of imaging plane, the full width half maximum (FWHM) of the simulated focusing spot profiles under different tilting angles were calculated. Figure 5.9 shows the resolution map with reference to different EZP X and Y axes rotational angles up to 12° by 12°, indicating the focusing capability varies from 10.5 $\mu$m to 28.6 $\mu$m when EZP scans the full field.

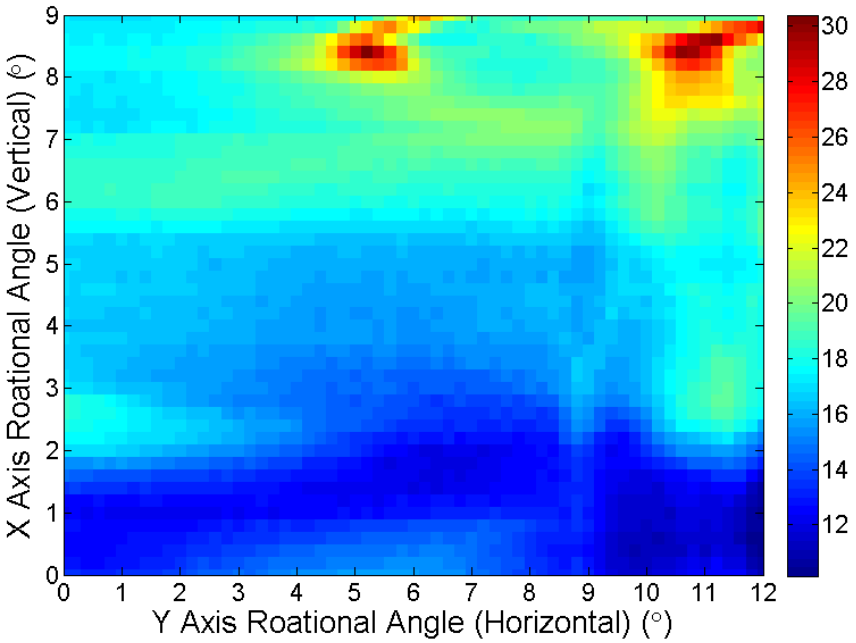


Figure 5.9: Simulated focusing spot resolution map for the full imaging field of Fresnel EZP on the observation plane, scale bar is in microns.

### 5.2.2 Device fabrication

The micromirror is actuated by staggered vertical comb drives fabricated by a comb self-alignment process in bonded double-SOI wafers [96, 97]. Coarse features of the stator are etched by Deep Reactive Ion Etching (DRIE) into 25 $\mu$m thick SOI $< 100 >$ device layer. An oxidized $< 100 >$ wafer is fusion bonded on top of the patterned wafer, and ground down to 25 $\mu$m thickness with ¡50nm surface roughness to form the micromirror surface. Features of the elliptical zone plate objectives are patterned on the surface to quarter-wavelength depth. Exact features of the actuators, aligned to the lower layer features, are etched into deposited silicon dioxide. DRIE-oxide RIE-DRIE etching sequence forms the self-aligned. Backside substrate DRIE and oxide RIE on both sides releases the mirror and removes remaining protective oxide. Scanning electron micrographs of the fabricated device are presented in Figure 5.10.

### 5.2.3 Device characterization

The measured focused spot size shows little degradation Figure 5.11 for micromirror scanning angles up to $10^{\circ}$ (optical) about both axes. When comparing with the simulation results predicted in Figure 5.9, the measured esults shows a similar resolution range, while the spot size 2-D distribution is different in certain areas. The simulated resolution map has the minimum and maximum values of 10.5 $\mu$m and 28.6 $\mu$m, while the measured resolution ranges from 12 to 24 $\mu$m. The small difference may come from fabrication defects and measurement errors. In simulated resolution map, the worst resolution happens when both the horizontal and vertical axes reach the maximum deflection angles. The reason for this could be longer diffraction distance for the laser beam to propagate from the micromirror to the imaging plane when the deflection

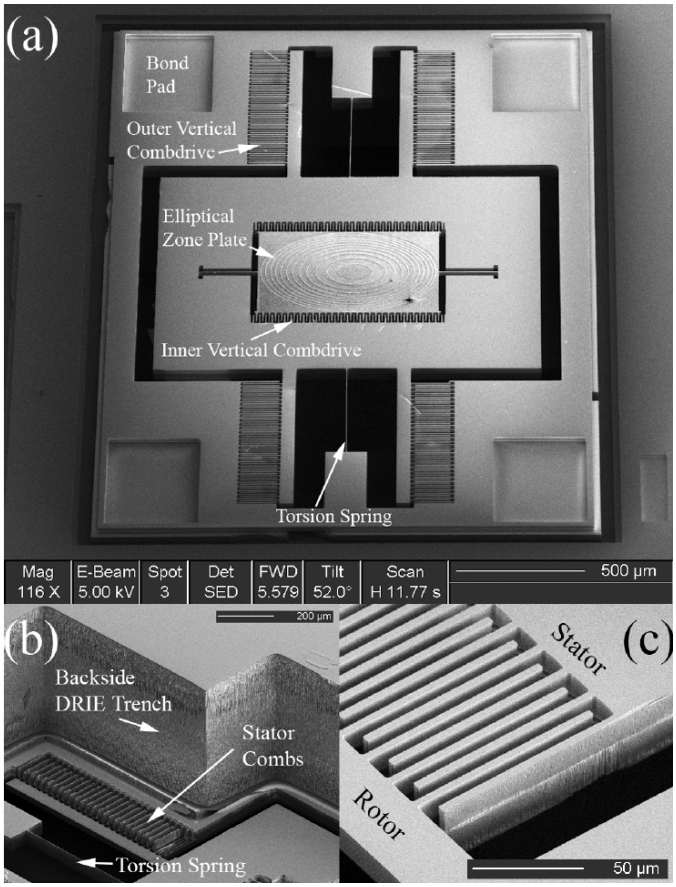


Figure 5.10: SEM images of the fabricated device. (a) Top view showing the EZP, vertical comb drives, torsion springs, and bond pads for electrical connection. (b) Backside view showing DRIE trench with vertical sidewalls to release the scanning micromirror. (c) Close-in view of vertical combdrive.

angles are larger, therefore deviating from the value of the focal length designed for Fresnel EZP. However in measurement, worst resolution happens when there is largest horizontal axis deflection with a small vertical deflection.

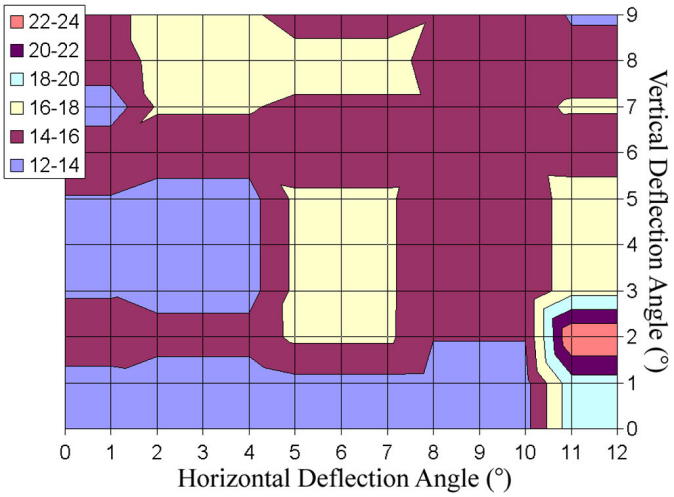


Figure 5.11: Map of diameter of the focused spot (in microns) created by an EZP with 7mm focal length for 635nm illumination at 20° nominal incidence as function of optical angular deflection of the micromirror.

Preliminary testing of image-formation capabilities of the device was performed in a simple transmission-mode experiment. A sample with spatially-varying transmission was placed in the focal plane of a scanning EZP, and transmitted light was concentrated into a photo-detector using two collection lenses. Mylar transparencies printed with longhorn logos and numbers were imaged (Figure 5.12) using the system at 5 frames/second. Comparison with images obtained from an Olympus BX51 microscope using 10X objective indicated an estimated field of view of 1mm $\times$ 0.35mm at approximately 15 $\mu$m resolution.

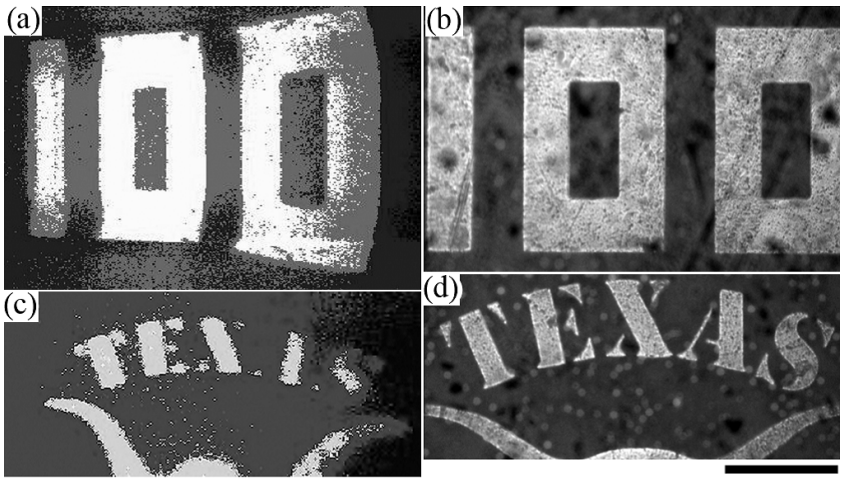


Figure 5.12: Results of imaging Mylar transparencies using preliminary transmission-mode imaging experiment. (a-b) Image calibration: (a) Image of number 100 (transparent) in opaque background, and (b) Image of sample using Olympus BX51 confocal microscope. (c-d) Image of longhorn symbol and text "TEXAS": (c) using the device, and (d) using Olympus BX51 confocal microscope. Scale Bar: 250 $\mu$m.

## 5.3 Summary

To reduce the scanning driving voltage requirements and explore new materials for MEMS micromirror fabrication, a novel stainless steel micro-scanner with large mirror surface area and easy fabrication profile was designed, fabricated and incorporated in a hyperspectral fluorescence TPM system. The stainless steel micromirror requires a driving voltage lower than 10V while providing large scanning amplitude ($> 20°$). Large imaging field of view was thus required by the stainless steel micromirror based microscope with an imaging rate of 10 FPS.

Novel monolithic integration of reflective binary-phase modulation elements on two-axis MEMS scanning micromirrors is demonstrated for simultaneous beam scanning and focusing in a compact single-chip solution. Focusing capability varying from 10.5 $\mu$m to 28.6 $\mu$m with reference to different EZP deflection angles were predicted

by a FFT based Rayleigh-Sommerfeld scalar integral simulation, and afterwards experimentally determined to be around 15 $\mu$m. This approach can potentially eliminate the need for focusing optics in a micro-endoscopes catheter, thus simplifying assembly and improving form factor.

# Chapter 6

# Non-Silicon MEMS enabled Hyperspectral Two-Photon Autofluorescence Imaging for Epithelial Cancer Detection

This chapter reviews a handheld hyperspectral two-photon imaging system capable of acquiring spectral imaging across wide spectrum simultaneously towards applications in early epithelial cancer diagnosis. Utilizing the non-silicon MEMS scanner, this is the third-generation handheld imaging probe designed for cancer diagnosis. Inheriting the advantages of high imaging contrast, enhanced signal to noise ratio, broadband spectroscopic analysis and portability of previous designs, this two-photon hyperspectral autofluorescence imaging gains its unique desired features compared to its predecessors by integrating non-silicon MEMS scanner and two-photon autofluorescence imaging within it. Those features include low-voltage actuation, enhanced fluorescence collection efficiency and better hyperspectral signatures for cancer diagnosis.

As discussed in the background chapter, hyperspectral imaging, which integrates the advantages of both conventional imaging and spectroscopy, were first designed for remote sensing [98], while currently finding diverse applications in biomedical imaging field. Portable hyperspectral screening devices are highly desirable for sensitive biopsy-free characterization of diseases such as epithelial cancers in situ and precision guided microsurgery. Spectral resolution and frame rate in such miniaturized imaging devices are in high demand, which has led to intensive research on developing novel

handheld multi-channel imaging and spectroscopy instruments using microtechnologies [65]. Traditional hyperspectral imaging techniques involve the using of liquid crystal and acousto-optic tunable filters, Fourier-transform spectrometry or spectral-temporal scanning to acquire both morphological and spectral information, while capturing both spatial and spectral data within one frame is highly preferred to reduce processing time. However, the imaging rate is limited by the switching rate, while there is also trade-off between the spectral image quality and the acquisition time. Currently most advanced hyperspectral imaging microscope on market could acquire hyperspectral imaging at 5 frames per second (fps) with 512 $\times$ 512 pixel resolution [99], but with a bulky size and a costly price. Here we explore a miniaturized, portable and low-cost solution for hyperspectral imaging.

Compared to the various microscopy techniques employed in these systems, two-photon laser scanning microscope (TPLSM) has shown great promise as a versatile non-invasive fluorescence imaging tool over the last two decades [100, 38]. TPLSM improves on conventional confocal fluorescence microscopy by using a near infrared (NIR) femtosecond laser pulses excite fluorophores through the simultaneous absorption of two photons within 10-15 fs [101, 102]. While broadly applied in various cancer diagnosis applications [41, 40], research work is currently focused on the miniaturization of TPM for use in minimally invasive handheld imaging systems. A portable two-photon imaging probe used to view suspected tumor sites noninvasively could replace costly and painful biopsy procedures. Therefore this system could improve treatment, reduce processing cost, and lessen interpretation inaccuracy in remote areas that lack adequate clinical centers and healthcare facilities [103]. Various types of miniaturized laser scanning TPM schemes have been developed, including scanning cantilever mechanisms utilizing fiber tips [104, 105], small lens [106] and a microelectromechanical (MEMS)

scanning micromirror [107, 108, 109, 110]. This chapter will start with a non-silicon TPLSM design, and then followed by the evaluation and characterization of it.

## 6.1 Two-photon hyperspectral autofluorescence imaging background

Two-photon microscopy allows high-resolution imaging of in vivo intact tissues. Two-photon absorption (2PA) excited fluorescence has an important advantage over conventional one-photon absorption excited fluorescence due to its inherent 3D resolution, larger penetration depth, lower scattering, and lower photodamage. Intrinsic contrast from nicotinamide adenine dinucleotide (NADH), flavin adenine dinucleotide (FAD), collagen, elastin, and keratin [111, 112] can allow measurement of metabolism and native structure without the need to introduce artificial compounds. Reliable imaging of intrinsic contrast on microscopic-length scales in tissues such as the heart, brain, skin, and tumors could provide important insights into cellular function and allow improved interpretation and validation of diagnostics based on in vivo bulk-tissue measurements. Precancers are characterized by epithelial changes including increased nuclear size, increase nuclear-to-cytoplasmic ratio, hyperchromasia, pleomorphism, angiogenesis, and increased metabolic rate [113]. Epithelial invasion of underlying structures marks the transition to full-blown malignancy. The neoplastic process is associated with changes in the extracellular matrix (ECM), especially the collagen fibers and the framework that they constitute.

Collagen appears to be the tissue constituent mainly responsible for second harmonic generation (SHG) [114, 115]. Endogenous SHG in biological materials arises from the large molecular anisotropy and second-order nonlinear susceptibility typical of biological molecules and structures [41]. Collagen molecules consist of three pep-

tide chains that form a rod-shaped triple helix. Nonlinear susceptibility is an optical property characteristic of chiral molecules. The microcrystalline structure of collagen [116, 117, 118, 119] makes it capable of SHG [115, 120]. Several researchers have reported endogenous second harmonic generation in biological tissues. Fine and Hansen [114] used a ruby laser to irradiate a variety of excised tissues. SHG was observed only in collagenous tissues (cornea, sclera, tendon, and skin). The dependence of the SHG signal on tissue structure and local symmetry has been used for macroscopic mapping [120, 116]. SHG was observed in type I collagen by nanosecond laser irradiation over a broad spectral region [116].

Using a hyperspectral two photon data acquisition and spectral unmixing technique we can delineate and quantify the concentrations of multiple intrinsic fluorophores and sources of second-harmonic generation in vivo. Spectral data can be used to segment distinct structures within 3D volumes, based on the specific excitation–emission fingerprints of each structure's constituents. Hyperspectral microscopy can allow extraction of the relative concentrations of specific intrinsic fluorophores, effectively yielding in vivo, spatially resolved chemical analysis of fine submicrometer structure. In this chapter we mainly investigate the hyperspectral imaging of collagen phantom sample as the starting point.

## 6.2 MEMS enabled two-photon hyperspectral imaging instrumentation

Following the similar development path of the laser scanning confocal reflectance endoscope, a desktop two photon laser scanning microscope (TPLSM) was first developed and verified with typical calibration two-photon excited fluorophores.

The imaging process in TPLSM begins with the delivery of an ultrafast infrared laser pulse train to the optical scanning device which steers the laser light onto the imaging sample through various well-aligned optical imaging components. Typically, a visible-infrared dichroic mirror is placed at the intersection of illumination and detection arms to allow only visible fluorescence signal to pass through and be detected by an opto-electro convertor. Figure 6.1 depicts a real-time hyperspectral fluorescence based TPM which uses a magnetically actuated stainless steel micro-scanner as the light steering unit and a Ti-sapphire femtosecond laser (80 MHz Mai Tai, Spectra Physics) as the light source. The illumination Ti-sapphire laser was selected to be centered at 800nm, which is capable of exciting various fluorophores such as DAPI, fluorescein isothiocyanate (FITC), yellow fluorescent protein (YFP) and Alexa 568 [121, 122]. Although these fluorophores have different one-photon excitation (OPE) spectrums, due to different quantum mechanical selection rules, a fluorophore's two-photon excitation (TPE) spectrum is usually not equivalent to the double wavelengths of its OPE spectrum, allowing for the TPE spectrum for various fluorophore's to overlap. As shown in Figure 6.1, the illumination beam coming from the Ti-sapphire laser is reflected by a dichroic mirror with 775nm cutting-off wavelength (FF775, Semrock, Inc.) , then deflected by the stainless steel micro-scanner, and is focused onto the sample with the help of an objective lenses with various magnification levels. The forwarding illumination laser power is controlled at 50mW before passing through the dichroic mirror. The power controlling was realized by placing by a thin film femtosecond laser line polarizer (420-0126, Eksma Optics) on the imaging path mounted on a rotational stage. The polarizer can be rotated to approach the matching laser light polarization to decrease the optical power.

A custom made software kit was developed in Java and LabVIEW for paral-

lel driving signal generation, data acquisition, real-time image construction, and post processing for hyperspectral imaging. The software kit I/O port generates a low voltage signal to modulate the flux generated by an electrocoil to actuate both axes of the micro-scanner at the device's resonant frequencies and create a Lissajous scanning pattern on the tissue sample. The TPE fluorescence light is guided back by the scanner and reflected by the dichroic mirror before striking a volume phase holographic (VPH) grating. The dispersed light is detected by a 16-channel linear photomultiplier (PMT) array (H11459, Hamamatsu Photonics) where the spectral information is acquired and analyzed by our custom developed software kit to generate the hyperspectral images at 10 frames per second (FPS).

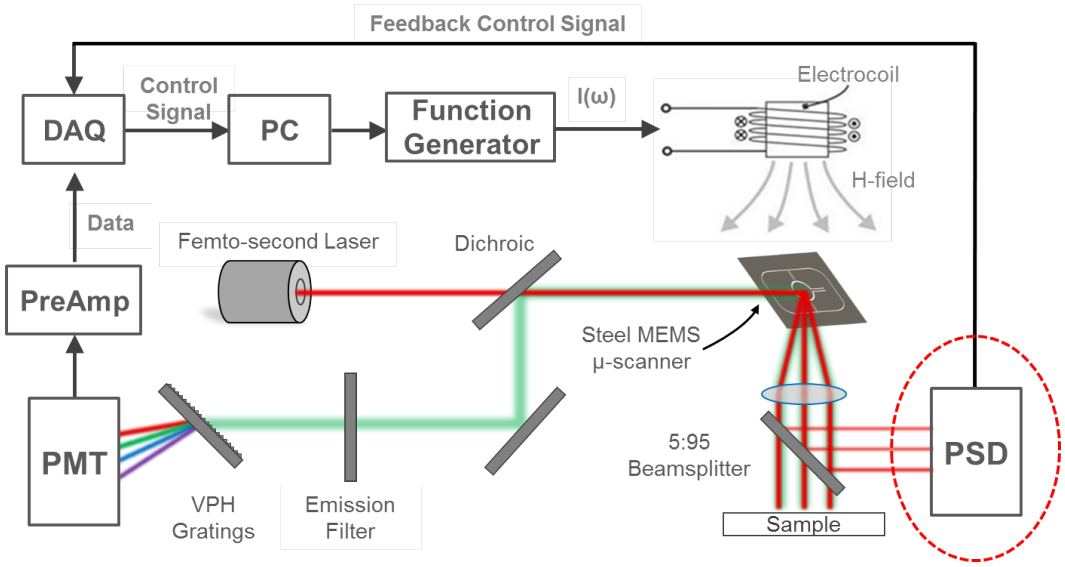


Figure 6.1: Schematic of two-photon fluorescence microscope based on the magnetic-actuated micro-scanner.

To create a closed-loop feedback control system, a position sensitive device (PSD, S5990-01, Hamamatsu Photonics) was incorporated into the forward illumination path in order to determine location of micro-scanner in real time which allows the system

to compensate for damping effects and improve image stability. For torsional scanners, the energy loss due to nonlinear viscous forces, i.e. air damping, and material fatigue creates an unstable relationship between the applied torque and deflection angle. Also, stochastic perturbations, such as vibration, driving electronics jitter, thermal changes, and shock, can introduce mechanical misalignment into the mirror position [123]. This feedback control system compensates for disturbances or imperfections in the micro-scanner which may cause the FOV to fluctuate to reduce image blurring. Without a feedback system, the end user would need to estimate the amplitude, frequency, offset, and phase of the Lissajous pattern in order to construct an image. The new system incorporating the PSD automates and simplifies the image construction operation.

A portion of the forward illumination light is directed to the PSD by a 5:95 beamsplitter which placed between the micro-scanner and the objective lens. The PSD will generate two sinusoidal patterns which depict the relative X and Y position of the micro-scanner and help analyze the nonlinear behavior of the torsion suspensions and the oscillatory stability.

For data acquisition, the signal collected by the 16 channel PMT was recorded by a 16 analog input channel data acquisition (DAQ) card (National Instruments PXIe-6358) and the two input channel DAQ card (National Instruments PCI-6111) was used record the PSD signal. To help remove unwanted environmental noise from the PSD signal, a simple band pass circuit was implemented before data acquisition. A continuous digital pulse train triggering signal, with a frequency equal to acquisition rate, was routed to the programmable free interface (PFI) channel of both DAQ cards in order to synchronize the outgoing micro-scanner actuation signal and the incoming 16 channel florescence data and the PMT signal which represents the fluorescence data nonlinearly

spaced across the visible spectrum.

The synchronized fluorescence and PSD data is sent from LabVIEW to a Java based program via TCP/IP. The PSD signal is passed through a digital filter in order to remove frequencies irrelevant to micro-scanner actuation. An autocorrelation algorithm is used to determine the phase delay between the known actuation signal and the filtered PSD signal. The correct phase delay allows the Java program to plot the intensity values along the phase-corrected Lissajous scanning pattern to create an output window displaying all 16 images.

## 6.3 MEMS enabled hyperspectral imaging probe design

A handheld probe for two-photon hyperspectral imaging was develop as shown in Figure 6.2. The main differences of this generation of hyperspectral imaging probe comparing with the previous diffusion optical imaging probe include: 1). Compatible with half inch off-shelf lens tubes, therefore possible for multiple imaging lens tube compatibility. 2). The incorporation of a non-silicon MEMS scanner, ideal for medical imaging use due to its low-voltage actuation. 3). Femtosecond laser beam delivery through a photonic crystal fiber (LMA-20, Thorlabs).

In the embodiment designed for oral cancer detection, the optical layout and performance were designed and predicted as shown in Figure 6.3. Large FOV reaching 1mm by 1mm with the lateral optical resolution of 0.99$\mu$m was realized at the excitation wavelength of 800nm.

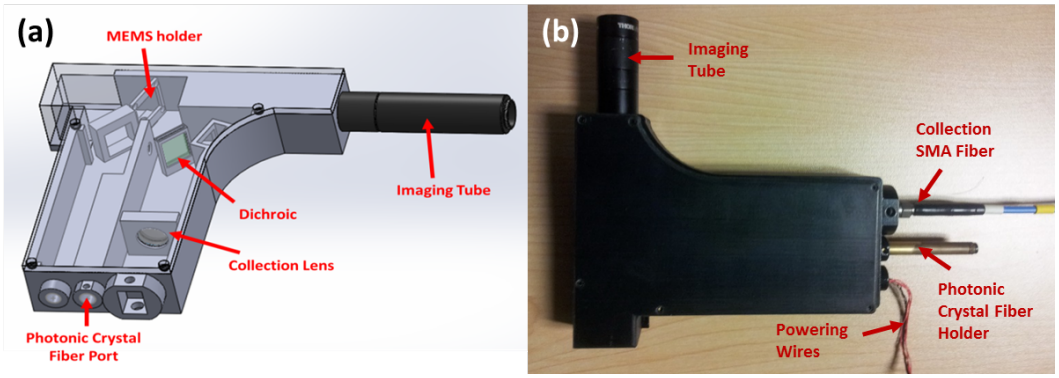


Figure 6.2: Handheld two-photon hyperspectral imaging probe design. (a) CAD schematic of the handheld two-photon hyperspectral imaging probe. (b) Photograph of the assembled handheld two-photon hyperspectral imaging probe.

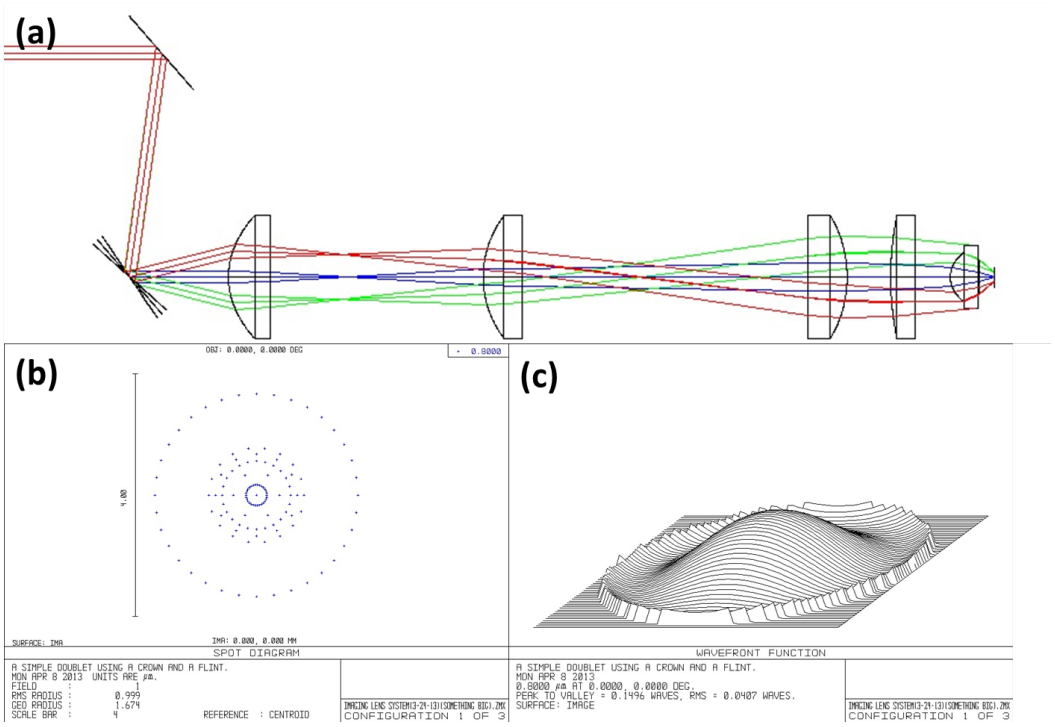


Figure 6.3: Optical design layout and imaging performance simulation of handheld two-photon imaging probe for oral cancer detection. (a) Handheld two-photon imaging probe lens tube layout design. (b) Lateral optical resolution simulation. (c) Wavefront performance simulation.

## 6.4 Two-photon autofluorescence phantom sample preparation

We prepared the rat tail collagen 1 to synthesize 5mg/ml collagen hydrogels as phantom sample for the calibration of two-photon autofluorescenec imaging. The preparation process for the two-photon autofluorescence collagen phantom sample is as follows (Figure 6.4) [124]:

* Diluted in acetic acid/
* DMEM+HEPES buffer
* $<$ 0.5mm thick
* 37 °C for 50 minutes
* Stored in 1 $\times$ DPBS at 38 °C

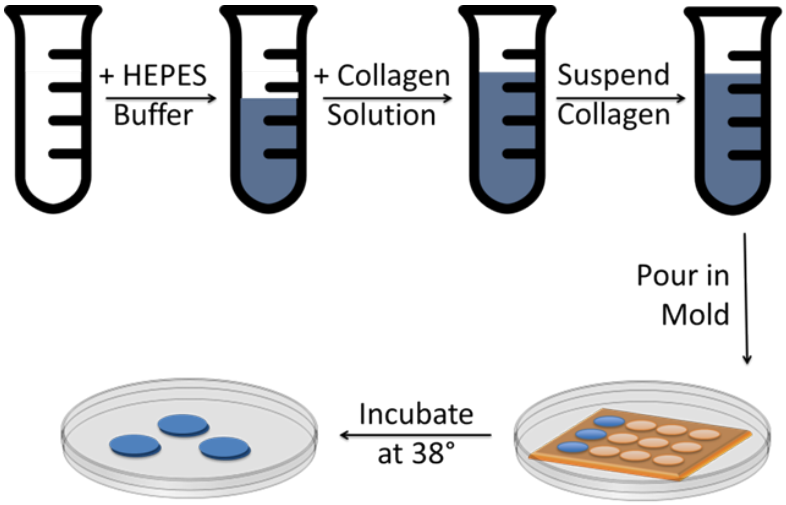


Figure 6.4: Schematic of two-photon fluorescence microscope based on the magnetic-actuated micro-scanner.

## 6.5 Two-photon hyperspectral imaging results

The hyperspectral fluorescence imaging performance of the micro-scanner based TPM is demonstrated by imaging of spike stained CTCs and the MSCs attached on micro beads in a PEGylated fibrin gel. During cancer metastasis, CTCs are shed from the primary malignant melanoma site into the surrounding vasculature which the cells may seed additional tumor sites and dramatically worsen the patient's cancer prognosis. Thus CTCs are widely recognized as indicators of the patient's cancer disease status [125]. However, CTCs are usually rare and are extremely difficult to detect. Numerous CTC screening methodologies have been explored and some distinguish themselves as novel miniaturized point-of-care approaches [126], but nearly all require a painful and time-consuming isolation, enrichment and characterization process. Carrying the advantages of high selectivity, small size, and low photo-toxicity, MEMS based TPM integrated with CTC microfluidic devices shows promise and may prove itself as the next groundbreaking point-of-care CTC screening technique, echoing recent endeavors on optofluidic cell analysis [127]. MEMS enabled portable hyperspectral TPM would create a much more efficient CTC detection system due to the device's inherent speed and compact size allowing it to be incorporated into a point-of-care device. The device's accuracy would only be dependent on the selectivity of two-photon fluorescence imaging, which is enhanced and facilitated by various extrinsic fluorophores staining techniques. Here, the fluorescence imaging TPM using the MEMS micromirror of has FOV of 200 $\mu$m $\times$ 400 $\mu$m and lateral resolution of 1 $\mu$m with a water-immersion multiphoton objective lens (CFI Fluor 60XW, N.A. = 1, Nikon Corp.), with an imaging rate of 10 FPS. Figure 6.5 was acquired from the 540 nm wavelength window of the hyperspectral fluorescence imaging of cultured cancer cell line of COLO 205 after the

screening experiment. The preliminary characterization results illustrated here from the spike CTCs depicts the great potential of a fast hyperspectral screening imaging system as a new diagnostic tool for fast CTCs calibration after screening.

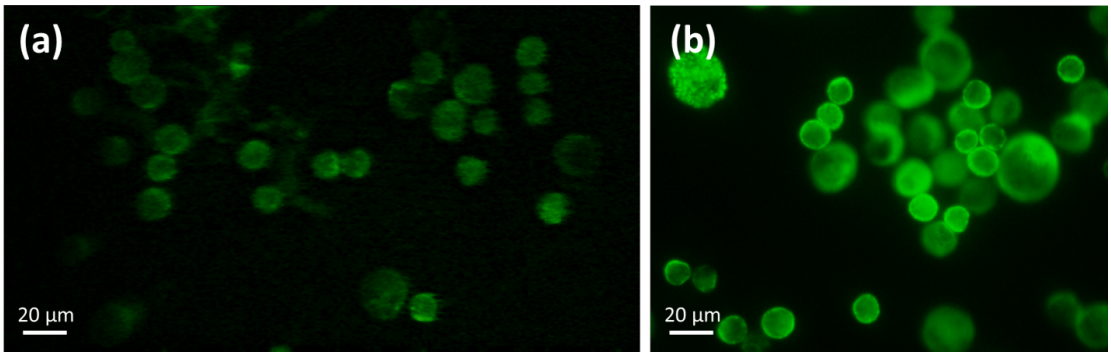


Figure 6.5: (a).The stainless steel MEMS micromirror based TPM imaging calibration using COLO 205 cancer cell line after CTCs screening with a microfluidic device. Scale bar is 30 $\mu$m. (b). Control image from Olympus BX51 desktop fluorescent microscope for comparison.

Three 3D physiological and morphological analyses are essential in verifying the cellular phenotype in tissue engineering [128]. MEMS enabled TPM provides a portable and convenient solution for the tissue 3D physiological and morphological fluorescence characterization. Figure 6.6 demonstrates the hyperspectral depth-sectional characterization of the physiological and morphological features of the MSCs attached on a MCB in a PEGylated fibrin gel. As the characterization tissue model, the human mesenchymal stem cells are attached to the MCB array. 2D hyperspectral images of 16 wavelengths were imaged by the MEMS enabled TPM at depths at 0 $\mu$m to 206 $\mu$m from the top of the MCB, with the depth sequence gap of 1 $\mu$m.Figure 6.6 (a) provides the orthogonal view of the MSCs attached on MCB, while Figure 6.6 (b-e) provide the cross-sectional view of the sample at multiple depths. All the figures of Figure 6.6 are the composite of the images acquired from the 480 nm and 540 nm wavelength windows of the hy-

perspectral fluorescence MEMS TPM. The blue components notate the DAPI stained cell nuclei area, while the green components notate the Calcein AM stained whole cell plasma area.

The microcarrier bead assays with human MSCs were used in the angiogenesis assays in a fibrin-based in vitro model. While morphological characterization is critical to determine whether desired cell types were achieved for tissue engineering, the successful morphometric measurements and quantification of the assay demonstrates the validity of using MEMS TPM to fulfill this requirement. Moreover, with the power of large imaging range, high resolution, low photo-toxicity and small form factor, MEMS TPM is ideal, if not essential, to real-time monitor the process of tissue-development on site.

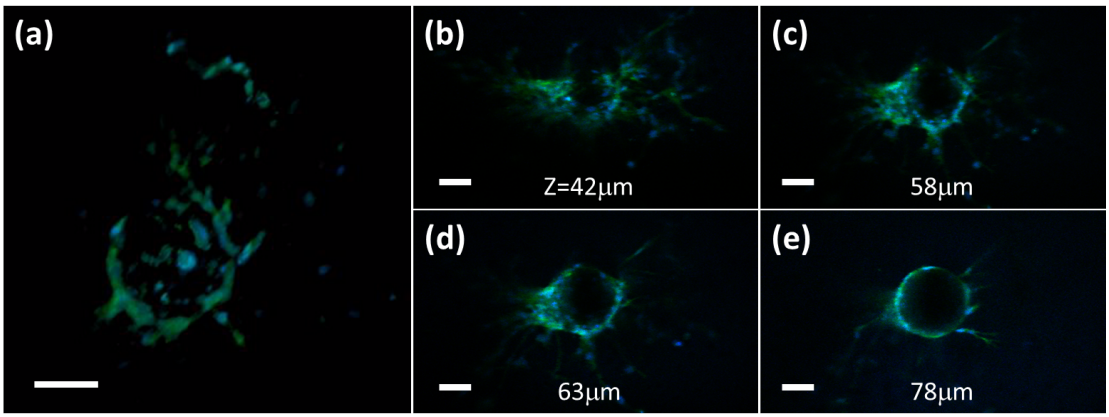


Figure 6.6: MEMS TPM images acquired from and the MSCs attached on a MCB in a PEGylated fibrin gel. (a) Three-dimensional rendering of a sequence of 207 lateral MEMS TPM images of the MSCs. Sequence depth gap is 1 $\mu$m. (b-e) Selection of lateral images from an imaging depth of 42, 58, 63 and 78 $\mu$m. Field of view in all lateral images is 0.6mm $\times$ 1mm. Scale bars are 100 $\mu$m.

The two-photon autofluorescence imaging of collagen fiber phantom sample is as shown in Figure 6.7.

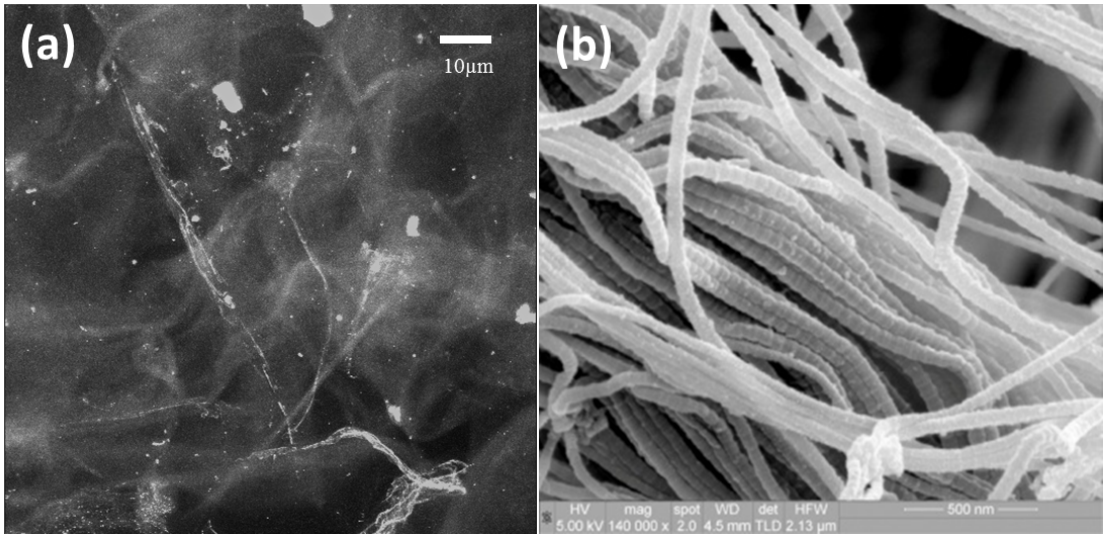


Figure 6.7: Two-photon autofluorescence imaging of collagen fiber phantom sample. (a) Two-photon imaging result. (b) Control imaging of collagen sample under SEM

## 6.6 Summary

Miniaturized portable TPM probe using the stainless steel MEMS micromirror have been shown to be a possible and valid approach from the optical imaging performance characterization of the MEMS enabled TPM. Various biological tissue samples, including spike CTCs and MSCs attached to MCB with extinct fluorophores were used for the characterization and evaluation for the imaging performance of MEMS enabled hyperspectral probes.

# Chapter 7

# Conclusion and future directions

This dissertation experimentally demonstrates multiple imaging modalities designed for multiple applications of cancer imaging in early diagnosis and precise tumor margin assessment in cases of excisional therapy. Health care professionals encounter multiple dilemmas with the surveillance, diagnosis, and management of patients with oral neoplasia. Driven by the needs toward a complete and advanced mobile and *in situ* imaging and surgery guidance tool, we coupled our expertises in miniature confocal optical imaging, optical diffuse reflectance imaging, nonlinear optical imaging, hyperspectral imaging and optical MEMS devices toward this end. Engineering of precision optical micro- and nano- systems has enabled complex next-generation healthcare instruments providing reduced form factor and enhanced minimally-invasive visualization of internal organs at levels of resolution and informative detail. Such miniaturized instruments can prove to be the driving force to make new discoveries and solve a myriad of healthcare-related problems of critical importance to the general public. This dissertation demonstrates the applicability of MEMS scanner enabled multi-modality endoscopic instruments for *in vivo* diagnostics and potential extension of image-guided excisional microsurgery towards early cancer detection, treatment, and monitoring.

A complete investigation of desktop and handheld confocal reflectance microscope using the silicon electrostatic combdrive micromirror was first implemented. The MEMS confocal laser endomicroscopy (CLE) built was based upon the principle of

illuminating a tissue with a low-power laser and then detecting reflectance or fluorescent light reflected from the tissue. The laser is focused at a specific depth and only light reflected back from that plane is refocused and able to pass through the pinhole confocal aperture. This handheld confocal imaging system is capable of resolving sub-cellular morphological features of single cell layer optical sections, of thickness similar to conventional histology, located up to several hundred micrometers deep. The optical performance was predicted during design stage using Code V showing the sub-cellular level lateral and axial resolution, which got verified and proved with experimental outcomes.

Our core imaging instrumentation innovation was coupled with homemade highly specialized software kit to provide easy and fully functional use for the anatomic pathologists without engineering background. These histological images of tissue with details provided gives the possibility of defining the cellular signatures of disease states in real-time. Fast Lissajous imaging speed up to 2 fps was realized with improved Labview and Java based real-time imaging software. Properties such as 3D imaging through auto-focusing and mosaic imaging for extended lateral view were examined for carcinoma real-time pathology. With the aid of this state-of-the-art imaging tool, we performed the first and only practice in Texas to use MEMS enabled confocal endomicroscopy to make a precise aid in the diagnosis of oral cavity with dysplasia or localized cancer at the UT Health Science Center San Antonio (UTHSCSA). Ex vivo and ex vitro tissue samples including the Neoplastic lesion tissues of Giant Cell Fibroma and Peripheral Ossifying Fibroma, the fibroma inside the paraffin box and gross tissues block from patients were imaged by the bench-top and handheld imaging modalities, and further compared with commercial microscope imaging results. We show that the efficacy of the MEMS scanner based handheld confocal imaging probe as a potential clinical tool for oral cancer

diagnosis and treatment.

As laser scanning handheld confocal endoscope proved to be an effective imaging tool for early cancer diagnosis with highly improved mobility, reduced cost and enhanced efficiency, we continue to seek the breakthroughs overcoming the limitations for better quality and highly informative images for cancer diagnosis. A skin cancer diagnosis probe integrating optical diffuse reflectance imaging and hyperspectral imaging was developed. Over the past two decades, one of the wide-ranging research activities taken place using alternative techniques to traditional biopsy on the early detection of cancer was Hyperspectral imaging (HSI), which represents a hybrid modality for optical diagnostics due to spectroscopic data being obtained from an image. The HSI concept combines spectroscopy and imaging and allows the recording of the entire emission spectrum for every pixel on the entire image. For materials such as individual minerals or cellular materials, it is possible to construct a spectral curve from the hyperspectral data that can then be matched with the spectral signatures of individual materials collected from the laboratory or identified earlier and available in data banks or spectral libraries. Specific reflectance peaks and absorption troughs can be read directly from these curves to allow for the precise identification of a material, class, cell, or feature. On the other hand, due to the well-defined source-collector geometry of optical probes, it is possible to draw quantitative conclusions from the spectral images and attain optical and physiological property maps. Models that the optical spectra are fit to can be analytical models such as, diffusion theory, computational models such as Monte-Carlo, or empirical models such as the look-up-table. Broadband diffuse optical spectroscopy imaging system that acquires a widefield spectral cube of image data (x,y, $\lambda$) with spectra at each pixel processed for the estimation of multiple optical and biological properties could be used to form into respective property maps for cancer analysis. The acqui-

sition of spectral and spatial information multiplies the diagnostic strengths of dermal inspection.

MEMS micromirror has been the core enabling technology for the manipulation of light by micromechanical actuation, in integration with other micro-optical elements. While obtaining the advantages of small form factor, large scanning angle, compatibility with semiconductor industry, the first generation silicon micromirror suffers from the drawbacks of limited aperture size, and requirement for high voltage actuation, which result in low fluorescence collection efficiency in hyperspectral imaging, and medical safety concerns, respectively. Aiming at optimal fluorescence imaging performance in two-photon imaging mode and to reduce the fabrication time and cost, a novel non-silicon (stainless steel) MEMS scanner based on electrical discharge machining (EDM) technique was developed.

Autofluorescence hyperspectral imaging is emerging as a desired point-of-care solution for cancer diagnosis without the need for extrinsic fluorophores conjugated with *in vivo* tissues. Integrating the stainless steel scanner, a handheld two-photon hyperspectral imaging probe was developed, taking the advantages of two-photon excitation such as longer-penetration depth, pinbole-less design, and low phototoxicity for various types of cancer diagnosis.

Meanwhile, techniques such as real-time mosaic imaging and laser-scanning status monitoring were developed to ensure the imaging reliability for handheld imaging. These efforts contribute to a more informative and reliable handheld imaging instrument for oral cancer detection.

Stepping forward from my dissertation research, endeavors could be followed either on device or instrumentation level, both serving the increasing point-of-care early

cancer diagnosis need toward a more informative and multi-functional engineering tool.

Though MEMS micromirror has demonstrated great advantages in single point laser scanning imaging system, there are emerging optical units such as Yokogawa spinning disc for the realization of laser scanning imaging instruments, serving with parallel collection, much faster imaging rate, and moving-part-less features. There is a need to follow the improving microscopy technologies , while combining the strength of MEMS industry, to develop of next-generation laser-manipulation micro-device for imaging handheld instrumentations. On the other hand, desired functionalities to be incorporated such as focus adjustment and lensless design could be achieved through a multi-functional device integrating reflective micromirror with additional imaging capabilities.

Besides, on the instrumentation level, while most of the previous efforts has been focused on the miniaturization of the front-end probe, the size of the serving platform is also desired to be reduced, echoing the development of mobile health as the leading theme for point-of-care devices. A lower cost imaging instrument with lower requirement for the light source and photodetector unit, while preserving powerful features such as 3D profiling and hyperspectral imaging, is on call for the next-stage development.

As an engineering tool designed for the healthcare need, early cancer diagnosis instrumentations should be timely feedbacked with the latest requirements from the clinic, no matter in which direction of innovation. Convinced with the care specialty needed in hospitals as springboard for key drive, the continuing research and development efforts will be focused on the following directions: 1) Adapt the core imaging technologies to fulfill physicians' needs in other fields of medicine, such as imaging guided suspicious tissue removal and computer aided disease real-time diagnosis. 2)

Exploring the adaptation of the imaging technology to therapeutic technologies. 3) Collaborate with research in other specialized areas such as neurology, head and neck, and gynecology, to build clinical data and accelerate the translational research.

# Bibliography


[1] World Health Organization. Department of Reproductive Health, World Health Organization. Department of Chronic Diseases, and Health Promotion. *Comprehensive cervical cancer control: a guide to essential practice*. WHO, 2006.

[2] Siddhartha Mukherjee. *The emperor of all maladies: a biography of cancer*. Scribner, 2011.

[3] Ruth Etzioni, Nicole Urban, Scott Ramsey, Martin McIntosh, Stephen Schwartz, Brian Reid, Jerald Radich, Garnet Anderson, and Leland Hartwell. The case for early detection. *Nature Reviews Cancer*, 3(4):243–252, 2003.

[4] Janet E Joy, Edward E Penhoet, Diana B Petitti, et al. *Saving women's lives: strategies for improving breast cancer detection and diagnosis*. National Academies Press, 2005.

[5] Robert G McKinnell, Ralph E Parchment, Alan O Perantoni, and G Barry Pierce. *The biological basis of cancer*. Cambridge University Press, 1998.

[6] Andrew J Einstein. Medical imaging: the radiation issue. *Nature Reviews Cardiology*, 6(6):436–438, 2009.

[7] Boris Rainer Haxel, Martin Goetz, Ralf Kiesslich, and Jan Gosepath. Confocal endomicroscopy: a novel application for imaging of oral and oropharyngeal mucosa in human. *European Archives of Oto-Rhino-Laryngology*, 267(3):443–448, 2010.

[8] Arthur F Gmitro and David Aziz. Confocal microscopy through a fiber-optic imaging bundle. *Optics letters*, 18(8):565–567, 1993.

[9] SA Boppart, Brett E Bouma, Constantinos Pitris, Guillermo J Tearney, James G Fujimoto, and ME Brezinski. Forward-imaging instruments for optical coherence tomography. *Optics Letters*, 22(21):1618–1620, 1997.

[10] Sunghoon Kwon and Luke P Lee. Micromachined transmissive scanning confocal microscope. *Optics letters*, 29(7):706–708, 2004.

[11] Youngjoo Yee, Jong U Bu, Manhyo Ha, Junghoon Choi, Hyunho Oh, Sangshin Lee, and Hyojin Nam. Fabrication and characterization of a pzt actuated micromirror with two-axis rotational motion for free space optics. In *Micro Electro Mechanical Systems, 2001. MEMS 2001. The 14th IEEE International Conference on*, pages 317–320. IEEE, 2001.

[12] Ankur Jain, Hongwei Qu, Shane Todd, and Huikai Xie. A thermal bimorph micromirror with large bi-directional and vertical actuation. *Sensors and Actuators A: Physical*, 122(1):9–15, 2005.

[13] Hyoung J Cho and Chong H Ahn. Magnetically-driven bi-directional optical microscanner. *Journal of Micromechanics and Microengineering*, 13(3):383, 2003.

[14] Jack W Judy and Richard S Muller. Magnetic microactuation of torsional polysilicon structures. *Sensors and Actuators A: Physical*, 53(1):392–397, 1996.

[15] Arda D Yalcinkaya, Hakan Urey, Dean Brown, Tom Montague, and Randy Sprague. Two-axis electromagnetic microscanner for high resolution displays. *Microelectromechanical Systems, Journal of*, 15(4):786–794, 2006.

[16] Hyuck Choo, David Garmire, James Demmel, and Richard S Muller. Simple fabrication process for self-aligned, high-performance microscanners—demonstrated use to generate a 2-d ablation pattern. *Microelectromechanical Systems, Journal of*, 16(2):260–268, 2007.

[17] Dooyoung Hah, ST-Y Huang, Jui-Che Tsai, Hiroshi Toshiyoshi, and Ming C Wu. Low-voltage, large-scan angle mems analog micromirror arrays with hidden vertical comb-drive actuators. *Microelectromechanical Systems, Journal of*, 13(2):279–289, 2004.

[18] Lixia Zhou, Joseph M Kahn, and Kristofer SJ Pister. Scanning micromirrors fabricated by an soi/soi wafer-bonding process. *Microelectromechanical Systems, Journal of*, 15(1):24–32, 2006.

[19] Kurt E Petersen. Silicon torsional scanning mirror. *IBM Journal of Research and Development*, 24(5):631–637, 1980.

[20] Ming C Wu. Micromachining for optical and optoelectronic systems. *Proceedings of the IEEE*, 85(11):1833–1856, 1997.

[21] Richard S Muller and Kam Y Lau. Surface-micromachined microoptical elements and systems. *Proceedings of the IEEE*, 86(8):1705–1720, 1998.

[22] Kurt E Petersen. Silicon as a mechanical material. *Proceedings of the IEEE*, 70(5):420–457, 1982.

[23] Dooyoung Hah, Hiroshi Toshiyoshi, and Ming C Wu. Design of electrostatic actuators for moems applications. In *Symposium on Design, Test, Integration, and Packaging of MEMS/MOEMS 2002*, pages 200–207. International Society for Optics and Photonics, 2002.

[24] Dae Sung Lee. *Design and fabrication of SOI-based micromirrors for optical applications*, volume 68. 2007.

[25] Robert A Conant, Jocelyn T Nee, Kam Y Lau, and Richard S Muller. A flat high-frequency scanning micromirror. In *Proc. Solid-State Sensor and Actuator Workshop*, pages 6–9, 2000.

[26] Dooyoung Hah, Chang-Auck Choi, Chang-Kyu Kim, and Chi-Hoon Jun. A self-aligned vertical comb-drive actuator on an soi wafer for a 2d scanning micromirror. *Journal of Micromechanics and Microengineering*, 14(8):1148, 2004.

[27] Karthik Kumar, Kazunori Hoshino, and Xiaojing Zhang. Handheld subcellular-resolution single-fiber confocal microscope using high-reflectivity two-axis vertical combdrive silicon microscanner. *Biomedical microdevices*, 10(5):653–660, 2008.

[28] Sunghoon Kwon, Veljko Milanovic, and Luke P Lee. Vertical combdrive based 2-d gimbaled micromirrors with large static rotation by backside island isolation. *Selected Topics in Quantum Electronics, IEEE Journal of*, 10(3):498–504, 2004.

[29] C Tsou, WT Lin, CC Fan, and Bruce CS Chou. A novel self-aligned vertical electrostatic combdrives actuator for scanning micromirrors. *Journal of Micromechanics and Microengineering*, 15(4):855, 2005.

[30] Marvin Minsky. Microscopy apparatus, December 19 1961. US Patent 3,013,467.

[31] A Fine, WB Amos, RM Durbin, and PA McNaughton. Confocal microscopy: applications in neurobiology. *Trends in neurosciences*, 11(8):346–351, 1988.

[32] W Stolz, C Schmoeckel, F Ryckmanns, J Gross, and O Braun-Falco. Morphometric and ultrastructural analyses of melanocytes, nevus cells, and melanoma cells. *Archives of dermatological research*, 279(3):167–172, 1987.

[33] Xin Wang, Brian W Pogue, Shudong Jiang, Hamid Dehghani, Xiaomei Song, Subhadra Srinivasan, Ben A Brooksby, Keith D Paulsen, Christine Kogel, Steven P Poplack, et al. Image reconstruction of effective mie scattering parameters of breast tissue in vivo with near-infrared tomography. *Journal of biomedical optics*, 11(4):041106–041106, 2006.

[34] Cliff Wong, Triantafyllos Stylianopoulos, Jian Cui, John Martin, Vikash P Chauhan, Wen Jiang, Zoran Popović, Rakesh K Jain, Moungi G Bawendi, and Dai Fukumura. Multistage nanoparticle delivery system for deep penetration into tumor tissue. *Proceedings of the National Academy of Sciences*, 108(6):2426–2431, 2011.

[35] Patrick Theer, Mazahir T Hasan, and Winfried Denk. Two-photon imaging to a depth of 1000 $\mu$m in living brains by use of a ti: Al¡ sub¿ 2¡/sub¿ o¡ sub¿ 3¡/sub¿ regenerative amplifier. *Optics letters*, 28(12):1022–1024, 2003.

[36] Patrick Theer and Winfried Denk. On the fundamental imaging-depth limit in two-photon microscopy. *JOSA A*, 23(12):3139–3149, 2006.

[37] Gary Chinga-Carrasco Magnus B. Lilledahl and Catharina de Lange Davies. *Confocal Laser Microscopy - Principles and Applications in Medicine, Biology, and the Food Sciences*. InTECH, 2013.

[38] Warren R Zipfel, Rebecca M Williams, and Watt W Webb. Nonlinear magic: multiphoton microscopy in the biosciences. *Nature biotechnology*, 21(11):1369–1377, 2003.

[39] Virginijus Barzda, Catherine Greenhalgh, Jürg Aus der Au, Steven Elmore, Johannes van Beek, and Jeff Squier. Visualization of mitochondria in cardiomyocytes by simultaneous harmonic generation and fluorescence microscopy. *Optics express*, 13(20):8263–8276, 2005.

[40] Melissa C Skala, Jayne M Squirrell, Kristin M Vrotsos, Jens C Eickhoff, Annette Gendron-Fitzpatrick, Kevin W Eliceiri, and Nirmala Ramanujam. Multiphoton microscopy of endogenous fluorescence differentiates normal, precancerous, and cancerous squamous epithelial tissues. *Cancer research*, 65(4):1180–1186, 2005.

[41] Petra Wilder-Smith, Kathryn Osann, Nevine Hanna, Naglaa El Abbadi, Matt Brenner, Diana Messadi, and Tatiana Krasieva. In vivo multiphoton fluorescence imaging: a novel approach to oral malignancy. *Lasers in surgery and medicine*, 35(2):96–103, 2004.

[42] Enrico Dimitrow, Mirjana Ziemer, Martin Johannes Koehler, Johannes Norgauer, Karsten König, Peter Elsner, and Martin Kaatz. Sensitivity and specificity of multiphoton laser tomography for in vivo and ex vivo diagnosis of malignant melanoma. *Journal of Investigative Dermatology*, 129(7):1752–1758, 2009.

[43] Nicholas J Durr, Timothy Larson, Danielle K Smith, Brian A Korgel, Konstantin Sokolov, and Adela Ben-Yakar. Two-photon luminescence imaging of cancer cells using molecularly targeted gold nanorods. *Nano letters*, 7(4):941–945, 2007.

[44] Christoph Stosiek, Olga Garaschuk, Knut Holthoff, and Arthur Konnerth. In vivo two-photon calcium imaging of neuronal networks. *Proceedings of the National Academy of Sciences*, 100(12):7319–7324, 2003.

[45] Edward B Brown, Robert B Campbell, Yoshikazu Tsuzuki, Lei Xu, Peter Carmeliet, Dai Fukumura, and Rakesh K Jain. In vivo measurement of gene expression, angiogenesis and physiological function in tumors using multiphoton laser scanning microscopy. *Nature medicine*, 7(7):864–868, 2001.

[46] Michael J Levene, Daniel A Dombeck, Karl A Kasischke, Raymond P Molloy, and Watt W Webb. In vivo multiphoton microscopy of deep brain tissue. *Journal of neurophysiology*, 91(4):1908–1912, 2004.

[47] Yuval Garini, Ian T Young, and George McNamara. Spectral imaging: principles and applications. *Cytometry Part A*, 69(8):735–747, 2006.

[48] Fred A Kruse. Mapping spectral variability of geologic targets using airborne visible/infrared imaging spectrometer (aviris) data and a combined spectral feature/unmixing approach. In *SPIE's 1995 Symposium on OE/Aerospace Sensing and Dual Use Photonics*, pages 213–224. International Society for Optics and Photonics, 1995.

[49] K Kumar and XJ Zhang. Cmos-compatible 2-axis self-aligned vertical comb-driven micromirror for large field-of-view microendoscopes. In *Micro Electro Mechanical Systems, 2009. MEMS 2009. IEEE 22nd International Conference on*, pages 1015–1018. IEEE, 2009.

[50] Karthik Kumar, Rony Avritscher, David C Madoff, and Xiaojing Zhang. Handheld single-cell-layer optical sectioning reflectance confocal microscope for interventional imaging. In *The 29th Conference on Lasers and Electro Optics (CLEO)*, 2009.

[51] Karthik Kumar, Jonathan C Condit, Austin McElroy, Nate J Kemp, Kazunori Hoshino, Thomas E Milner, and Xiaojing Zhang. Fast 3d in vivo swept-source optical coherence tomography using a two-axis mems scanning micromirror. *Journal of Optics A: Pure and Applied Optics*, 10(4):044013, 2008.

[52] Ahmedin Jemal, Rebecca Siegel, Jiaquan Xu, and Elizabeth Ward. Cancer statistics, 2010. *CA: a cancer journal for clinicians*, 60(5):277–300, 2010.

[53] Katayoun Sargeran, Heikki Murtomaa, Seyed Mohammad Reza Safavi, Miira M Vehkalahti, and Olli Teronen. Survival after diagnosis of cancer of the oral cavity. *British Journal of Oral and Maxillofacial Surgery*, 46(3):187–191, 2008.

[54] Balakrishna B Yeole, Agnihotram V Ramanakumar, and R Sankaranarayanan. Survival from oral cancer in mumbai (bombay), india. *Cancer Causes & Control*, 14(10):945–952, 2003.

[55] Imjai Chitapanarux, Vicharn Lorvidhaya, Pichit Sittitrai, Thienchai Pattarasakulchai, Ekkasit Tharavichitkul, Pornpoch Sriuthaisiriwong, Pimkhuan Kamnerdsupaphon, and Vimol Sukthomya. Oral cavity cancers at a young age: analysis of patient, tumor and treatment characteristics in chiang mai university hospital. *Oral oncology*, 42(1):82–87, 2006.

[56] Gerry F Funk, Lucy Hynds Karnell, Robert A Robinson, Weining K Zhen, Douglas K Trask, and Henry T Hoffman. Presentation, treatment, and outcome of oral cavity cancer: a national cancer data base report. *Head & neck*, 24(2):165–180, 2002.

[57] A Chandu, G Adams, and ACH Smith. Factors affecting survival in patients with oral cancer: an australian perspective. *International journal of oral and maxillofacial surgery*, 34(5):514–520, 2005.

[58] Sol Silverman. *Oral cancer*. Pmph Bc Decker, 2003.

[59] Lewis R Eversole. *Clinical outline of oral pathology: diagnosis and treatment*. Pmph-usa, 2001.

[60] Shinya Inoué. Foundations of confocal scanned imaging in light microscopy. In *Handbook of biological confocal microscopy*, pages 1–19. Springer, 2006.

[61] Karthik Kumar, Rony Avritscher, Youmin Wang, Nancy Lane, David C Madoff, Tse-Kuan Yu, Jonathan W Uhr, and Xiaojing Zhang. Handheld histology-equivalent sectioning laser-scanning confocal optical microscope for interventional imaging. *Biomedical microdevices*, 12(2):223–233, 2010.

[62] Hyun-Joon Shin, Mark C Pierce, Daesung Lee, Hyejun Ra, Olav Solgaard, Rebecca Richards-Kortum, et al. Fiber-optic confocal microscope using a mems scanner and miniature objective lens. *Opt. Express*, 15(15):9113–9122, 2007.

[63] G-DJ Su, Shi-Sheng Lee, and Ming C Wu. Optical scanners realized by surface-micromachined vertical torsion mirror. *Photonics Technology Letters, IEEE*, 11(5):587–589, 1999.

[64] Tuqiang Xie, Huikai Xie, GK Fedder, and Yingtian Pan. Endoscopic optical coherence tomography with new mems mirror. *Electronics Letters*, 39(21):1535–1536, 2003.

[65] Yogesh G Patel, Kishwer S Nehal, Iana Aranda, Yongbiao Li, Allan C Halpern, and Milind Rajadhyaksha. Confocal reflectance mosaicing of basal cell carcinomas in mohs surgical skin excisions. *Journal of biomedical optics*, 12(3):034027–034027, 2007.

[66] Narasimhan Rajaram, Timothy J Aramil, Kelvin Lee, Jason S Reichenberg, Tri H Nguyen, and James W Tunnell. Design and validation of a clinical instrument for spectral diagnosis of cutaneous malignancy. *Applied optics*, 49(2):142–152, 2010.

[67] Darrell S Rigel, Robert J Friedman, and Alfred W Kopf. Lifetime risk for development of skin cancer in the us population: current estimate is now 1 in 5. *Journal of the American Academy of Dermatology*, 35(6):1012–1013, 1996.

[68] Robert S Stern. Prevalence of a history of skin cancer in 2007: results of an incidence-based model. *Archives of dermatology*, 146(3):279, 2010.

[69] Dena L Miller and Martin A Weinstock. Nonmelanoma skin cancer in the united states: incidence. *Journal of the American Academy of Dermatology*, 30(5):774–778, 1994.

[70] Heralio Serrano, Joseph Scotto, Gale Shornick, Thomas R Fears, and E Robert Greenberg. Incidence of nonmelanoma skin cancer in new hampshire and vermont. *Journal of the American Academy of Dermatology*, 24(4):574–579, 1991.

[71] Tamara S Housman, Phillip M Williford, Steven R Feldman, Hoa V Teuschler, Alan B Fleischer, Neal D Goldman, Rajesh Balkrishnan, and G John Chen. Nonmelanoma skin cancer: an episode of care management approach. *Dermatologic surgery*, 29(7):700–711, 2003.

[72] Judith R Mourant, Andreas H Hielscher, Angelia A Eick, Tamara M Johnson, and James P Freyer. Evidence of intrinsic differences in the light scattering properties of tumorigenic and nontumorigenic cells. *Cancer Cytopathology*, 84(6):366–374, 1998.

[73] N Ramanujam, M Follen Mitchell, A Mahadevan, S Warren, S Thomsen, E Silva, and R Richards-Kortum. In vivo diagnosis of cervical intraepithelial neoplasia using 337-nm-excited laser-induced fluorescence. *Proceedings of the National Academy of Sciences*, 91(21):10193–10197, 1994.

[74] Rebecca Richards-Kortum, MF Mitchell, Nimmi Ramanujam, Anita Mahadevan, Sharon Thomsen, et al. In vivo fluorescence spectroscopy: potential for noninvasive, automated diagnosis of cervical intraepithelial neoplasia and use as a surrogate endpoint biomarker. *Journal of cellular biochemistry. Supplement*, 19:111, 1994.

[75] Autofluorescence microscopy of fresh cervical-tissue sections reveals alterations in tissue biochemistry with dysplasia¶.

[76] Marie Morille, Catherine Passirani, Sandrine Dufort, Guillaume Bastiat, Bruno Pitard, Jean-Luc Coll, and Jean-Pierre Benoit. Tumor transfection after systemic injection of dna lipid nanocapsules. *Biomaterials*, 32(9):2327–2333, 2011.

[77] Thomas J Farrell, Michael S Patterson, and Brian Wilson. A diffusion theory model of spatially resolved, steady-state diffuse reflectance for the noninvasive determination of tissue optical properties in vivo. *Medical physics*, 19:879, 1992.

[78] George Zonios, Lev T Perelman, Vadim Backman, Ramasamy Manoharan, Maryann Fitzmaurice, Jacques Van Dam, and Michael S Feld. Diffuse reflectance spectroscopy of human adenomatous colon polyps¡ i¿ in vivo¡/i¿. *Applied Optics*, 38(31):6628–6637, 1999.

[79] Steven L Jacques. Monte carlo modeling of light transport in tissue (steady state and time of flight). In *Optical-thermal response of laser-irradiated tissue*, pages 109–144. Springer, 2011.

[80] Changfang Zhu, Gregory M Palmer, Tara M Breslin, Josephine Harter, and Nirmala Ramanujam. Diagnosis of breast cancer using diffuse reflectance spectroscopy: comparison of a monte carlo versus partial least squares analysis based feature extraction technique. *Lasers in Surgery and Medicine*, 38(7):714–724, 2006.

[81] Narasimhan Rajaram, Tri H Nguyen, and James W Tunnell. Lookup table–based inverse model for determining optical properties of turbid media. *Journal of biomedical optics*, 13(5):050501–050501, 2008.

[82] Ishan Barman, Narahara Chari Dingari, Narasimhan Rajaram, James W Tunnell, Ramachandra R Dasari, and Michael S Feld. Rapid and accurate determination of tissue optical properties using least-squares support vector machines. *Biomedical optics express*, 2(3):592, 2011.

[83] Sean A Burgess, Matthew B Bouchard, Baohong Yuan, and Elizabeth Hillman. Simultaneous multiwavelength laminar optical tomography. *Optics letters*, 33(22):2710–2712, 2008.

[84] YD Gokdel, B Sarioglu, S Mutlu, and AD Yalcinkaya. Design and fabrication of two-axis micromachined steel scanners. *Journal of Micromechanics and Microengineering*, 19(7):075001, 2009.

[85] Jack W Judy and Richard S Muller. Magnetically actuated, addressable microstructures. *Microelectromechanical Systems, Journal of*, 6(3):249–256, 1997.

[86] Serhan O Isikman, Olgaç Ergeneman, Arda D Yalcinkaya, and Hakan Urey. Modeling and characterization of soft magnetic film actuated 2-d scanners. *Selected Topics in Quantum Electronics, IEEE Journal of*, 13(2):283–289, 2007.

[87] Hakan Urey. Torsional mems scanner design for high-resolution scanning display systems. In *International Symposium on Optical Science and Technology*, pages 27–37. International Society for Optics and Photonics, 2002.

[88] Dooyoung Hah, Pamela R Patterson, Hung D Nguyen, Hiroshi Toshiyoshi, and Ming C Wu. Theory and experiments of angular vertical comb-drive actuators for

scanning micromirrors. *Selected Topics in Quantum Electronics, IEEE Journal of*, 10(3):505–513, 2004.

[89] Youmin Wang, Sheldon Bish, James W Tunnell, and Xiaojing Zhang. Mems scanner enabled real-time depth sensitive hyperspectral imaging of biological tissue. *Optics Express*, 18(23):24101, 2010.

[90] LY Lin, SS Lee, KSJ Pister, and MC Wu. Micro-machined three-dimensional micro-optics for integrated free-space optical system. *Photonics Technology Letters, IEEE*, 6(12):1445–1447, 1994.

[91] Matt Young. Zone plates and their aberrations. *JOSA*, 62(8):972–976, 1972.

[92] Qing Cao and Jürgen Jahns. Comprehensive focusing analysis of various fresnel zone plates. *JOSA A*, 21(4):561–571, 2004.

[93] Sungdo Cha, Paul C Lin, Lijun Zhu, Pang-Chen Sun, and Yeshaiahu Fainman. Nontranslational three-dimensional profilometry by chromatic confocal microscopy with dynamically configurable micromirror scanning. *Applied optics*, 39(16):2605–2613, 2000.

[94] Max Born and Emil Wolf. *Principles of optics: electromagnetic theory of propagation, interference and diffraction of light*. CUP Archive, 1999.

[95] N Delen and B Hooker. Free-space beam propagation between arbitrarily oriented planes based on full diffraction theory: a fast fourier transform approach. *JOSA A*, 15(4):857–867, 1998.

[96] Uma Krishnamoorthy, Daesung Lee, and Olav Solgaard. Self-aligned vertical electrostatic combdrives for micromirror actuation. *Microelectromechanical Systems, Journal of*, 12(4):458–464, 2003.

[97] Youmin Wang, Karthik Kumar, Lingyun Wang, and Xiaojing Zhang. Monolithic integration of binary-phase fresnel zone plate objectives on 2-axis scanning micromirrors for compact microscopes. *Optics Express*, 20(6):6657–6668, 2012.

[98] John A Richards. *Remote sensing digital image analysis*. Springer, 2012.

[99] Liang Gao, Robert Kester, and Tomasz Tkaczyk. Optical design of a snapshot high-sampling image mapping spectrometer (ims) for hyperspectral microscopy. In *BiOS*, pages 75700Z–75700Z. International Society for Optics and Photonics, 2010.

[100] Peter TC So, Chen Y Dong, Barry R Masters, and Keith M Berland. Two-photon excitation fluorescence microscopy. *Annual review of biomedical engineering*, 2(1):399–429, 2000.

[101] Reinhart Poprawe. *Tailored Light 2: Laser Application Technology*, volume 2. Springerverlag Berlin Heidelberg, 2011.

[102] Joseph R Lakowicz. *Topics in Fluorescence Spectroscopy: Volume 1: Techniques*, volume 1. Springer, 1992.

[103] RM MacKie, C Fleming, AD McMahon, and P Jarrett. The use of the dermatoscope to identify early melanoma using the three-colour test. *British Journal of Dermatology*, 146(3):481–484, 2002.

[104] Fritjof Helmchen, Michale S Fee, David W Tank, and Winfried Denk. A miniature head-mounted two-photon microscope: high-resolution brain imaging in freely moving animals. *Neuron*, 31(6):903–912, 2001.

[105] Benjamin A Flusberg, Juergen C Jung, Eric D Cocker, Erik P Anderson, and Mark J Schnitzer. In vivo brain imaging using a portable 3.9 gram two-photon fluorescence microendoscope. *Optics letters*, 30(17):2272–2274, 2005.

[106] David L Dickensheets and Gordon S Kino. Scanned optical fiber confocal microscope. In *IS&T/SPIE 1994 International Symposium on Electronic Imaging: Science and Technology*, pages 39–47. International Society for Optics and Photonics, 1994.

[107] Christopher L Hoy, W Piyawattabanetha, H Ra, O Solgaard, and A Ben-Yakar. Optical design and imaging performance testing of a 9.6-mm diameter femtosecond laser microsurgery probe. *Opt. Express*, 19(11):10536–10552, 2011.

[108] Wibool Piyawattanametha, Robert PJ Barretto, Tony H Ko, Benjamin A Flusberg, Eric D Cocker, Hyejun Ra, Daesung Lee, Olav Solgaard, and Mark J Schnitzer. Fast-scanning two-photon fluorescence imaging based on a microelectromechanical systems two-dimensional scanning mirror. *Optics letters*, 31(13):2018–2020, 2006.

[109] Hongchun Bao, John Allen, Robert Pattie, Rod Vance, and Min Gu. Fast handheld two-photon fluorescence microendoscope with a 475 $\mu$m$\times$ 475 $\mu$m field of view for in vivo imaging. *Optics letters*, 33(12):1333–1335, 2008.

[110] Wibool Piyawattanametha and MJ Schnitzer. Cortical blood flow imaging with a portable mems based 2-photon fluorescence microendoscope. In *Nano/Micro Engineered and Molecular Systems (NEMS), 2011 IEEE International Conference on*, pages 1262–1266. IEEE, 2011.

[111] Warren R Zipfel, Rebecca M Williams, Richard Christie, Alexander Yu Nikitin, Bradley T Hyman, and Watt W Webb. Live tissue intrinsic emission microscopy using multiphoton-excited native fluorescence and second harmonic generation. *Proceedings of the National Academy of Sciences*, 100(12):7075–7080, 2003.

[112] Shaohui Huang, Ahmed A Heikal, and Watt W Webb. Two-photon fluorescence spectroscopy and microscopy of nad (p) h and flavoprotein. *Biophysical journal*, 82(5):2811–2825, 2002.

[113] Irene Georgakoudi, Brian C Jacobson, Markus G Müller, Ellen E Sheets, Kamran Badizadegan, David L Carr-Locke, Christopher P Crum, Charles W Boone, Ramachandra R Dasari, Jacques Van Dam, et al. Nad (p) h and collagen as in vivo quantitative fluorescent biomarkers of epithelial precancerous changes. *Cancer research*, 62(3):682–687, 2002.

[114] S Fine and WP Hansen. Optical second harmonic generation in biological systems. *Applied Optics*, 10(10):2350–2353, 1971.

[115] E Georgiou, T Theodossiou, V Hovhannisyan, K Politopoulos, GS Rapti, and D Yova. Second and third optical harmonic generation in type i collagen, by nanosecond laser irradiation, over a broad spectral region. *Optics communications*, 176(1):253–260, 2000.

[116] Yici Guo, Howard E Savage, Feng Liu, Stimson P Schantz, PP Ho, and RR Alfano. Subsurface tumor progression investigated by noninvasive optical second harmonic tomography. *Proceedings of the National Academy of Sciences*, 96(19):10854–10856, 1999.

[117] Barry R Masters, Peter TC So, and Enrico Gratton. Multiphoton excitation microscopy of in vivo human skin: Functional and morphological optical biopsy based on three-dimensional imaging, lifetime measurements and fluorescence spectroscopya. *Annals of the New York Academy of Sciences*, 838(1):58–67, 1998.

[118] Barry R Masters and Peter TC So. Confocal microscopy and multi-photon excitation microscopy of human skin in vivo. *Opt. Express*, 8(1):2–10, 2001.

[119] Angelie Agarwal, Mariah L Coleno, Vincent P Wallace, Wei-Yang Wu, Chung-Ho Sun, Bruce J Tromberg, and Steven C George. Two-photon laser scanning microscopy of epithelial cell-modulated collagen density in engineered human lung tissue. *Tissue engineering*, 7(2):191–202, 2001.

[120] Beop-Min Kim, Jürgen Eichler, Karen M Reiser, Alexander M Rubenchik, and Luiz B Da Silva. Collagen structure and nonlinear susceptibility: effects of heat, glycation, and enzymatic cleavage on second harmonic signal intensity. *Lasers in surgery and medicine*, 27(4):329–335, 2000.

[121] Jonathan AN Fisher, Brian M Salzberg, and Arjun G Yodh. Near infrared two-photon excitation cross-sections of voltage-sensitive dyes. *Journal of neuroscience methods*, 148(1):94–102, 2005.

[122] Chris Xu, Warren Zipfel, Jason B Shear, Rebecca M Williams, and Watt W Webb. Multiphoton fluorescence excitation: new spectral windows for biological nonlinear microscopy. *Proceedings of the National Academy of Sciences*, 93(20):10763–10768, 1996.

[123] LK Koay, MM Ratnam, and Horizon Gitano-Briggs. An approach for nonlinear damping characterization for linear optical scanner. *Experimental Techniques*, 2012.

[124] Shalu Suri and Christine E Schmidt. Cell-laden hydrogel constructs of hyaluronic acid, collagen, and laminin for neural tissue engineering. *Tissue Engineering Part A*, 16(5):1703–1716, 2010.

[125] Gerhardt Attard, Joost F Swennenhuis, David Olmos, Alison HM Reid, Elaine Vickers, Roger A'Hern, Rianne Levink, Frank Coumans, Joana Moreira, Ruth Riisnaes, et al. Characterization of erg, ar and pten gene status in circulating tumor cells from patients with castration-resistant prostate cancer. *Cancer Research*, 69(7):2912–2918, 2009.

[126] Kazunori Hoshino, Yu-Yen Huang, Nancy Lane, Michael Huebschman, Jonathan W Uhr, Eugene P Frenkel, and Xiaojing Zhang. Microchip-based immunomagnetic detection of circulating tumor cells. *Lab on a Chip*, 11(20):3449–3457, 2011.

[127] Guoan Zheng, Seung Ah Lee, Samuel Yang, and Changhuei Yang. Sub-pixel resolving optofluidic microscope for on-chip cell imaging. *Lab on a Chip*, 10(22):3125–3129, 2010.

[128] Julie A Rytlewski, Laura R Geuss, Chinedu I Anyaeji, Evan W Lewis, and Laura J Suggs. Three-dimensional image quantification as a new morphometry method for tissue engineering. *Tissue Engineering Part C: Methods*, 18(7):507–516, 2012.

# Vita

Youmin Wang was born in Wuxi, China on April 30, 1986.

He received the Bachelor of Engineering degree in Electronics Engineering at Shanghai Jiao Tong University (SJTU) in 2008. He wrote his Bachelor thesis "Image Processing and Computer Vision in the Modeling and Evaluation of Visual Hallucination under Virtual Environment"based on his work at Biomedical Information Institute of SJTU which was part of Chinese National "973"Key Program. He was honored Shanghai Outstanding Graduate upon undergraduate graduation. He entered the University of Texas at Austin in August 2008 and got the Master of Science in Electrical Engineering degree in May 2010.

From then he started work toward doctoral degree till May 2013 under the supervision of Prof. John X.J. Zhang, on multi-modality endoscopes for early-cancer diagnosis.

Permanent address: 107 West Dean Keeton St. BME 3.342
Austin, Texas 78712
U. S. A.

This Dissertation was typeset with LaTeX[†] by the author.

[†]LaTeX is a document preparation system developed by Leslie Lamport as a special version of Donald Knuth's TeX Program.